ADVANCED PHASE DETECTION IN SURFACE PLASMONIC MICROSCOPY

WAI KIN CHOW

PhD

The Hong Kong Polytechnic University

2019

The Hong Kong Polytechnic University

Department of Electronic and Information Engineering

Advanced Phase Detection in Surface Plasmonic Microscopy

Wai Kin CHOW

A thesis submitted in partial fulfilment of the requirements for the degree of Doctor of Philosophy

November 2018

CERTIFICATE OF ORIGINALITY

I hereby declare that this thesis is my own work and that, to the best of my knowledge and belief, it reproduces no material previously published or written, nor material that has been accepted for the award of any other degree or diploma, except where due acknowledgement has been made in the text.

____________________ (Signed)

CHOW Wai Kin (Name of Student)

Abstract

Surface plasmon resonance sensing is a technique widely used for real-time, high axial-sensitivity and label-free monitoring for bio-molecular interactions. By measuring the phase change around excitation angle, phase-based Surface Plasmon Resonance sensing has been found to have better sensitive than intensity-based in recent years. In addition we have developed methods based on confocal microscopy to improve the measurement localization. This thesis addresses methods to combine both microscopic and phase measurement on samples supporting surface plasmons. To measure phase two beam interferometry is most commonly used, however, the optical setup for interference measurement is more challenging as its configuration is more complicated than the conventional intensity-based measurement. Recently, our group developed an embedded confocal surface plasmon microscope to recover excitation angle by interfering the leakage radiation of SPs and the direct reflection along normal incident angle. This provides a compact and stable form of interferometry.

As the system is a confocal scanning system, it requires a series of confocal measurements to perform the measurement. Our group proposed an advanced modulation strategy to improve the speed of the acquisition process. In this thesis, we apply an optical vortex approach to which can enhance the speed of data acquisition by an approximately a factor of 4 without sacrificing the signal-to-noise ratio. In addition we also address a Hilbert transform approach to reduce the data acquisition time.

On the other hand, the system not only allows us to locate the excitation angle of the SP, it can also be used to determine the characteristics of the sample by measuring the phase information around SPs. In this thesis, we show that different loss mechanisms, due to reradiation and absorption, of the SP can be separated by imposing additional Goos–Hänchen phase in the surface plasmon microscope. The experimental result is validated by separating the loss mechanism on gold sample with different thickness.

Thanks to the phase information of SP, more insight of the SP can be investigated. Therefore, it will be great if we can measure all the phase information on the reflection spectrum. In this thesis, ptychography algorithm is applied to recover the complex field of the BFP (the phase and the modulus of the field can be recovered). Experiment shows that the phase on BFP can be recovered successfully. With the recovered field, it allows us to perform more advanced post processing techniques to extract more information. For example, the field from the back focal plane can be projected using virtual optics to any plane in the imaging system. We demonstrate several results including the attenuation results can be obtained with this method. In other words we show that by measuring the phase we can obtain similar or indeed superior results to those we previously obtained by manipulating the phase with the spatial light modulator.

In this thesis, it will be divided into two main parts, (1) advanced beam profile modulation based on SLM phase modulation and (2) Quantitative (amplitude and phase) measurement of SPR based on ptychography will be discussed.

Acknowledgement

I would like to express my sincere gratitude to my original supervisor Professor Michael Somekh for his knowledge, guidance, encouragement, support and patience during the entire period of my research. I would like to thank my current supervisor Dr. Daniel Lun for the kindly supervision in my final year. I would also like to thank Dr. Wen Chen for the kindly support, especially for the demonstration of the phase retrieval algorithm.

I would like to thank the Department of Electronic and Information Engineering (EIE) for the funding of my work. I appreciate the financial support from the Research Committee of the Hong Kong Polytechnic University.

I would like to thank Dr. Suejit Pechprasarn for the laser alignment training and the guidance. I would like to thank the facility provided by Material Resource Centre (MRC) and University Research Facility in Materials Characterization and Device Fabrication (UMF), especially Dr. Hardy Lui and Dr. Terence Wong. I would like to thank everyone in our group especially Mr. Jingkai Meng and Mr. Zhuangyu Han for the valuable discussion and the co-operation.

I would like to thank my family, especially my parents, my sisters and my better half Tiffany for their love and support.

Terry Wai Kin CHOW

Table of Contents

Publications

Journals

1) Pechprasarn S, Melnikov A, Chow TWK, Somekh MG (2018) Widefield Confocal Microscope for Surface Wave K-Vector Measurement. Nano Res Appl. Vol.4 No.2:4. doi:10.21767/2471-9838.100029

2) Chow, T. W. K., Zhang, B., & Somekh, M. G. (2018). Hilbert transform-based single-shot plasmon microscopy. Optics Letters, 43(18), 4453-4456. doi:10.1364/OL.43.004453

3) Pechprasarn, S., Chow, T. W. K., & Somekh, M. G. (2018). Application of confocal surface wave microscope to self-calibrated attenuation coefficient measurement by Goos-Hänchen phase shift modulation. Scientific Reports, 8, 8547. doi:10.1038/s41598-018-26424-2

4) Pechprasarn, S., Chow, T. W. K., Ittipornnuson, K., Somekh, M. G., & Albutt, N. (2017). Confocal Surface Plasmon Embedded Interferometric Microscope: A Brief Review. Applied Mechanics and Materials, 866, 365-369. doi:10.4028/www.scientific.net/AMM.866.365

5) Chow, T. W. K., Pechprasarn, S., Meng, J., & Somekh, M. G. (2016). Single shot embedded surface plasmon microscopy with vortex illumination. Optics Express, 24(10), 10797-10805. doi:10.1364/OE.24.010797

Journals in preparation

1) Chow, T. W. K., Chen W., Lun P.K. & Somekh, M. G. (2018) Back focal plane ptychography as a measurement tool: application to plasmonic and surface wave characterization

2) Chow, T. W. K., Lun P.K. & Somekh, M. G. (2018) Image plane diagnostics for surface wave characterisation

Conference Proceedings

1) Chow, W.-K., Pechprasarn, S., & Somekh, M. G. (2016). Embedded Interferometry with Dynamic Reference Beam. Paper presented at the APMC11 / MST33 / AAT39 Conference Phuket, Thailand

2) Somekh, M. G., Pechprasarn, S., Chow, W.-K., Meng, J., & Shen, H. (2016). New avenues for confocal surface plasmon microscopy. Paper presented at the SPIE BiOS.

3) Pechprasarn, S., Chow, W. K., Meng, J., & Somekh, M. G. (2015, 25-27 Nov. 2015). Confocal surface plasmon microscopy with vortex beam illumination for biosensing application: Label free biosensing application of confocal surface plasmon microscope. Paper presented at the 2015 8th Biomedical Engineering International Conference (BMEiCON).

4) Pechprasarn, S., Chow, W.-K., Meng, J., & Somekh, M. G. (2015, 2015/11/19). Confocal surface plasmon microscopy with vortex beam illumination for biosensing application. Paper presented at the Asia Communications and Photonics Conference 2015, Hong Kong.

List of Figures

Abbreviations

AM – Amplitude Modulation

BFP – Back Focal Plane

CMOS – Complementary Metal-Oxide-Semiconductor

FFT – Fast Fourier Transform

FM – Frequency Modulation

GH – Goos–Hänchen

GS algorithm – Gerchberg and Saxton algorithm

HeNe laser - Helium–neon laser

ITO – Indium Tin Oxide

LiF – Lithium Fluoride

NA – Numerical Aperture

PIE – Ptychographic Iterative Engine

PMMA – Poly(methyl methacrylate)

SLM – Spatial Light Modulator

SP(R) – Surface Plasmon (Resonance)

SP(R)M – Surface Plasmon (Resonance) Microscope

SNOM – Scanning Near-field Optical Microscope

TIE – Transport of Intensity Equation

Chapter 1 – Introduction

Surface plasmon resonance (SPR) sensing provides a non-invasive, real-time and sensitive measurement to observe biomolecular interactions within a confined axial region on the sensor surface. On the sample's surface, a sensing field is established when surface plasmon is excited by incident light. Under attenuated total internal reflection configuration, at resonance condition, a dip is formed in the angular reflection spectrum due to energy dissipation among the metallic layer or scattering on the surface. (Kretschmann & Raether, 1968)

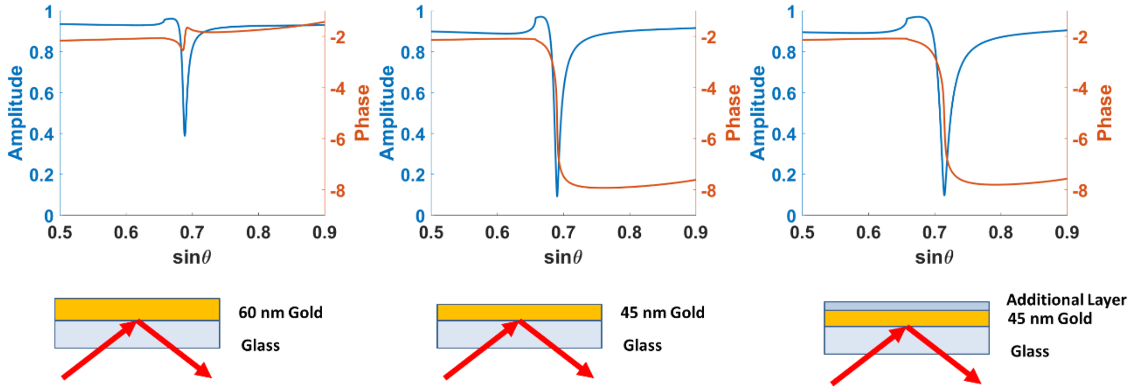

Figure 1-1 shows the simulated reflected spectrum in different structures. (a) thick gold: 60 nm, (b) standard thickness: 45nm and (c) standard thickness: 45nm with additional layer of dielectric

The result shown on Figure 1-1 are the simulated reflected spectrum on different smooth layered structure where the dips arise from the ohmic loss in the metal layer. When the structure of the samples is different with respect to the refractive index and thickness of the layers, the reflected spectrum will exhibit different amplitude and phase response. Biosensing biomolecular interactions can be monitored by the change of the angular response of surface plasmon resonance (SPR) (Bo Liedberg, Nylander, & Lunström, 1983) (as shown on Figure 1-1b to 1c, the dip is moved from

0.691 to 0.715 according to the thickness and the refractive index of the additional layer). The dip position in the spectrum relies on the effective refractive index (or so called bulk refractive index) within the sensing field. As the penetration depth is only hundreds of nanometers, it is therefore very sensitive to changes of the effective refractive index in a confined region for monitoring the bio-molecules interaction at the interface. Also, it is a label-free technique which means the biomolecules can be studied without attachment to a fluorescent dye, which can perturb the measurements. Moreover, fluorescent measurements are subject to photobleaching and phototoxcity which damages living cells. For this the surface plasmon resonance technique can be used for a wide range of applications such as drug discovery (Patching, 2014), food safety (Situ, Mooney, Elliott, & Buijs, 2010), virus detection (Boltovets et al., 2004) and environmental monitoring. (Dillon, Daly, Killard, & O'Kennedy, 2003)

In recent years, more researchers are working on the phase detection of surface plasmon resonance sensing because the phase change with respect to the k-vector on the reflection spectrum is much sharper than that of intensity-based approach resulting better sensitivity (Andrei V. Kabashin, Sergiy Patskovsky, & Alexander N. Grigorenko, 2009) (as shown in Figure 1-1). At resonance, the surface plasmon not only undergoes reduction of intensity but also a phase shift leading to a Goos-Hanchen lateral shift on the sample surface. For intensity-based method, the resonance k-vector can be recovered by the dip position where the intensity is minimum in the reflection spectrum. The system of intensity-based method is relatively simple as only the intensity of the reflection spectrum needs to be recorded which can be performed by a standard detector. However, for phase-based method, the resonance k-vector is recovered according to phase transition on the reflected spectrum. It becomes complicated as it requires a reference beam to recover the phase information. Recently, our group has demonstrated that the phase of the surface plasmon can be measured on an embedded confocal surface plasmon microscopy. A confocal measurement, so called V(z), along defocus z is used to determine the excitation angle at resonance condition. The accuracy and the robustness can be further improved by modulating the pupil function on the back focal plane of the objective lens. (B. Zhang, Pechprasarn, & Somekh, 2012; Bei Zhang, Pechprasarn, Somekh, & Zhang, 2012) However, there is still plenty of room for improvement in terms of parameters such as acquisition time. The recovery process relies on the V(z) curve which requires a series of defocus images in resulting long acquisition time. The phase information provides additional information about the sample such as propagation length which can be determined by the gradient of the phase transition on the reflected spectrum $d\Phi/dk$ where Φ is the relative phase of the reflection of the corresponding k-vector. As shown on Figure 1-1a and 1b, the phase shift will exhibit differently in different sample structures. By investigating the shape of the phase response, the characteristics of the sample can be identified. It can be used for designing and testing a bio-sensor to optimum parameters.

In this chapter, I will discuss the current issues of phase sensing on surface plasmon resonance microscope (SPRM), the research objective of this thesis and the outline of the thesis.

1.1 Current Issues in Surface plasmon microscopy

Phase-based SPR sensing gains great attention in recent years due to the better sensitivity as described above. Although it can provide better sensitivity in measurement, it involves more complicated configuration compared with the intensity based SPR sensing. Thanks to the embedded confocal SPRM (B. Zhang, S. Pechprasarn, & M. G. Somekh, 2012; Bei Zhang et al., 2012), the trade-off between the sensitivity and the resolution is solved. However, it requires time-consuming scanning operations which may introduce systematic error due to the long acquisition process. Therefore, it will make it even more attractive if the time for the acquisition process can be reduced.

On the other hand, the understanding of characteristics of the sensors can be used to improve the sample design for better measurement performance. For example, the propagation length of the SP on the sample is one of the key parameters that determine the performance of many surface plasmon measurement systems. Therefore, understanding the loss mechanism of the SP becomes necessary to optimize and understand the performance. There are two main loss mechanisms which are the coupling loss (re-radiation of SP) and the ohmic loss within lossy materials. To the best of our knowledge, there is no direct method, including far field and near field, to separate the loss mechanism of SP. It is clear that the development of surface wave instrumentation can be improved by better understanding the loss mechanisms of SPs.

Lastly, in the confocal SPRM, the collected confocal signal is an intensity signal which is a summation over a weighted sum of angles and polarizations. Therefore, the relative phase shift with respect to the incident angle is not directly known. In order words, most of the phase information is lost. In order to measure the data from the sample such as the attenuation coefficients of the SP, an additional measurement is needed to be conducted. Therefore, it will make it more effective that the complete field (modulus and phase) on the BFP can be recovered. Therefore, the new data can be obtained by processing the recovered complex BFP without additional measurement.

1.2 Research Aims and Objectives

The effect of phase on the SP is well established. It provides an excellent way of enhancing the performance of different sensors. The purpose of this thesis is to investigate how phase measurements can be used in surface plasmon microscopy, where the surface waves are excited through an objective lens, giving the possibility for localized measurements. This thesis will mainly concentrate on two related themes; in the early parts of the thesis we will consider the effect of manipulating the phase with a spatial light modulator; in later chapters I will show how measuring the phase can allow one to perform of the similar functions to those achieved by physical manipulation of the phase. Phase measurement therefore allows one to replace many hardware operations with inexpensive and versatile computational optics.

Specifically, in this thesis, various phase sensing techniques on the embedded confocal surface plasmon resonance microscope (SPRM) will be investigated. In this chapter, the detailed research objective will be listed.

The research objectives to achieve our overall aim can be divided into three parts.

The first goal is to develop the advanced techniques to improve of performance in the embedded SLM-based surface plasmon microscope. We are going to develop a series of BFP phase modulation technique to help to improve the signal-to-noise ratio and the acquisition time during the measurement without the increase of complexity. The second goal is to separate the loss mechanism of the surface plasmon in various structures using our embedded confocal SPRM. It will be done by imposing artificial Goos–Hänchen phase shift on the BFP with a phase-SLM.

The third goal is to retrieve the quantitative phase information of the angular response by a computational algorithm, so called Ptychography. In this part, we would further make use of the recovered quantitative phase information for further measurement. The performance of the algorithm will be validated by comparing the results obtained by SLM-based measurement. We aim to obtain the result in the same quality but with simpler instrumentation.

1.3 Outline of thesis

Chapter 2 – Background and Literature Review describes the physics of surface plasmon, the development of surface plasmon sensing and latest progress on the embedded confocal surface plasmon microscopy. The background of the conventional ptychographic iterative engine will also be discussed.

Chapter 3 – Experimental material and methods describes the selection of the components for the experimental setups and the theoretical model for the system. The calibration of the phase SLM for SLM-based SPRM and the design of the rotation stage for the ptychographic iterative engine will also be discussed.

Chapter 4 - Advanced Pupil Function Engineering in SPRM describes the modelling of V(z) curve on the embedded confocal surface plasmon microscope and the signal to noise improvement based on the advanced pupil function engineering. Also, vortex phase modulation technique will also be described, and the experimental result show the improvement on the speed of acquisition. Additionally, a Hilbert transform approach will be addressed on how it can be used to reduce the data acquisition time.

Chapter 5 – Separation of Attenuation mechanisms by Goos–Hänchen Phase Engineering describes the measurement of attenuation of surface plasmon in SPRM. I will first discuss the model of the attenuation of SP. I will show how the phase shift of SP can be used to separate the attenuation mechanism of coupling loss and ohmic loss. The experimental result of separation of loss mechanism is also addressed.

Chapter 6– Quantitative Phase Measurement by Back Focal Plane Ptychography describes the quantitative measurement on BFP by Ptychographic iterative algorithm. I will first address the modified settings for SPRM. The data processing for the modified ptychographic iterative engine will also be discussed in detail. The result will be compared with the direct measurement and the result obtained by the SLM-based SPRM. Some interesting samples will also be examined.

Chapter 7– Conclusion and Future Work describes conclusion of the thesis and the future work on surface plasmon microscope

Chapter 2 – Background and Literature Review

This project is mainly concerned with various phase detection techniques on objective-based surface plasmon microscope. In general, there are two types of approaches to be presented in this thesis. One is SLM-based phase measurement, so called V(z) which applies phase modulation technique to improve the performance of the system and explore the characteristics of the sample. Another approach is the computational technique such as ptychography or transport of intensity, to recover quantitative angular phase information on BFP. In this chapter, I will first review the fundamentals of SLM-based surface plasmon microscopes including the physics of surface plasmon and the algorithm to recover the phase information by the phase modulation techniques. Then, I will review the background of phase retrieval algorithms and the principle of the ptychography.

2.1 Fundamentals of Surface Plasmon

2.1.1 Background of Surface Plasmon

Surface plasmon was first observed on gratings in 1902. (Wood, 1902) Wood reported an observation of a reflection of bright and dark bands when illuminating metal grating, although he was unable to provide an explanation of the observation. Rayleigh attempted to explain the Wood's observation by dynamical theory of grating. The theory indicated that the scattered field at the Rayleigh wavelength corresponds to the position of the discontinuous change of intensity on the spectrum from Wood's observation. However, the theory cannot explain the gradual intensity change (or the shape of the intensity band) around the position where the discontinuous change of intensity was observed. (Rayleigh, 1907) Further explanation based on Rayleigh theory proposed by Fano (Fano, 1941). But there was still a mismatch between theory and the observation. Hessel and Oliner (Hessel & Oliner, 1965) provides another theoretical explanation based on a guided wave approach in 1965. This approach can explain the band shape of the reflection spectrum. In 1957, Ritchie (Ritchie, 1957) also observed the anomalies on thin smooth surfaces rather than only observed on grating structure, this indicates that this effect arose from the properties of the materials not just the grating properties. Powell and Swan (Bohm & Pines, 1951, 1953) proposed the explanations based on rigorous vector theories to explain the phenomenon in 1951 and 1953. Finally, the theoretical framework of SPs was generalized by Raether. (Raether, 1986) He derived the SP from electromagnetic theory and studied the effect of SP on different surfaces such as smooth surfaces, rough surfaces and gratings. Nowadays, it is known that the SP can be excited when the components of the wave-vector (also called k-vector) of the illumination beam parallel to the surface matches resonance wavevector. This wavevector arises from the dispersion relations which is a function of the driving frequency. The detailed condition to excite SP will be discussed in the next section.

2.1.2 Dispersion Equation of Surface Plasmon Resonance

Surface plasmon resonance is the collective oscillation of conduction electrons at the interface between the permittivity materials with opposite signs at resonance condition. The negative permittivity occurs due to the oscillation electrons in a metal surface. (Raether, 1986). The permittivity of metal can be expressed as (derived from Drude's Model (Römer, 2005))

$$\varepsilon_{metal}(\omega) = 1 - \frac{\omega_p^2}{\omega^2} \tag{2-1}$$

The permittivity becomes negative when the operating frequency ω is smaller than plasma frequency ω_p which can be expressed as

$$\omega_p = \sqrt{\frac{n_e e^2}{\varepsilon_0 m_e}} \tag{2-2}$$

Where n_e is the density of the free electrons, m_e is effective mass of electron, e is the charge of electron and ε_0 is the permittivity of free space. Therefore, exciting SPs at longer wavelength is preferable (The detailed selection of the parameters will be discussed in the section of "Selection and Preparations of Sensors" under Chapter 3). Thanks to the good chemical properties of gold, it is normally used to fabricate the biosensor for a binding experiment. Provided that $n_{e,gold} = 5.9 \times 10^{28}\ \mathrm{m}^3$, $e = 1.6 \times 10^{-19}\ \mathrm{C}$, $\varepsilon_0 = 8.85 \times 10^{-12}\ \mathrm{F/m}$ and $m_e = 1 \times 10^{-30}\ \mathrm{kg}$, the calculated plasma frequency of gold $\omega_{p,gold}$ is $1.3 \times 10^{16}\ \mathrm{rad}$. In practice, therefore effective plasmon generation occurs at much lower angular frequencies (longer wavelenths). Practical generation of surface plasmons for gold occurs at wavelengths beyond the green part of the visible spectrum above 500nm. It can be seen that the values of the permittivity of gold driven by visible spectrum become negative according to the equation (2-1). The details of the selection of the wavelength will be discussed in Chapter 3.

It is interesting that SP cannot be excited by visible light from free space directly because the k-vector of the SP is greater than the k-vector of the incident light under the same driving frequency. Some additional coupling mechanism is necessary as discussed later. In this section, the excitation conditions of SP will be discussed. The detailed derivation can be found in (Schasfoort & Tudos, 2008)

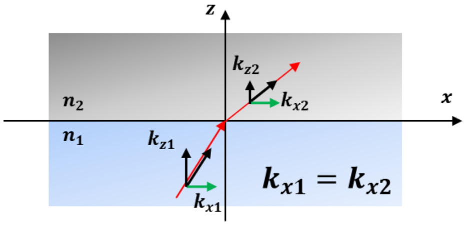

Figure 2-1 shows decomposed k-vector on two media

where the k_{x1} and k_{z1} is decomposed vector of k_1 along direction x and direction z, and k_{x2} and k_{z2} is decomposed vector of k_2 along direction x and direction z

In general, by boundary condition, the dispersion relation of SP can be derived. Now, considering two semi-infinite interfaces such that the light travels from medium 1 to medium 2 where n_1 is greater than n_2 shown on Figure 2-1. According to the incident plane, the light can be decomposed into p-polarization and s-polarization. As there is no decomposed electric field of s-polarization beam across two media, we only investigate the p-polarization beam. The wavevector to excite SP can be derived from its resonance condition. Recall that the modulus of the reflectance coefficient $|r_p|$ on the structure shown on Figure 2-1 can be expressed as (Cardona, 1971)

$$|r_p| = \left|\frac{\tan(\theta_i - \theta_r)}{\tan(\theta_i + \theta_r)}\right| \tag{2-3}$$

Where θ_i is the incident angle, θ_r is the refraction angle. On one hand, by decomposing the wavevector into two components along x-coordinate and z-coordinate we obtain

$$\tan \theta_i = k_{z1}/k_{x1} \text{ and } \tan \theta_r = k_{z2}/k_{x2} \tag{2-4}$$

On the other hand, the reflection coefficient become resonance when $(\theta_i - \theta_r) = \pi/2$. According to Snell's Law, we have

$$\sqrt{\varepsilon_1}\sin\theta_i = \sqrt{\varepsilon_2}\sin\theta_r = -\sqrt{\varepsilon_2}\cos\theta_i \tag{2-5}$$

Then, the relationship among dielectric constant, incident angle and decomposed vectors is obtained such that

$$\tan\theta_i = -\sqrt{\varepsilon_2/\varepsilon_1} = k_{z1}/k_{x1} \tag{2-6}$$

On the other hand, by decomposing the wavevector into two components along x-coordinate and z-coordinate. And it can be expressed as

$$k_{x1}^2 = k_1^2 - k_{z1}^2 = k_1^2 - k_{x1}^2\,\varepsilon_1/\varepsilon_2 \tag{2-7}$$

Also it should be noted that $k_x = k_{x1} = k_{x2}$. By re-arranging the equation, we obtain

$$k_x = k_0\sqrt{\frac{\varepsilon_1\varepsilon_2}{\varepsilon_1+\varepsilon_2}} = \frac{\omega}{c}\sqrt{\frac{\varepsilon_1\varepsilon_2}{\varepsilon_1+\varepsilon_2}} \quad \text{and} \quad k_{zi} = k_0\sqrt{\frac{\varepsilon_i^2}{\varepsilon_1+\varepsilon_2}} = \frac{\omega}{c}\sqrt{\frac{\varepsilon_i^2}{\varepsilon_1+\varepsilon_2}} \tag{2-8}$$

where ε_1 and ε_2 are the permittivity of medium 1 and 2 respectively, ω is the angular frequency and c is speed of light in vacuum.

2.1.3 Principle of SPR Sensing

In this section, we will discuss how SPR can be used for sensing application, especially for monitoring binding experiment. Two mechanisms, namely penetration depth and the change of k-vector should be discussed in detail.

In order to confine the field or energy at the interface, we are looking for a special arrangement of the layered structure such that the sign of the dielectric constant of two media are opposite. Assuming the ε_1 is positive and ε_2 is negative such that $|\varepsilon_2| > |\varepsilon_1|$, the field along z-direction k_{zi} becomes purely imaginary resulting in exponentially decay field along the z-direction according to the equation (2-8). The penetration depth gives a measure of the region where the SP is sensitive to a change in the local optical properties.

Now, considering the interface of water/gold illuminated by a HeNe (633nm) laser such that $k = 2\pi/\lambda$, the penetration depth can be calculated according to the equation (2-8). Given that $\varepsilon_1 = \varepsilon_{water} = 1.77$ and $\varepsilon_2 = \varepsilon_{gold} = -16$ (assuming no loss), the penetration depth on water side is only $\frac{1}{imag(k_{zi})} = 215\ \mathrm{nm}$. As the penetration depth is extremely short and the field is an exponential decaying, the effective index, the contribution of the effective index extended by the field mainly from the sample surface resulting sensitive response of the change on the sample near surface. For biosensing, we are interested in detecting a thin layer (much thinner than the penetration depth of the evanescent field), it can be used for wide range of applications such as protein-protein binding experiment.

2.2 Excitation of Surface Plasmon

In this section, the excitation conditions of SP will be discussed. Before we start to discuss the excitation of SP, it should be also noted that there is no electric field component can be decomposed at the interface for the beam in s-polarization. Therefore, it is expected only the beam in p-polarization can excite SPs. (Schasfoort & Tudos, 2008) Also, as mentioned before, SP can only be excited when the sufficiently large wavevector to support the propagation. It can be explained by the Figure 2-2.

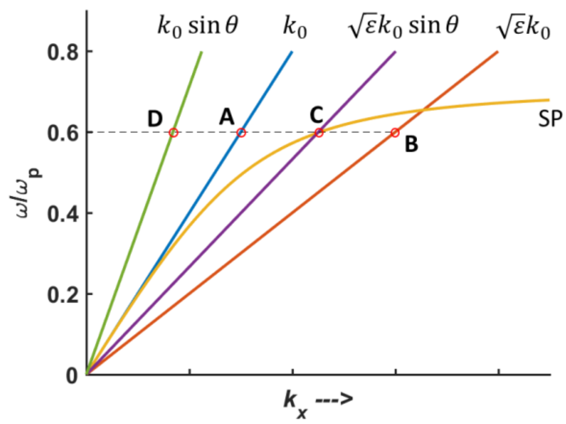

Figure 2-2 Dispersion relation for surface plasmons showing how plasmon excitation requires either a high index source medium to increase the k-vector at a given frequency, or some additional k-vector provided by a structure such as a grating.

In the figure, ω/ω_p represents the ratio between the operating frequency ω and plasmon frequency and k_x is the k-vector along the interface. the SP curve, in yellow, represents the SP dispersion between angular frequency and the k_x according to the equation (2-8) using the approximation value for ε given by equation (2-1). The blue and orange lines are the dispersion relations for light in vacuum and dielectric material with higher refractive index of $\sqrt{\varepsilon}$ respectively. It shows that the SP dispersion curve does not have an intersection with the dispersion line for light in vacuum except at the origin. It means that the wavevector of light in vacuum is always smaller than that of SP. Therefore, SP cannot be excited by light incident from free space directly. However, under appropriate configurations like Kretschmann (Kretschmann & Raether, 1968) or Otto (Otto, 1968) configurations, the SP can be excited by visible light. Now, considering the operating frequency of the excitation is ω (the horizontal dashed line, in this example, ω/ω_p = 0.6 for illustration), the necessary k-vector of the SP (operating point C) is greater than that of light in vacuum (operating point A). However, under the same operating frequency, the k-vector in the dielectric material with higher refractive index (operating point B) can be greater than that of SP. However, there is still a k-vector mismatch to excite SP. By tuning the incident angle, the component of the k-vector along x-direction in dielectric materials can be reduced (the purple line). The SP can therefore be excited when the k-vector for the illumination light matches the surface plasmon dispersions as shown at operating point C. Changes in the free space k-vector can also be imposed with a grating as discussed in the next section.

2.2.1 Grating excitation

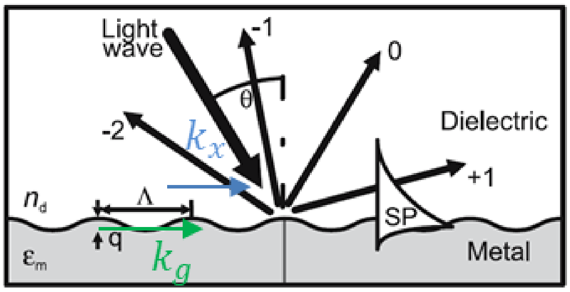

Figure 2-3 shows SP excitation by the grating structure (Homola, 2006)

In grating configuration as shown on Figure 2-3, the light wave is incident on a grating structure with a period of Λ. The grating structure generates multiple diffraction orders. And the wavevector is now changed by the grating vector of the grating structure which can be expressed as

$$k_{x,on\,surface} = k_x + mk_g = k_0 \sin\theta \pm m\frac{2\pi}{\Lambda} \qquad (2\text{-}9)$$

Where k_g is grating vector, Λ is the grating period and m is diffraction order (which is an integer number), k_0 is the wavevector of the light wave and θ is the incident angle. As discussed above, it is obvious that the change of the k-vector is discrete integer multiples of the grating vector. Therefore, it may not match the operating wavevector of SP. Hence, by varying the incident angle, the SP can be excited so that the driving wavevector and the wavevector of SP are matched. Consider the green line in Figure 2-2 this shows the variation in the k-vector for a specific incident angle in air. In order to hit the plasmon dispersion curve an additional k-vector is necessary, this is imposed by the grating which adds integer multiples of k_g to the green curve so that intersection with the plasmon dispersion is achieved. Generally, first order diffraction is stronger than higher orders so it usual for the first diffracted order to be used for excitation.

2.2.2 Attenuated Total Reflection configuration

There are two practical methods to excite SPs on a flat surface by the means of the couplant with higher index, these are the Kretschmann (Kretschmann & Raether, 1968) and Otto (Otto, 1968) configurations. These are shown on Figure 2-2, where in both cases the incident k-vector is multiplied by the index of the prism corresponding to the purple curve of Figure 2-2.

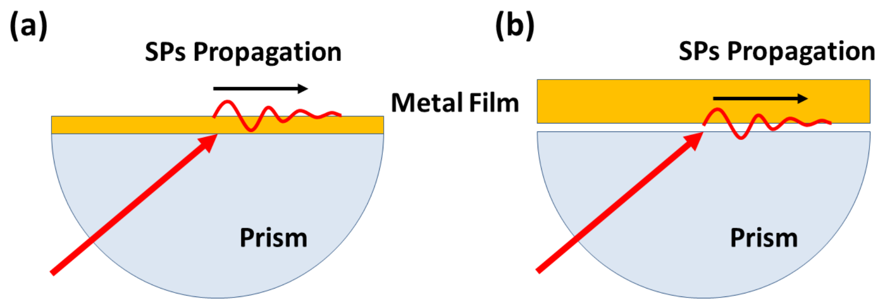

Figure 2-4 (a) Kretschmann and (b) Otto configuration for coupling surface plasmons. In both cases, the surface plasmon propagates along the metal/dielectric interface. The thickness of the metal film in Otto configuration is thick enough preventing evanescent field to the other side of the metal film.

For the Otto configuration, there is an air gap between the prism and the metal film (The metal film in Otto configuration is thick enough so that the no evanescent field extended to the other side of metal film). When the SP is excited, the SP will propagate between the air gap and the metal. For the Kretschmann configuration, after coupling, SPs are excited on the interface between the upper surface of metal and the dielectric above the sample as shown in Figure 2-4 (a). These methods are designed for different applications. The Otto configuration is suitable for investigating SPR effect on bulk material. However, the gap between prism and metallic layer is only several hundreds of nanometers resulting in difficulty of alignment making convenient measurement more difficult. Therefore, surface plasmon sensing in the Otto configuration is experimentally demanding, moreover, it is less suitable as a sensor as the SP is not accessible on the exposed surface. For the Kretschmann configuration, the SPs are excited on the upper surface. This is very suitable for monitoring the changes on the surface on the metallic layer for the applications such as antibody-antigen reaction (Singhal, Haynes, & Hansen, 2010), DNA monitoring (Jordan, Frutos, Thiel, & Corn, 1997) and pharmacology (Borch & Roepstorff, 2004)

2.2.3 Short Summary on SP Excitation

In short, only p-polarized beam can excite SP and it requires additional couplant such as prism or diffraction grating to increase the spatial frequency (or k_x) along the interface of metallic and dielectric layers for SP excitation. In this thesis, Kretschmann configuration will be used on the SPRM.

2.3 Prism-based SPR Sensor

In 1983, Liedberg et al. proposed SPR can be used for gas detection and biosensing (Bo Liedberg et al., 1983). They demonstrated that the angular shift of the dip in the reflection spectrum on protein-protein binding experiment can be employed for measuring the concentration of the solution and estimating the thickness of deposited protein on the silver sensor. After that, biosensing by SPR developed rapidly. (Löfås et al., 1991; B. Liedberg, Lundström, & Stenberg, 1993)

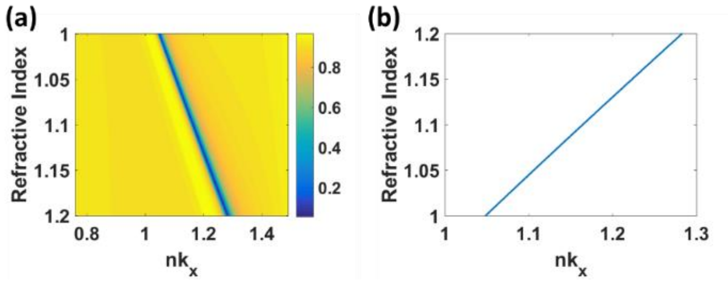

Figure 2-5 a) Reflection Spectrum of effective refractive index on the sensing side from 1 to 1.2 with different k-vector, b) The relationship between the effective refractive index and the corresponding k-vector for excitation.

As the surface plasmon resonance condition is approached, the oscillations of the electrons in the gold become stronger, so that the ohmic losses due to inelastic scattering of electrons becomes greater, so energy is absorbed as heat resulting in a dip in the reflection coefficient. When the structure is illuminated with a wide range of incident angles, a dip at certain incident angle will be formed at the SPR condition. When the refractive index of the layer above the sensor is increased resulting higher effective refractive index, then more momentum along x-direction is needed to excite the SP. Hence, the angle of incident has to be increased to fulfill the coupling condition as shown on Figure 2-5. By monitoring the position change of the dip, the change of refractive index above the sensor can be detected. In other words, the change of the k_x can be used to measure the change of the change of the coupling condition.

Thanks to the characteristics of SPR, it enables the sensitive detection on the bio-molecules interaction measurement in real time without invasive label. (Nguyen, Park, Kang, & Kim, 2015). To improve the throughput of the system, multiple antigens can be fabricated in an array structure. High throughput can be obtained when the distance between the antigens is as short as possible. In this case the lateral resolution of the system, the ability to resolve two points, becomes more important. Therefore, the need of SPR microscopy becomes more and more important. In the next section, SPRM will be discussed.

2.4 Prism-based SPR microscopy

In 1987, the idea of combining the SP with a microscope was proposed (E. Yeatman & Ash, 1987). In 1988, Rothenhäusler and Knoll designed Kretchmann based SPR microscopes shown on Figure 2-6. The sample will be illuminated in the angle close to resonance angle. The contrast of the image can be visualized based on dI/dk_x. They indicated that the lateral resolution is limited by the propagation length of the SPR.

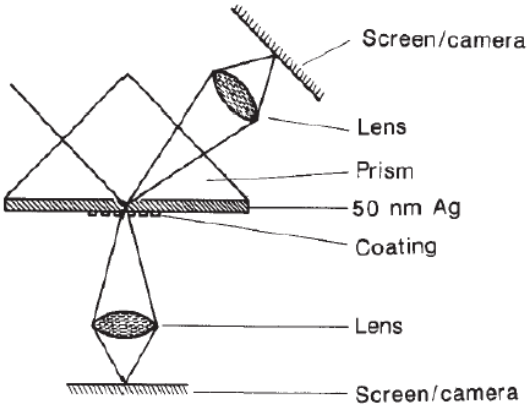

Figure 2-6 Kretchmann based SPR microscopes setup (Rothenhausler & Knoll, 1988)

In 1996, Yeatman (E. M. Yeatman, 1996) has shown that the lateral resolution can be improved by a shorter SP propagation length. However, the drawback is a reduction in sensitivity. It shows that the Kretschmann configuration cannot provide good lateral resolution together with good sensitivity for a prism-based system. A number of attempts were proposed to improve lateral resolution in SPRM. In 1999, Giebel (Giebel et al., 1999) proposed that the lateral resolution could be improved by replacing the gold layer by aluminium. As aluminium introduces more ohmic loss, the resulting propagation length is reduced resulting in better lateral resolution (around 2 microns). However, the sensitivity is again reduced.

In conclusion, there is no doubt that the axial resolution of the SPRM can be very good. However, due to the propagation length, lateral resolution of the prism-based SPRM is very poor. On the other hand, the aberration is severe in the prism based SPRM as the reradiated light from the sample at different positions has different optical path lengths. In the next section, objective-based SPR microscopy will be discussed. It can be used to overcome the problem of poor lateral resolution in prism based SPR imaging.

2.5 Objective-based SPR microscopy

In 1998, Kano (Hiroshi Kano, Mizuguchi, & Kawata, 1998) suggested objective based surface plasmon microscope to excite SP by a focused laser beam. In this way, the wider range of angular response of incident beam can be captured in one shot. On one hand, objective-based arrangement is more easily be integrated into conventional microscopic system. On the other hand, it allows us to develop more advanced strategies to extract more information from the sample.

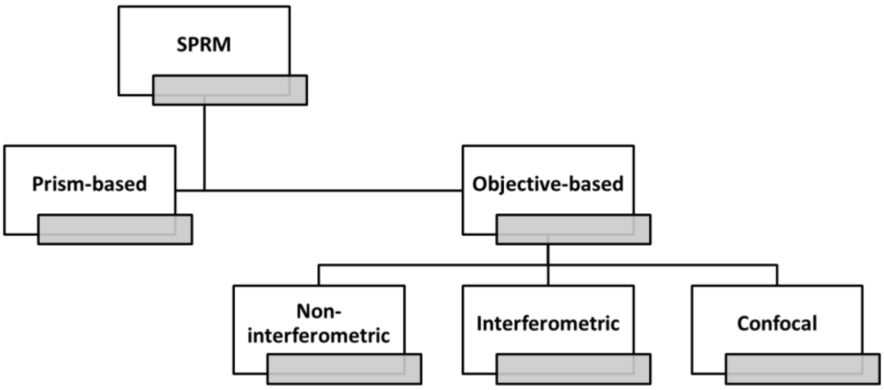

Figure 2-7 classification of SPRM

In general, the objective-based SP microscope can be classified into three types, namely non-interferometric, interferometric and confocal SPRM. (The classification of SPRM is shown on Figure 2-7) In this section, I will first explain the principle of the excitation through the objective lens. Then, we will look at the principle of those types of SPRM and the limitation of the them. Finally, we will show the current progress in embedded confocal SPRM.

2.5.1 BFP excitation of a high NA objective lens

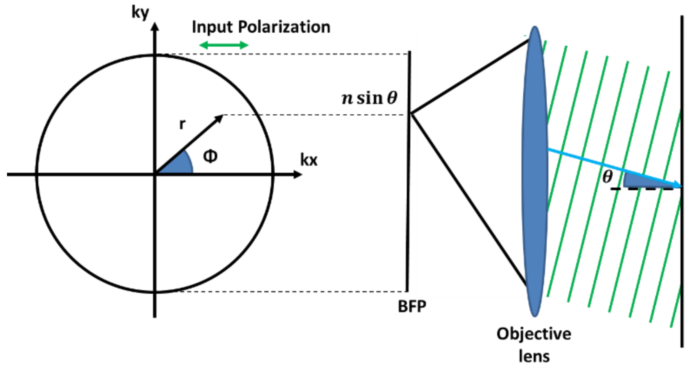

Figure 2-8 shows the schematic diagram of BFP and Plane wave on the sample

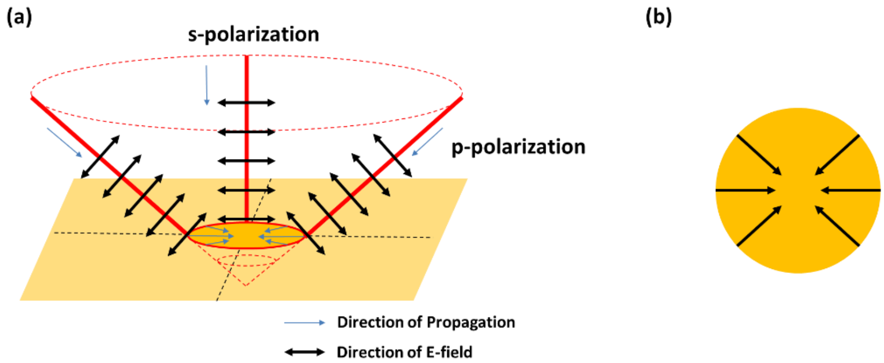

Figure 2-9 shows (a) the schematic diagram of the incident light and (b) the propagation of SP in top view

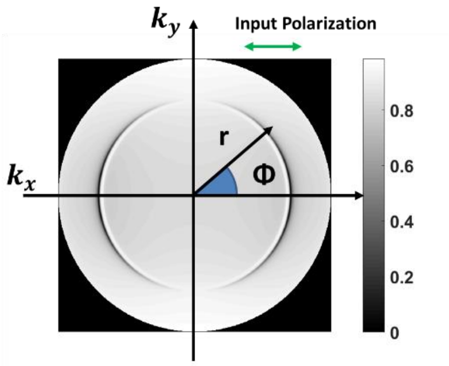

Figure 2-10 shows the simulated intensity on the BFP by linear polarization

Assuming there is a point source on BFP located at $P(r, \Phi) = P(n \sin\theta, \Phi)$, it will provide a plane wave on the sample with an incident angle of θ as shown on Figure 2-8. The maximum angle of the incident angle is limited by the Numerical Aperture, NA, of the objective lens such that $\theta_{max} = \sin^{-1}\left({}^{\mathrm{NA}}/_{n}\right)$ where n is the refractive index of immersion oil for the corresponding objective lens. By illuminating the full aperture of the objective lens, the reflection spectrum of the light will be collected. On the other hand, the reflection spectrum for different polarization is different. As shown on Figure 2-9, the direction of the electric field to the sample refracted by the objective lens is different when the input beam is linear. The electric field of p-polarization can drive the electrons oscillating perpendicular to the sample surface. However, there is no components electric field to drive the electrons in normal direction of the interface. Figure 2-10 show the simulated intensity on the BFP by linear polarization. The point sources along, x-axis and y-axis represent the pure p-polarization and the pure s-polarization respectively. According to the azimuthal angle ϕ, the point sources can be decomposed into p-polarization and s-polarization and the resultant reflection is the complex sum of two components. It can be seen that a clear dip is on x-axis (pure p-polarization) and no dip on y-axis (pure s-polarization). And it should be noted that the SP will propagate to the center when the sample is moving toward to the objective lens as shown on Figure 2-9b.

2.5.2 Non-interferometric SPR microscopes

Non-interferometric SPRM can be classified into two types, namely scanning and wide-field. In general, wide-field imaging is more attractive as the time of image formation for scanning type SPRM can be very long. Scanning-type imaging normally provides better resolution.

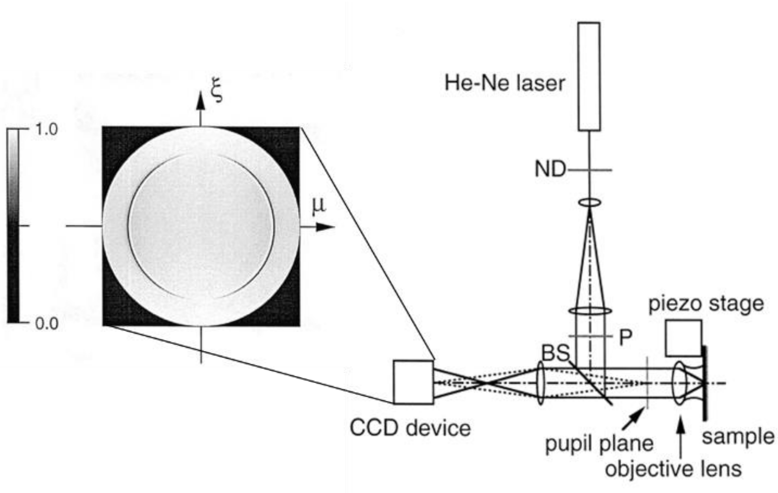

Figure 2-11 shows the schematic diagram and the captured back focal plane image by CCD camera (H. Kano & Knoll, 2000)

In 2000, Kano (H. Kano & Knoll, 2000) proposed a scanning type SPR by tracking the dip position which is corresponding to the resonance condition such as the refractive index variation (see Figure 2-11). The lateral resolution is limited by the noise and interference in the BFP. In 2004, Stabler et al (Stabler, Somekh, & See, 2004) set up a wide-field non-interferometric microscopic to obtain with good lateral resolution of around 1 micron.

2.5.3 Interferometric SPR microscopes

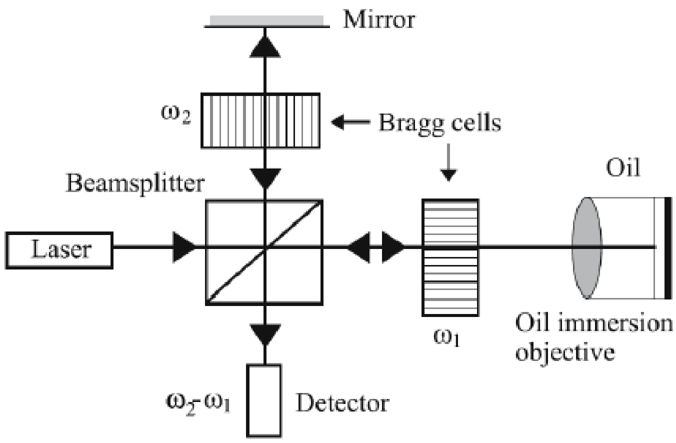

Figure 2-12 Scanning interferometric SPR microscope (M. G. Somekh, S. Liu, T. S. Velinov, & C. W. See, 2000)

In 2000, Somekh et al. (Michael G. Somekh et al., 2000; M. G. Somekh, S. G. Liu, T. S. Velinov, & C. W. See, 2000) proposed an interferometric SPRM with two arms as shown on Figure 2-12. By using a heterodyne interferometer, it showed that the trade-off by detecting the interference signal can be improved. (Pechprasarn & Somekh, 2012). A heterodyne SPR interferometric microscope has been developed which is similar to the confocal microscope to provide better lateral resolution. The output of the system is directly proportional to the amplitude of the incoming field $|V|$ which is stronger than that of confocal microscope ($|V|^2$). The advantage of these approaches over conventional SP microscopy is that that resolution is not limited by the propagation length of SP but now depends mostly on the optical configuration and the sample defocus used to get the necessary contrast. However, there is one drawback of the interferometric SPR microscopes where the alignment of the optical system is complicated which limits the usage in practical situations. (B. Zhang, Pechprasarn, Zhang, & Somekh, 2012). This concept has also been implemented as an optical fibre interferometer, which appears to allow more stable operation (Argoul, Berguiga, & Fahys, 2010).

2.6 Embedded Confocal Surface Plasmon Microscope

It has been very well established that detecting phase of SPR is better than detecting the amplitude or the intensity of SPR due to (i) phase detection is more robust in terms of noise performance, this finding is similar to AM and FM communication theory and (ii) detecting the amplitude requires operation around the position where surface plasmons excitation is strong, which appears as a dip on the back focal plane hence the noise performance becomes a severe issue. (Andrei V. Kabashin, Sergiy

Patskovsky, & Alexander N. Grigorenko, 2009) In order to solve the problem, a spatial light modulator (SLM) based interferometric SPR microscopes is introduced. It can simplify the system and provides a great flexibility on different detection modes compared to the other configurations. Thanks to its simplicity in optical setup, this makes it more attractive and suitable for commercialization.

2.6.1 V(z) Scanning

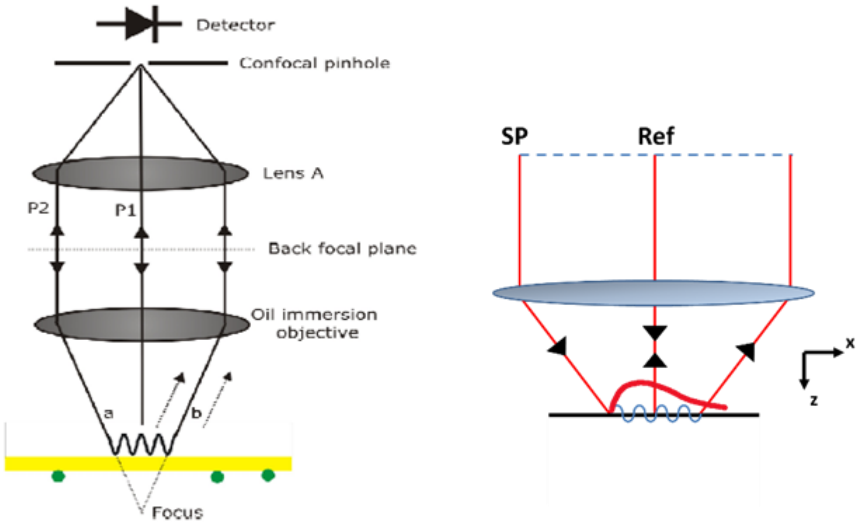

Figure 2-13 Schematic Diagram to show reference signal and surface plasmon signal, showing the principal contributions to the signa in the SPRM. Note that although radiation occurs continuously only rays appearing to come from the focus are detected at the pinhole.

Recently, Zhang et al (B. Zhang, S. Pechprasarn, J. Zhang, et al., 2012) showed that confocal SPRM provides a simpler and more stable alternative to interferometric SP imaging.(Bei Zhang et al., 2012). The plane-wave representation of the output signal of this system can be written as:

$$\mathrm{I(z)} = |\mathrm{V(z)}|^2 \tag{2-10}$$

$$= \left| \int_0^{2\pi} \int_0^{s_{max}} P_{in}(s) P_{out}(s) \left[cos^2\phi \; r_p(s) + sin^2\phi \; r_s(s) \right] \exp(2jnkzcos\theta) \; sdsd\phi \right|^2$$

$$= \left| \int_{\Omega} P^2 \, E_{BFP} \, e^{i\Phi} d\Omega \right|^2$$

Where I(z) is the output signal and V(z) is detected field along optical axis z. s is the sine of the incident angle ($\sin\theta$). P_{in} and P_{out} are input and output pupil functions. r_p and r_s are the amplitude reflection coefficients for p-polarization and s-polarization respectively. θ is the incident angle and ϕ is the azimuthal angle.

Due to the confocal arrangement as shown on Figure 2-13, only the paths that appear to come from the focus can pass through the pinhole. On the other hand, they show that SP can be excited at position 'a' and reemit at position 'b'. Hence, only the light from the paths, P1 and P2, are collected. As the rate of the phase change with respect to the defocus distance z is different so that the phase difference between the light from P1 and P2 will change as defocus distance z changes. It will form ripple pattern on negative defocus distance z which can be approximated by the equation below which can be expressed as:

$$\Delta \mathrm{z} = \frac{\lambda}{2n(1 - cos\theta_p)} \tag{2-11}$$

They also proved that the effect of mechanical defocus can be achieved by varying the curvature on the SLM.(Bei Zhang et al., 2012).

2.6.2 Beam Profile Modulation

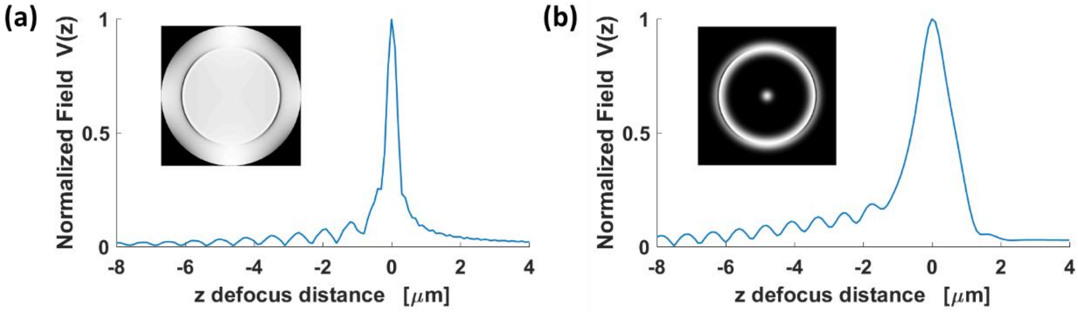

Figure 2-14 show the simulated V(z) (a) without amplitude pupil function and (b) with amplitude pupil function

One of the key components of the embedded confocal SPRM is the spatial light modulation (SLM) which can modulate the phase of the incoming beam. For other applications, SLM can be used for wavefront correction. (Love, 1997). In reverse, we can modulate a wavefront with different shapes to match our applications. For example, if we put the pattern of curvature on the SLM, then the SLM will act like a lens. As a result, the focus can be moved along optical axis by an amount dependent on the curvature. This is the principle we use to perform scanning along the optical axis (z axis) on the microscope. By aligning the SLM on the back focal plane of the objective lens, the beam profile at different incident angles can be modulated. By modulating the phase in the back focal plane, many sophisticated optical operations can be achieved, such as, scanning on x y and z axes and amplitude modulation as shown on Figure 2-14.

2.6.3 Phase Stepping

In 2013, Zhang et al, demonstrated that the SP excitation angle can be recovered by an embedded phase stepping confocal interferometry (Bei Zhang, Suejit Pechprasarn, & Michael G. Somekh, 2013), we can recover the angle of incidence by phase stepping technique. Firstly, it should be noted that there are two main contributions to the V(z), namely, the plasmon signal beam and the reference beam as described above. Furthermore, we can model two sources on the back focal plane into two simplified vectors, signal vector **S** and reference vector **R**.

$$I = |V(\mathrm{z})|^2 = |R|^2 + |S|^2 + 2|R||S|\cos(\emptyset) \qquad \text{(2-12)}$$

Where I is the intensity.

The intensity of the V(z) is the vector sum of signal vector and reference vector. In order to extract each relative phase difference Ø along V(z), a phase stepping technique is conducted. A set of equations are formulated as follows:

$$I_n = |R|^2 + |S|^2 + 2|R||S|cos\left(\emptyset + n\frac{\pi}{2}\right) \quad \text{for n} = 0,1,2,3 \qquad \text{(2-13)}$$

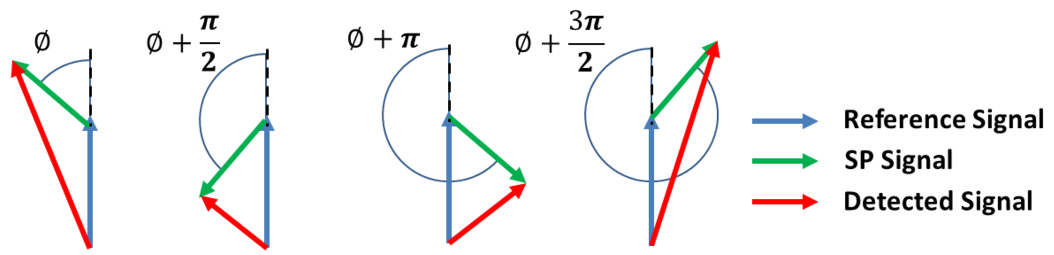

Figure 2-15 Schematic phase diagram showing the effect of phase stepping in the SPRM. The red arrow is the resultant field of the two contributions to the output signal. The blue reference is equivalent to the signal from P1 in Figure 2-13 and the green SP phase represents the signal from P2. In the actual system, the measured signal is proportional to the square of this field

As shown on Figure 2-15, we obtain 4 intensity measurements by phase-stepping the SP signal by 0, 90, 180 and 270 degrees. By solving the equations, the relative phase Ø between two main interfering beams can be computed by

$$\tan^{-1}[(I_3 - I_1)/(I_0 - I_2)] \qquad \text{(2-14)}$$

On the other hand, The relation between the $\emptyset(\mathrm{z})$ and the plasmonic angle is expressed as (Bei Zhang et al., 2013):

$$\emptyset(z) = 2kz\left(1 - cos\theta_p\right) + \beta \tag{2-15}$$

And hence, the gradient of $\emptyset(z)$ with respect to defocus distance z is expressed as:

$$\Delta k = \frac{d\emptyset}{dz} = 2k\left(1 - cos\theta_p\right) \tag{2-16}$$

By rearranging the equation (2-16),

$$\theta_p = \cos^{-1}\left[1 - \frac{\lambda \frac{d\emptyset}{dz}}{4n\pi}\right] = \cos^{-1}\left[1 - \frac{\Delta k}{2nk_0}\right] \tag{2-17}$$

Where Δk is the beat frequency between k_{sp} and k_{ref}.

Therefore, the plasmonic angle θ_p can be recovered by $\frac{d\emptyset}{dz}$ once the phase shifts on *V*(z) curve are obtained.

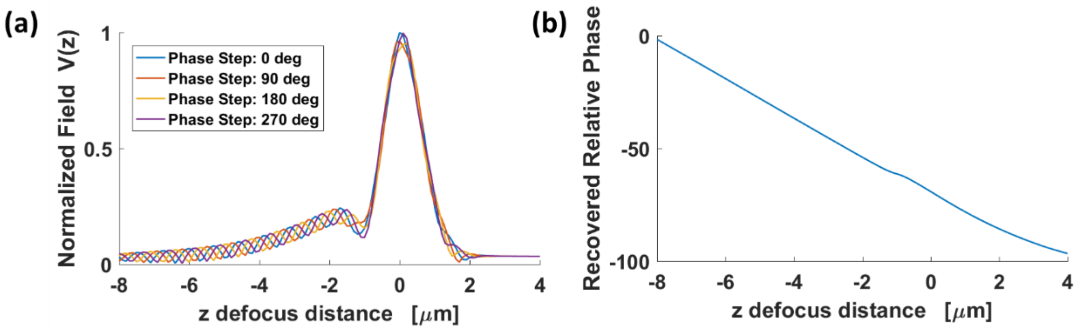

Figure 2-16 show (a) simulated V(z) on 47 nm Gold surface with amplitude pupil function with the amplitude pupil function shown on Figure 2-14b and (b) the recovered relative phase from (a)

To demonstrate the phase stepping technique, V(z) curves with 4 different phase steps are simulated as shown on Figure 2-16 (a). By applying the equation(2-14), the phase difference along defocus distance between two signals are recovered as shown on Figure 2-16 (b). By selecting the proper window with good linearity, the gradient of the relative phase is recovered. For example, $\frac{d\emptyset}{dz} = 8.24\ [\frac{rad}{\mu m}]$, then the recovered excitation angle θ_p according to (2-17), which is 43.37 deg. As a result, the surface plasmon k-vector can be recovered.

2.7 Current version of Surface plasmon microscope

Up to this point, the embedded confocal SPRM recover the excitation angle by a series of intensity measurement resulting in long acquisition time. For long acquisition time, it will introduce lots of unwanted noise such as drifting from temperature variation. It is expected that the system can be more robust if the acquisition time is reduced, this will be one output from the thesis.

The recovered phase in our confocal is the relative phase between two main contributions, namely the reference signal and the SP signal. Another output from the thesis will be to develop techniques to examine the form of the phase variations in more detail. We will show that the phase information in fact provide lots of useful information such as propagation and attenuation properties of SP. (The details will be discussed in Chapter 5).

2.8 Background of Phase Retrieval Algorithm

In chapter 6 of this we apply a phase retrieval algorithm to recover the complex field on the BFP of the objective. Therefore, it is worth to reviewing the background of the phase retrieval algorithm as well. In this study, the Ptychographical iterative Engine (PIE) was used as our phase retrieval algorithm to recover the complex field on the BFP. The algorithm was modified, but the overall algorithm is the similar.

2.8.1 History of PIE

In 1972, Gerchberg and Saxton suggested a practical phase retrieval iterative algorithm based on the FFT (Gerchberg & Saxton, 1972). The principle of the conventional Gerchberg and Saxton (GS) algorithm is to satisfy the intensity at two planes. The free variable that is used to satisfy these constraints is the phase. The block diagram of the algorithm is shown below

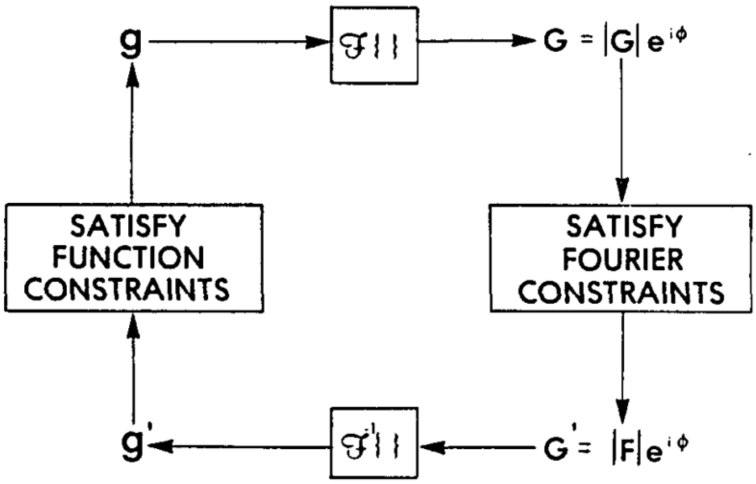

Figure 2-17 Block diagram of GS Algorithm (Fienup, 1982)

In the GS algorithm, for the k-th iteration, the input guess g on the object domain is transformed into the Fourier Domain. Then amplitude of the transformed function |G| is replaced by the measured amplitude |F| in order to satisfy the Fourier constraints. The corrected function g’ on object domain is obtained by inverse transforming the corrected function G’ on the Fourier domain. To satisfy the constraints on the object domain, the amplitude of g’ is replaced by the measurement function as well in order to have new (k+1)-th input guess g.

In 1982, Fienup (Fienup, 1982) summarized the phase retrieval algorithms including the error-reduction algorithm (GS algorithm), steepest-descent method and conjugated-gradient method. He also proposed the Input-Output Algorithm. In the algorithm, Fienup made a small (and often significant) modification to the standard GS algorithm by grouping the operations on the Fourier domain as shown on Figure 2-18 and regarding these operations as a non-linear system with an input g and an output g'.

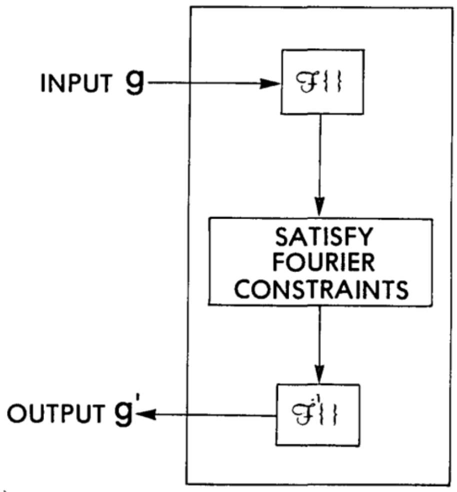

Figure 2-18 Block diagram of the system for the input-output algorithm (Fienup, 1982)

It is clear that the output g' satisfies the constraints on Fourier domain. Therefore, the solution can be found when it also satisfies the constraints on the object domain. The main point in this algorithm is to emphasize that the input g is not restricted to satisfy the constraints on the object domain. In this arrangement, it can give a great flexibility to modify the algorithm in order to improve the rate of the convergence of the algorithm.

On the other hand Hoppe (Hoppe, 1969) proposed the concept of ptychography for use in electron microscopy. The overlapping illumination provides the redundancy in the data allowing robust solution of the phase. (Andrew M. Maiden & Rodenburg, 2009). In 2004 and 2005, Faulkner and Rodenburg (Faulkner & Rodenburg, 2004,

2005) applied the iterative phase retrieval algorithms (as described just above) for moveable illumination microscopy by a series of diffraction patterns. The multiple constraints eliminate the ambiguities of the recovered phase and allow a large recovered area of the object. Up to date, a variety of modifications to the ptychography algorithm have been proposed to improve the performance of the algorithm (Beckers et al., 2013; Hurst, Edo, Walther, Sweeney, & Rodenburg, 2010; A. M. Maiden, Humphry, Sarahan, Kraus, & Rodenburg, 2012; Andrew M. Maiden & Rodenburg, 2009; Andrew M. Maiden, Rodenburg, & Humphry, 2010; Shenfield & Rodenburg, 2011)

2.8.2 Conventional Algorithm of PIE

There are various types of ptychography. For the ptychography algorithm, it is not necessary to relate the two planes by a Fourier relationship. (Faulkner and Rodenburg 2004). Any transform that represents the relationship between two planes can be used, for example, the free space propagator used by Allen. (Allen et al. 2001) However, in most cases, they consist of the subroutine described below

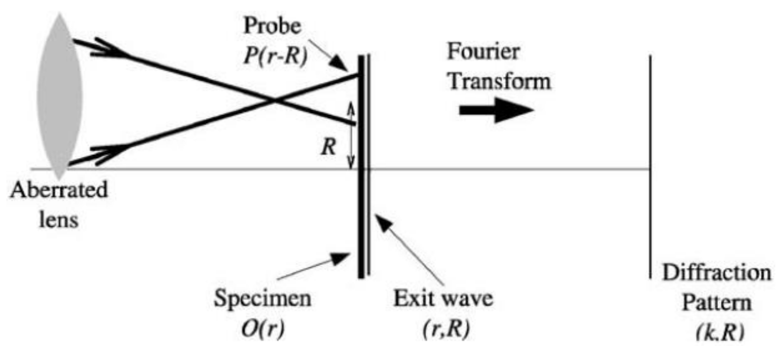

Figure 2-19 shows the schematic diagram of each plane (Faulkner & Rodenburg, 2005)

The guess object function $O(r)$ of the specimen can be expressed in a complex field function. The illumination function (or called Probe) $P(r-R)$ represents an illumination profile. The exit function $\psi(\boldsymbol{r},\boldsymbol{R})$ is the product of $O(r)$ and $P(r-R)$ which will project on diffraction plane. By moving the relative lateral position of $O(r)$ and $P(r-R)$, a series of diffraction intensities corresponding to the probe position will be recorded. Then, as mentioned above, the guess object function will be iteratively updated between the object plane and the corresponding Fourier plane (or called diffraction plane) as shown in the Figure 2-19.

The algorithm can be expressed as follows

1) Guess object function, $O_{g,n}(\boldsymbol{r})$
2) Exit wavefunction $\psi_{g,n}(\boldsymbol{r},\boldsymbol{R}) = O_{g,n}(\boldsymbol{r})P(\boldsymbol{r}-\boldsymbol{R})$
3) Fourier Transform $\Psi_{g,n}(\boldsymbol{k},\boldsymbol{R}) = \mathcal{F}\left[\psi_{g,n}(\boldsymbol{r},\boldsymbol{R})\right]$
   Where k is the usual reciprocal space coordinate
4) $\Psi_{c,n}(\boldsymbol{k},\boldsymbol{R}) = |\Psi_{measured}(\boldsymbol{k},\boldsymbol{R})|\angle\theta_{g,n}(\boldsymbol{k},\boldsymbol{R})$
5) Inverse transform $\psi_{c,n}(\boldsymbol{r},\boldsymbol{R}) = \mathcal{F}^{-1}\left[\Psi_{c,n}(\boldsymbol{k},\boldsymbol{R})\right]$
6) Update guessed object wavefunction
   $O_{g,n+1}(\boldsymbol{r}) = O_{g,n}(\boldsymbol{r}) + \frac{|P(\boldsymbol{r}-\boldsymbol{R})|}{|P_{max}(\boldsymbol{r}-\boldsymbol{R})|}\frac{P^*(\boldsymbol{r}-\boldsymbol{R})}{(|P(\boldsymbol{r}-\boldsymbol{R})|^2+\alpha)}\beta\left(\psi_{c,n}(\boldsymbol{r},\boldsymbol{R}) - \psi_{g,n}(\boldsymbol{r},\boldsymbol{R})\right)$

   $\frac{|P(\boldsymbol{r}-\boldsymbol{R})|}{|P_{max}(\boldsymbol{r}-\boldsymbol{R})|}$ term for normalization
7) $\mathrm{SSE} = \frac{\left(|\Psi_{measured}(\boldsymbol{k},\boldsymbol{R})|^2 - |\Psi_{g,n}(\boldsymbol{k},\boldsymbol{R})|^2\right)^2}{N}$

In step 1, a guess object function $O_{g,n}$ is defined by a constant amplitude with random phase ranging from -π to π. Then, in step 2, the exit wavefunction is computed by multiplying the guess function and a probe. In step 3, by Fourier-transforming the exit wavefunction $\psi_{g,n}$ on object plane, the wavefunction on the diffraction plane is obtained. In step 4, the corrected wavefunction $\Psi_{c,n}$ on the diffraction plane can be obtained by replacing the estimated modulus by the measured modulus $|\Psi_{measured}|$ on the image plane (which is corresponding to the probe used). In this step, the measured modulus can be regarded as a constraint for the algorithm. It also means that the constraint on the diffraction plane is satisfied. Then, in step 5, the corrected exit wavefunction $\psi_{c,n}$ can be obtained by inverse Fourier-transforming $\Psi_{c,n}$. The updating function can be expressed in step 6. The new guess of the object function is updated by the $\frac{|P(\boldsymbol{r}-\boldsymbol{R})|}{|P_{max}(\boldsymbol{r}-\boldsymbol{R})|}\frac{P^{*}(\boldsymbol{r}-\boldsymbol{R})}{(|P(\boldsymbol{r}-\boldsymbol{R})|^{2}+\alpha)}\beta\left(\psi_{c,n}(\boldsymbol{r},\boldsymbol{R})-\psi_{g,n}(\boldsymbol{r},\boldsymbol{R})\right)$. The learning rate β is to control the feedback to the new guess. In our experiment, the learning rate will be varied from 0.8 to 0.2 to obtain a satisfactory result. (The effect of the learning rate will be discussed in the section of "Learning Rate" in Chapter 6) Finally, the convergence of the algorithm can be monitored by the sum of the intensity difference between the measured intensity and guess intensity on image plane as expressed in Step 7.

2.9 Summary

In this chapter, we reviewed the fundamentals and the properties of the SP. SP can only be excited by the light beam in p-polarization and it propagates along the interface of the dieletric and metallic layers when excited. We also demonstrated that SP can only be excited by special configuration such as Otto and Kretschmann configuration. As discussed, we will use Kreschmann configuration for our study as Kretschmann configuration is more suitable for binding measurement. Then, we reviewed that the development of the SPR sensing from prism-based to objective-based SPR microscopy for better lateral resolution. We addressed that the lateral resolution can be further improved by the confocal SPRM. Finally, we addressed the need of the improvement on SPRM such as the time for data acquisition. On the other hand, we reviewed the history and the detailed steps of the PIE algorithm.

Chapter 3 – Experimental material and methods

In this chapter, I will discuss the optical setup and the tools for investigating the resolution and sensitivity of SPR microscope. As two similar optical systems are involved in this thesis, I will explain the common materials and the methods used on both systems first. Then, the optical configuration for SLM based SPRM will be discussed lens for Chapter 4 and 5 as they are generally the same involving a SLM conjugate on the BFP of the objective. Finally, the system for complex BFP retrieval by ptychographic algorithm will be addressed. The system may be slightly different from the setup in Chapter 4 and 5. The details configuration will be discussed in the coming section.

3.1 Common materials and methods

Kano(Hiroshi Kano et al., 1998) showed how SP can be excited by a focused laser beam in a high NA objective manner and hence all angular response of SP can be collected in an self-contained system. In this configuration, the system is not complicated and easy to align. As mentioned in Chapter 2, a robust signal such as excitation angle of SP can be accurately extracted by the V(z) technique.

3.1.1 High NA objective lens

In this project, we will keep the high NA objective lens as our fundamental component. We will perform different strategies to extract the information such as accurate excitation angle and the relative phase shift from the reflection spectrum.

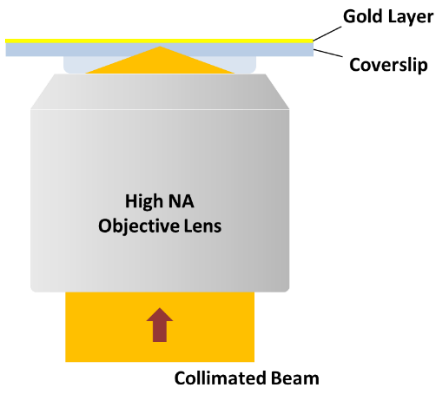

Figure 3-1 shows the schematic diagram of the illumination of a high NA SP microscope

The objective lens used in this study is Nikon 1.49NA objective lens (CFI Apochromat TIRF 60XC Oil-immersion type). It not only allows us to illuminate the sample with very high incident angles, with linear incident input polarizations different polarization states on the sample from pure p- to pure s- can be also excited. The focal length of the objective lens can be calculated as below

$$\mathrm{f} = \frac{\text{Tube Length}}{\text{Magnifcation}} = \frac{200\ \text{mm}}{60} = 3.33\ \text{mm}$$

And hence, the clear aperture of the objective lens is D = 2f x NA = 10 mm.

3.1.2 Beamsplitter Selection

In general, there are three types of beamsplitters, namely, cube form, plate form and pellicle form.

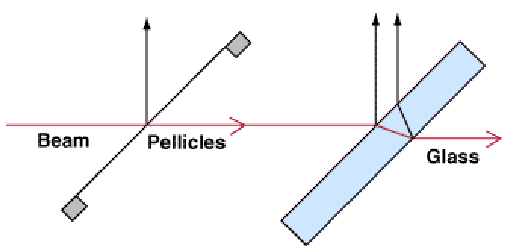

Figure 3-2 shows the ray diagram on pellicle beamsplitter and plate beamsplitter (EdmundOptics, 2018)

For classical beamsplitters such as cube and plate beamsplitter a ghost image will be created by the reflection on the 2nd surface. As the measured quantity in our system is intensity which is the interference signal between reference signal and SP signal. The quality of the data will be degraded if additional source of ghost image is involved. Pellicle beamsplitter consists of a nitrocellulose membrane which virtually eliminates the ghosting. Therefore, a pellicle beamsplitter is used for our system in this project. However, it should be noted that the pellicle beamsplitter is fragile and sensitive to acoustic noise. Therefore, the experimental procedure should be conducted in an enclosed environment.

3.1.3 Confocal Pinhole and pixelated CMOS Camera

In the embedded confocal SPRM, our group (B. Zhang, S. Pechprasarn, J. Zhang, et al., 2012) demonstrated that proper size of the confocal pinhole is crucial for the confocal measurement.

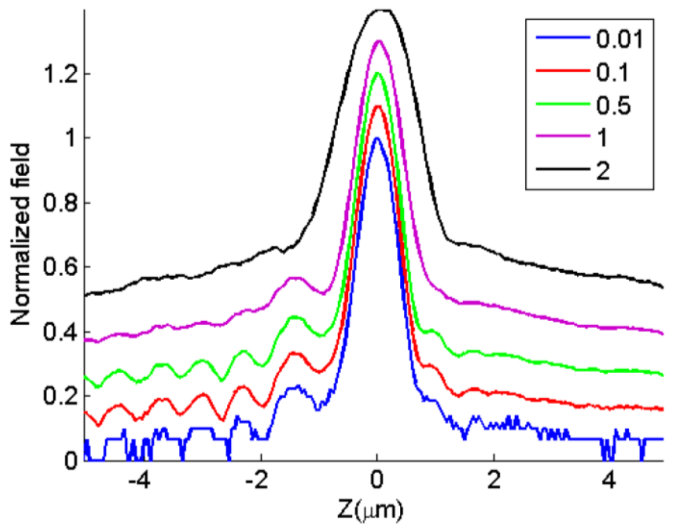

Figure 3-3 Experimental V(z) curves on 50 nm gold sample with 2nm adhesion layer of chromium for different pinhole radii. (Bei Zhang et al., 2012)

Figure 3-3 is the experimental V(z) curves on 50 nm gold sample obtained by varying the size of the confocal pinhole (the value is the ratio of the pinhole radius to the Airy disk radius). When the size of the pinhole is too large, the detector will receive the emitted SP from a wider range positions on the sample surface. These will produce ripples with different phase, so that the oscillations cancel. In other words, as the pinhole size increases the system loses the confocality. This is shown in Figure 3-3 when the ratio is greater than 0.5. On the other hand, when the size of the pinhole is too small (e.g. ratio = 0.01), the detected light is too weak resulting in poor signal-to-noise ratio. The experiment showed that the ratio of size ranging from 0.1 to 0.5 is a proper choice to balance between the confocality and signal-to-noise ratio.

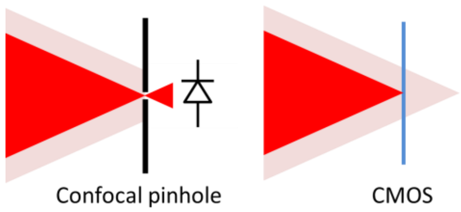

Figure 3-4 shows the confocality of confocal pinhole and CMOS camera

In our system, 633nm HeNe laser and 1.49 NA objective lens are adopted. Therefore, the diameter of the Airy disk is round 518 nm. In this study, the confocal pinhole and the photodetector are replaced by a CMOS camera which served as a controllable pinhole. By summing the intensity within the designed region on the camera, the summed intensity essentially is the signal detected by the photodetector after confocal pinhole as shown on Figure 3-4. Considering the magnification of the system is around 2250, the size of the magnified Airy on the camera is around 1.2 mm. For a camera with pixel size of 5.3 µm, more than 200 pixels can be used to represent the point spread function, which greatly improves the SNR.

3.1.4 Selection and Preparations of Sensors

For HeNe 633nm layer, the typical thickness for exciting SP is about 50 nm. In this section, a simulation is conducted to help us to select proper parameter for biosensing.

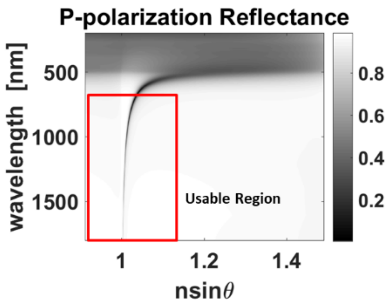

Figure 3-5 shows the resonance dip against wavelength on 50 nm Ag sample

There are three observations can be obtained from Figure 3-5. First, the dip of the reflection spectrum can be captured by objective lens with numerical NA of 1.49. Second, the SP cannot be excited when the input wavelength is too short, beyond the plasmon resonance frequency the permittivity becomes positive and the metal looks more like a dielectric, so plasmonic effects are not observed. It should also be noted that the excitation angle of the SP decreases as the wavelength increases. There are therefore advantages in using infrared light source to excite SP for biosensing. (Limaj et al., 2016). This can be particularly useful in objective lens surface plasmon microscopy as the demands on the very high numerical aperture lens become less severe. However, on one hand, the comprehensive optical components for infrared are expensive, this is particularly true for detectors operating above about 1.1 microns wavelength where silicon-based detection is not applicable. On the other hand, the alignment of the optical system is challenging as it is invisible to our eyes. Therefore, we use HeNe laser to demonstrate the technique of detecting phase. It should be emphasized that the technique in this study could also be used in the infrared spectrum.

3.1.5 Wide-Field

Although confocal image can provide higher sensitivity, the process of data acquisition is time consuming. In order to have quick overview of the sample, it is more convenient if we can get wide-field image of the sample and then move the sample to the region of interest.

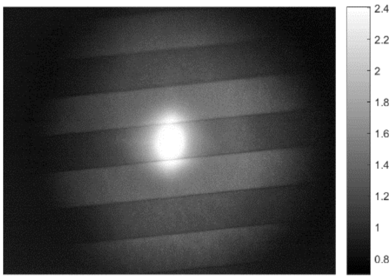

Figure 3-6 shows the wide-field image in log scale on the Ronchi grating pattern in period of 50 microns

In order to obtain a wide-field image, we can apply the principle proposed by Stabler et al. (Stabler et al., 2004), the coherence of the beam can be destroyed by putting rotating diffuser between the optical path. Then the sample will be illuminated randomly in spatial domain. Then, a wide-field image is obtained as shown in Figure 3-6, once the region of interest is confirmed, the rotating diffuser can be removed from the system. Then, V(z) measurement can be performed to obtain highly sensitive image from the sample. It should also be noted that the field of view on the sample is around 180 microns, determined by the field of view of the microscope objective.

3.2 SLM based Surface plasmon microscope

3.2.1 Configuration of SLM based Surface plasmon microscope

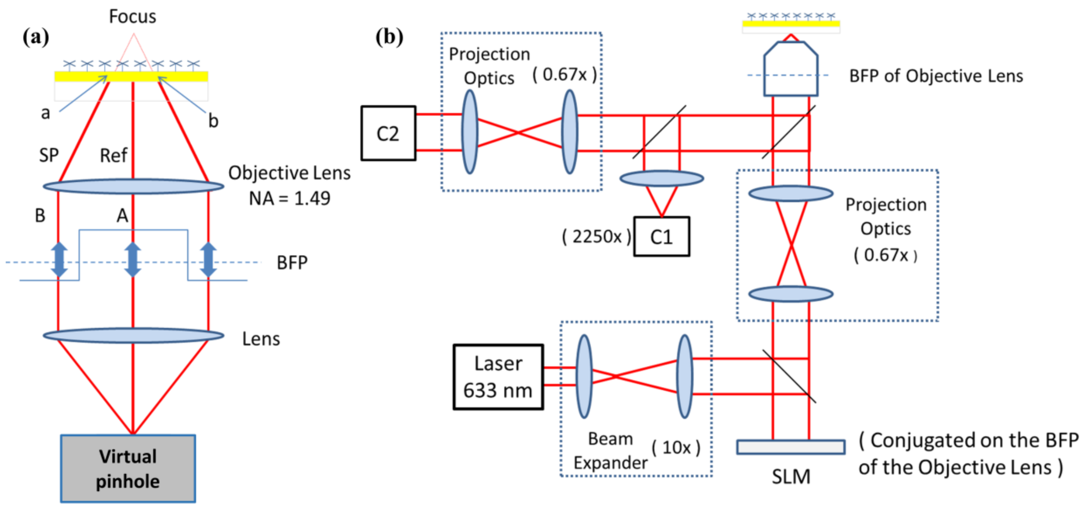

Figure 3-7 (a) Simplified schematic diagram of the confocal plasmon microscope, (b) Detailed schematic diagram.

As shown on Figure 3-7, in general, He-Ne Laser (Melles Griot, linearly polarized version) is used as a light source. The beam expander formed by two achromatic doublet lenses is used to expand the beam to fully cover selected region of the SLM. In order to have more pixels to modulate the back focal plane of the objective, the projection unit is used to match the size of the aperture of the objective (The details of the projection unit will be discussed in the later in this section. After passing through the objective, the beam will focus on the surface of the sensor and then reflects through the objective. The first CMOS camera is aligned on the conjugate back focal plane in order to monitor the change of the dip position on back focal plane. Finally, the beam will be focused and magnified on the second CMOS camera (image plane camera).

3.2.2 Spatial Light Modulator

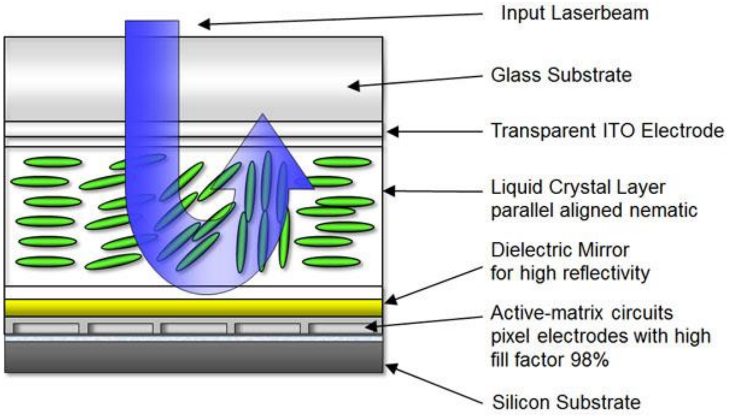

Figure 3-8 Schematic diagram the structure of Spatial Light Modulator (Hamamatsu, 2015)

The liquid crystal layer is embedded between the electrodes so that the orientation of the liquid crystal can be controlled by applying different voltages as the schematic diagram shown on Figure 3-8. As the orientation of the liquid crystal is changed by the applied voltage, the refractive index along the normal direction is changed according to the orientation of the Liquid crystals. The incoming beam will experience longer (or shorter) optical path length within the liquid crystals when the direction of liquid crystal is oriented parallel to the incident beam. This provides the potential to change the phase of the reflected light, typically by over 2π radians.

The phase shift of the returning optical beam depends on the incident wavelength and even at a specific wavelength the phase shift is not linear with the voltage, so that it necessary to perform a calibration before the SLM can be used for quantitative measurements. The details of calibration of the SLM will be discussed below.

3.3.3 Calibration of SLM

The calibration process is conducted to accurate control the phase of the SLM using an interferometer as shown on Figure 3-9.

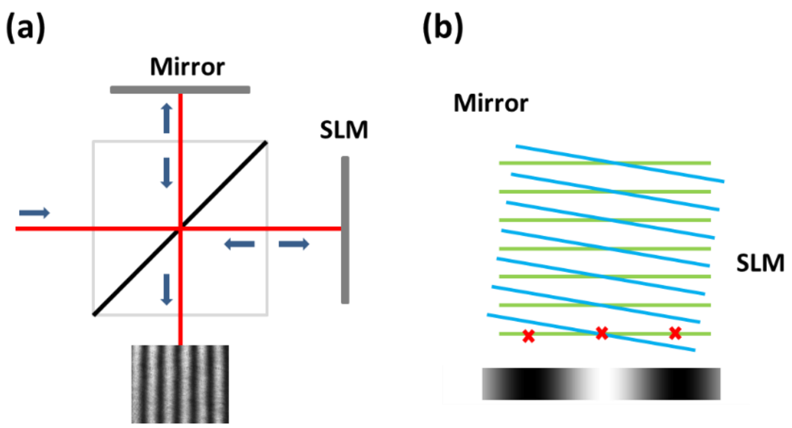

Figure 3-9 (a) shows schematic diagram for calibration of SLM and (b) interference pattern integrated by two plane waves

A clear interference pattern is obtained by two overlapping plane waves. The bright part occurs when they are in phase and the dark part is when they are antiphase. By offsetting the phase on SLM, the fringes can be move laterally.

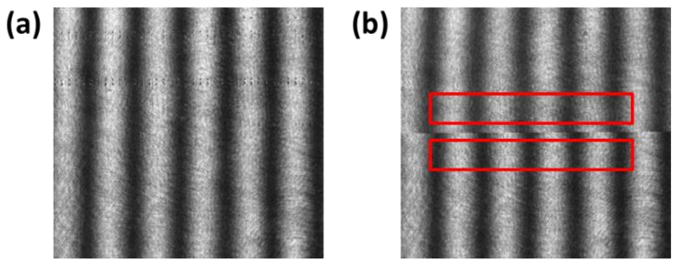

Figure 3-10 (a) shows interference signal and (b) the split interference pattern

In the calibration process of the SLM, the phase response for different grayscale level to the SLM will be examined. First, the SLM will be divided into two parts, for example, the upper part and bottom part. Then, keeping the phase on one part is fixed, e.g. grayscale level = 0 and changing the grayscale level on another part from 0 to 255. As a result, the interference pattern will also be split into two parts as shown on Figure 3-10(b). For each grayscale level, the interference pattern will be cropped within the region of interest (the red rectangle on Figure 3-10(b)). Within the red rectangles, the interference signal will be averaged along vertical direction. Then, the phase is extracted by Fourier transforming. By comparing the phase difference between the upper and lower fringes the relative phase between the input grayscale level and grayscale level =0 can be obtained. The phase values obtained can then be related to the grayscale levels imposed on the SLM.

3.3.4 Projection Optics between SLM and BFP of objective lens

The size of the SLM and the clear aperture of the objective lens are 7.1 mm and 10mm respectively. To fill the aperture of the objective lens, the minimum magnification is 10mm/7.1mm ≈ 1.4x. Hence, 100/150 and 125/200 lenses are a reasonable pair to perform this task.

3.3 BFP Ptychography system

In the later parts of the thesis we discuss the development of ptychography based methods, this requires different parts of the back focal plane of the objective to be projected to a transform (defocused image) plane. We discuss here the slightly unusual way we produce the different scenes with a Ronchi grating.

3.3.1 Design of Rotation Stage

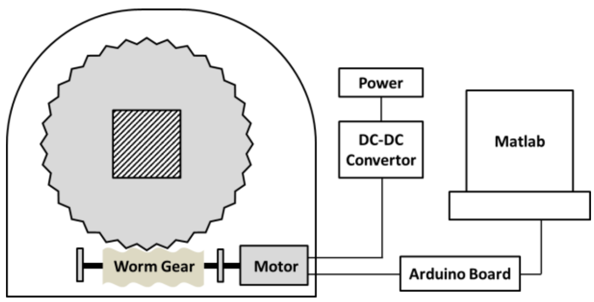

Figure 3-11 shows schematic diagram of the rotation stage

A customized rotation stage is designed to control the orientation of the Ronchi grating as shown on Figure 3-11. For the operation, Matlab will send the command with the rotation information to Arduino Board through serial port. Arduino Board will convert the information into a series of pulse to drive the stepping motor. Rotation of the stepping motor depends on the number of pulses received. Then, the stage attached with the Ronchi grating attached will be rotated driven by the worm gear.

3.4 Summary

In this chapter, we showed the experimental material and methods to implement our ideas in this study. As there were two systems in my study, I first discussed the common materials and method to implement the ideas. For example, the high NA objective lens was used to measure the angular response of the SP in a compact form. Then, we discussed the implementation of the SLM-based SPRM. SLM was inserted into the system for phase-modulation. In addition, we discussed the principle and the calibration of the SLM. Finally, we discussed the design of the rotation stage for the BFP Ptychography. The key components used in this thesis are summarized in Appendix II.

Chapter 4 - Advanced Pupil Function Engineering in SPRM

The embedded confocal SPRM is a simplified version of the original interferometric SPRM simplifying the original separated two arm interferometric system into a single arm, with both paths embedded in the arm. Although the configuration of the confocal SPRM is greatly simplified, the signal to noise is not as good as that of interferometric SPRM. In interferometric SPRM, not only is the recorded signal amplitude, but the reference beam is also provided from the 2^{nd} detection arm resulting in a strong integrated signal. In embedded confocal SPRM, the reference signal beam is provided from the normal reflection from the sample surface. The principle of recovering the excitation angle is by V(z) measurement. It is clear that the signal returning to the confocal pinhole becomes weak as the defocus distance increases resulting low signal to noise ratio. It will be a great advantage if the amplitude of the collected signal can be increased.

Integrating the SLM into the system improves the stability of the system by reducing the number of mechanical parts, it also improves the flexibility of the system, however, the SLM itself does not necessarily improve the signal from the system. We inserted the SLM on the conjugated BFP of objective lens. Simple phase profiles such as linear gradient or curvature were used to control the scanning and defocusing operations. And a phase-stepping algorithm is used to extract quantitative information with reasonably good signal to noise ratio. However, the intrinsic problem of low amplitude of reference beam was not yet solved.

In this chapter, we will show the amplitude of the reference beam can be increased by advanced phase modulation technique resulting good signal to noise ratio during acquisition. Also, the detailed description of the $d\emptyset/dz$ will be discussed. Finally, the experimental results using a controllable reference beam is also discussed. In addition, we will demonstrate how optical vortex modulation and Hilbert transform can be applied to extract the phase against defocus distance.

4.1 Background

In the chapter 2, we model the detected signals from the embedded confocal SPRM coming from two main distributions, namely, SPR signal and Reference signal. The reference signal is the normal reflection from the surface. Now, individual pupils are designed for surface plasmon and reference signals to understand the contribution of these components.

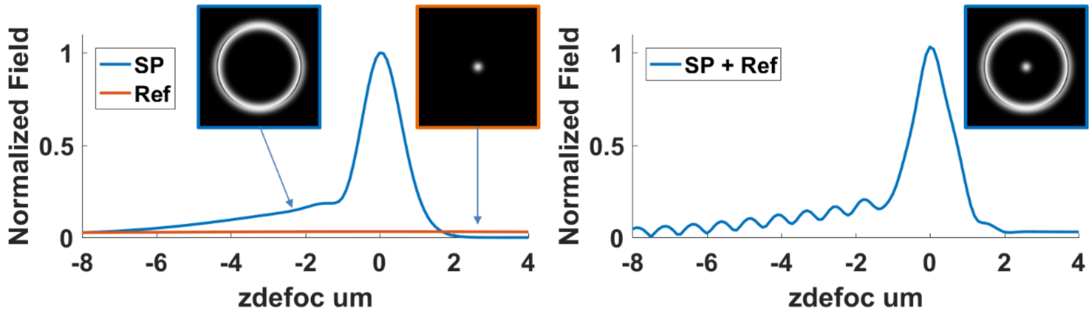

Figure 4-1 shows V(z) curve on 50 nm gold with different pupil function (a) pupil allowing the SP only to pass (b) shows a reference beam and SP signal where the interference signal is observable at negative defocus.

As shown in Figure 4-1, the field of the reference beam is very low compared with that of SP which will affect the signal to noise ratio of the integrated signal. Increasing the signal of the reference beam will make the measurement more attractive. In the past, the V(z) curve is obtained by defocusing the sample. There is no way to control on the reference beam. Recently, Zhang and Somekh (B. Zhang, S. Pechprasarn, J. Zhang, et al., 2012) integrated the embedded confocal SPRM with SLM to measure V(z) without mechanical movement leading to better stability. Initially, they measured the V(z) curve in the same way without enhancing the reference beam. The V(z) obtained with this configuration is the same as the conventional embedded confocal SPRM. However, with this configuration, it is possible to modulate the pupil function with more advanced pattern enabling a flexible way to control the measurement.

4.2 Reference Beam Modulation on BFP

In this section, several modulation strategies will be discussed from amplitude modulation to phase modulation to improve the signal to noise ratio and functionality of the integrated signal. The analysis involves the impact on the amplitude of the reference beam and the recovered phase of the detected signal.

4.2.1 Modulation 1– Amplitude modulation on Reference Beam

The logical choice to enhance reference beam is to use wider amplitude pupil function as shown on Figure 4-2.

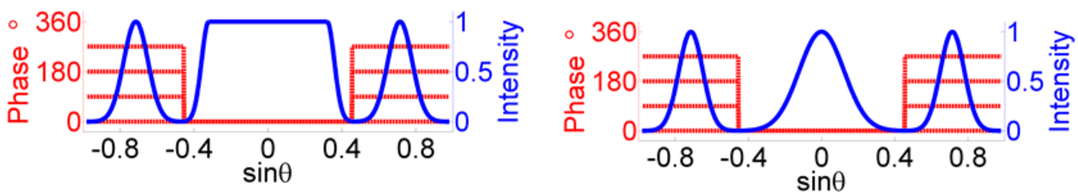

Figure 4-2 shows the amplitude pupil function in different size of reference beam. (a) wide reference beam and (b) standard reference beam

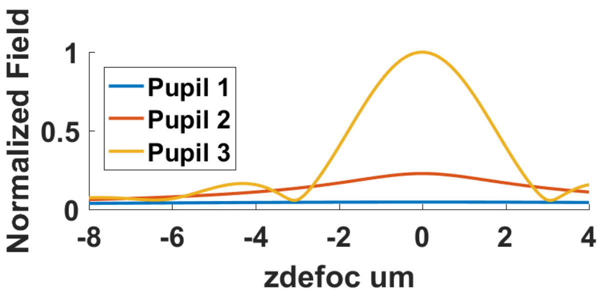

Figure 4-3 shows the V(z) of Reference signal with different width

As shown on Figure 4-3, it is obvious that the reference beam is now amplified. However, there is a ripple generated on the V(z) with pupil function 3. The V(z) with pupil function 2 seems better as there is no clear ripple on the V(z) curve. However, the amplitude decreases as defocus distance increases. It seems it will introduce additional nonlinear effect on the detected signal.

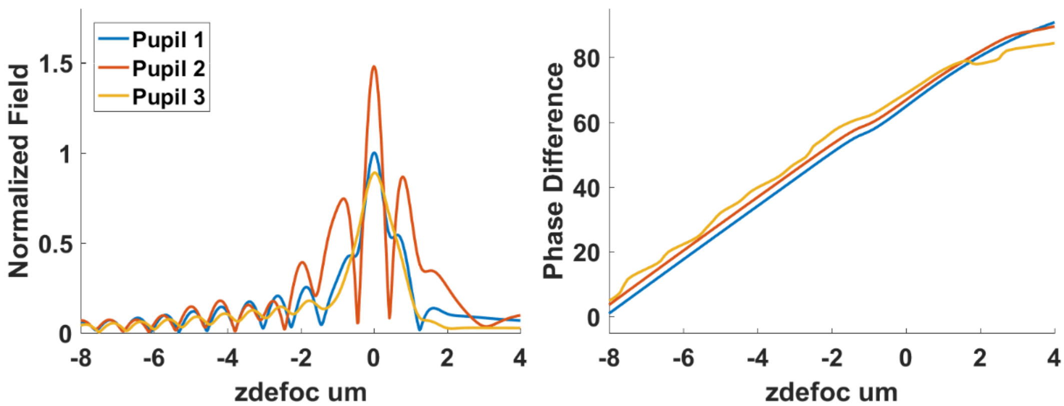

Figure 4-4 V(z) curves and recovered phase difference between SP and Ref signal

In the Figure 4-4, it can be seen that the quality of the V(z) with pupil function 3 is very poor. This is because the content of the reference beam is not purely direct normal reflection from the surface. It contains other low-frequency components. The quality of the recovered gradient with pupil function 2 is quite good. However, the amplitude of the reference beam is not amplified a lot. Also, the fine control on amplitude at each Δz is difficult. In most cases, a constant amplitude of reference beam at each Δz is appropriate for interference measurement.

4.2.2 Modulation 2– Phase modulation on Reference Beam

Thanks to flexibility of the SLM's control, separate control of the SP beam and Ref beam is possible. The simplest way to keep the amplitude constant is not to defocus the reference beam while defocusing the SP beam so that that reference beam signal does not decrease with defocus. This means that a strong reference beam is detected at the pinhole for all defocuses, this achieved with the pupil as shown on Figure 4-5. Here the central region remains flat while the curvature of the outer region corresponding to the excitation of SPR changes to mimic changing defocus values.

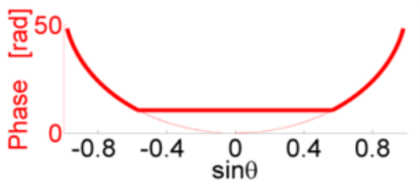

Figure 4-5 shows the phase modulation on BFP

It should be noted that the relationship between the gradient and the excitation can be expressed as

$$\mathrm{grad} = 2\mathrm{nk}(cos\theta_{\mathrm{flat}} - cos\theta_p) \quad (4\text{-}1)$$

where grad is the gradient of the recovered phase difference against defocus distance, θ_{flat} is the phase change of Ref against defocus distance.

Actually, θ_{flat} can be set to zero so that the equation can be rewritten back to the standard relationship which can be expressed as

$$\mathrm{grad} = 2\mathrm{nk}(1 - cos\theta_p) \quad (4\text{-}2)$$

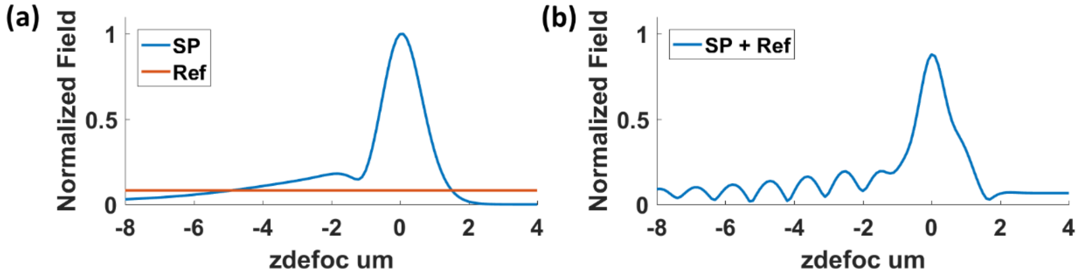

Figure 4-6 shows (a) the simulation amplitude of SP and Ref signal with flat phase of $cos\theta_{\text{flat}}$ on reference signal and (b) the interference signal of V(z) curves

In the simulation as shown on Figure 4-6 (a), it is obvious that the amplitude of the reference signal is amplified at least two times and the amplitude now is constant against defocus distance. As shown on Figure 4-6 (b), the ripples become bigger and the period of the ripples changed from 0.69 to 0.96 micron as they are inverse proportional to the factor $\left(\cos\theta_{\text{flat}} - \cos\theta_p\right)$. The details will be discussed in the latter context.

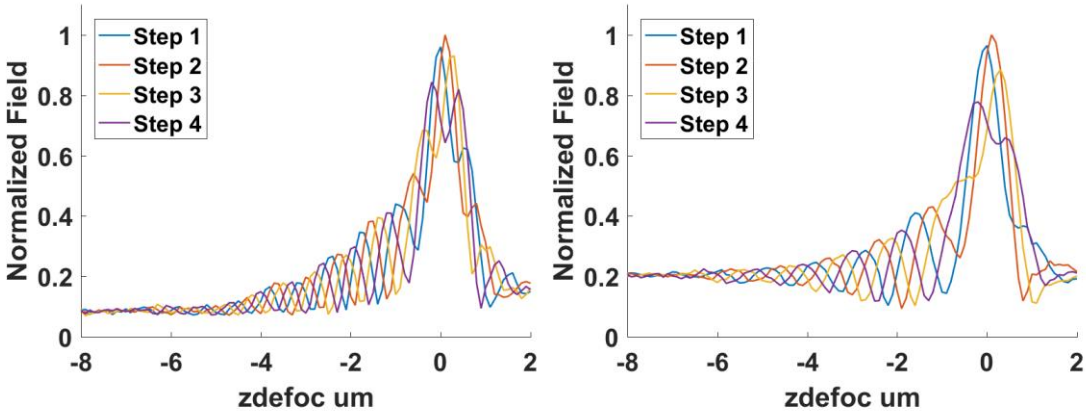

Figure 4-7 shows the one of the experimental phase-stepping results (a) without flat phase and (b) with flat phase on ITO layer with nominal thickness of 6 nm.

To test the performance, we performed an experiment on the SPRM as describe on the section 3.3 in Chapter 3. The amplitude pupil function is standard reference beam as shown on Figure 4-2b. The output with flat phase (as shown on Figure 4-5) and without flat phase were measured as shown on Figure 4-7. It is clear that the reference beam signal was amplified. It can survive in longer defocus distance. By repeating the experiment 50 times, the values of the standard deviation of the recovered thickness were calculated. Without flat phase modulation, it was 0.37 nm. With flat phase modulation, it is 0.16 nm only. It strongly shows that the signal to noise ratio is improved when the flat phase is modulated on the reference beam. It can be easily explained by the fact that the reference beam did not undergo defocusing. It remains stationary at the confocal pinhole.

4.2.3 Modulation 3– Hybrid modulation on Reference Beam

In the previous sub-section, we show the use of the flat phase can help to improve the signal to noise ratio. However, it is not the only advantage of the keeping the reference beam stationary at the confocal pinhole. Thanks to this arrangement, the amplitude of the pupil function for reference beam can be designed in any shape without fearing the nonlinear effect.

Now, two modulation techniques are combined to further enhance the reference signal as shown on Figure 4-8.

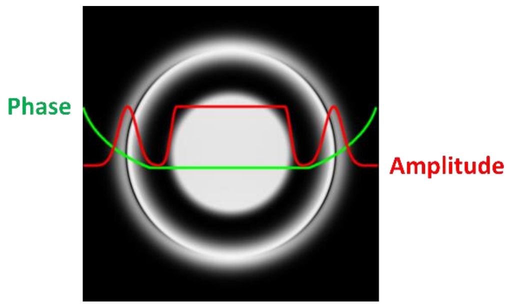

Figure 4-8 shows the schematic diagram of amplitude and phase modulation

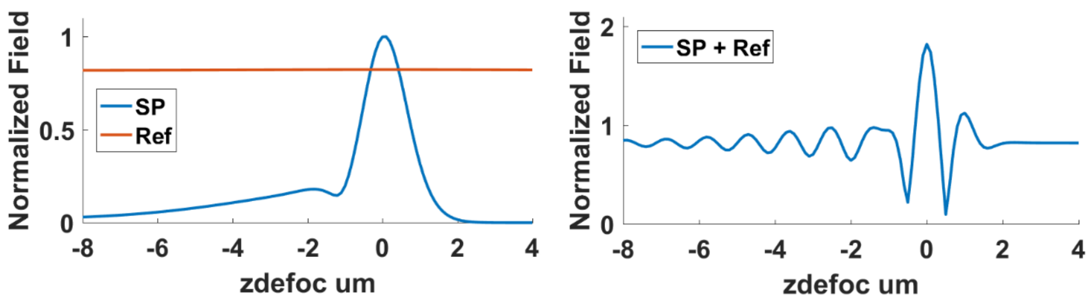

Figure 4-9 shows (a) the simulation amplitude of SP and Ref signal on reference signal and (b) the corresponding interference signal of V(z) curves

It can be seen that the amplitude is amplified substantially which is greater than that of defocused SP signal resulting in reference beam (see Figure 4-9 (a)).

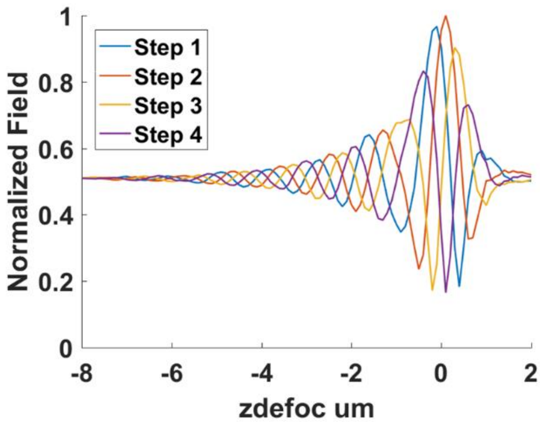

Figure 4-10 shows that experimental result on hybrid modulation on ITO layer with nominal thickness of 6 nm.

As shown on Figure 4-10, the result is very promising, and it should be noted that the result is the actual experimental data. Again, by repeating the experiment 50 times, the standard deviation of the recovered thickness without flat phase is 0.07 nm. The result is 5 times better than the thickness recovered by a simple defocus approach (which is 0.37 nm from the previous section).

4.2.4 Measurement in Low Power Environment

To demonstrate the performance of the controllable reference beam technique, we reduce the power to examine the performance of the unwrapped phase of SP against defocus with very low input light power. In the experiment, we reduced the input power by changing different AR-coated neutral density filters. Then, the unwrapped phases against defocus were measured with a standard measurement and the controllable reference beam technique.

In this experiment, the optical system is the same as described in the methodology. The input light power to the system is reduced by changing the neutral density filters. It shows the gradient with flatcap defocus implementation can survive when there is low light power environment.

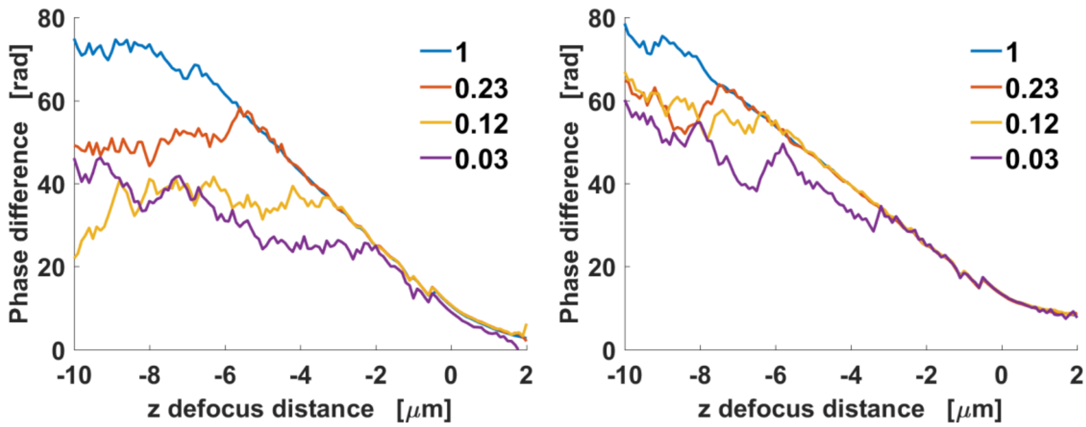

Figure 4-11 shows the recovered gradient (a) without flatcap modulation and (b) with flatcap modulation in low input light power, 766 nW, 178 nW, 87 nW and 22 nW respectively

The results in Figure 4-11 show that the linear regions on controllable reference beam measurement are much longer than that of standard measurement. This means that k-vector can be recovered with much lower input power ensuring that the signal is much more resilient to noise. From the above analysis, it is shown that the signal to noise ratio can be significantly improved by hybrid modulation method. And it should be noted that the control on amplitude pupil function on reference beam is very easy. It proved that the linearity of the gradient will not be affected with any shape of the amplitude pupil function as long as the phase on the region is flat. Therefore, the region of the reference beam now is not limited to the center. One of the possible regions can be close to SP signal so that the optical path is closer resulting better immunity to noise.

At this modulation flexibility offers another modulation technique, called vortex modulation, which will be discussed in the next section.

4.3 Optical Vortex Modulation

In the previous section, it was demonstrated that separate modulation of SP signal and reference signal allows us to improve the signal-to-noise ratio. In this section, we make use of the technique and apply the concept to speed up the acquisition process by 3 or 4 times depending the number of the measurements for the phase recovery. As mentioned in the earlier chapter, for the phase-stepping technique, the phase difference between SPR signal and the reference signal is calculated by 4 intensities of the detected confocal signal for the SRRM. These 4 intensities signals are measured by offsetting the phase of one of the signals (either SPR signal or Ref signal) by 0, 90, 180 and 270 degrees. In this case the calculation of the phase difference between two signals requires 4 measurements for each defocus distance.

We are looking for a technique to directly determine the phase difference between these two signals in a single shot at each defocus distance. In this chapter, we will explain the background of vortex beam first. Then, we will examine the image formed by the vortex beam to work out the parameters with this vortex modulation technique. Finally, the experimental results will be discussed.

4.3.1 Background of optical vortex

The SLM-based SPRM allows a variety of modulation strategies to improve the system. Thanks to the technique developed in the previous chapter, the phase of the reference beam can be modulated in a static phase pattern such as helical distribution. With this pattern, a vortex beam will be projected on the image plane where the phase also has a helical shape allowing us to capture 4 detected signals with the 4 phase differences in a single shot.

The phase has a circular flow around such singular points (called phase singularities) at the center (see Figure 4-12), and such a point is generally referred to as an optical vortex. (Curtis & Grier, 2003). For a vortex beam, it can be generated by a helical wavefront on the back focal plane around its axis of travel. (Curtis & Grier, 2003)

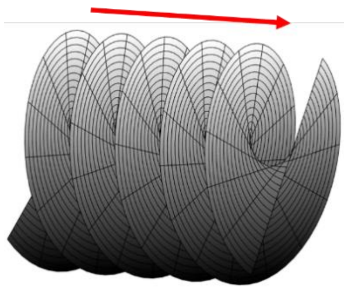

Figure 4-12 Shows the propagation of a helical beam

The topological charge is a number to indicate how many complete rotations of the twisted light occur within one wavelength. In this study, the topological is set to 1.

4.3.2 Helical Beam Projection on Image plane

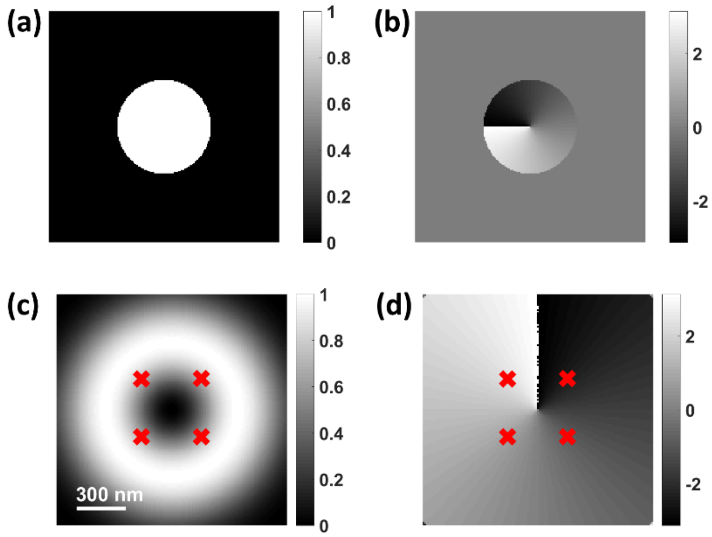

Figure 4-13 (a) and (b) shows the amplitude and helical phase distribution on BFP respectively where $k_x/nk_0 = 0.4$. (c) and (d) show intensity and the phase of the BFP projection on image plane respectively.

It is interesting that the amplitude of the field on image plane is a donut shape. This is because the amplitude at the center is cancelled out by the vortex beam where the phases vary from 0 to 2π. Moreover, importantly, Figure 4-13 (d) shows that the phase distribution of the vortex beam on the image plane is a helical distribution as well which allows us to make use of this phase distribution to reduce the acquisition time by performing phase-stepping on spatial space in single shot. By picking 4 points around the center as shown Figure 4-13 (d), it allows us to perform phase-stepping in single shot for each defocus distance. These four positions were selected based on a few considerations. In order to have equal optical path of the surface plasmon. The selected position should have same distance from the center. In order words, they should be selected within the circle with same radius. Also, the radius should be selected where the strength of the surface plasmon and the reference signal are comparable.

For the azimuthal angle, for phase stepping algorithm, the selected phases should be separated evenly. For this reason, the detection positions were evenly spaced 90 degrees apart. Since the input polarization was horizontally linearly polarized, there is no SP at the vertical position, so it is not possible to use the position at angles of 0, 90, 180 and 270 degrees. Therefore, the positions at the angle of 45, 135, 225, 315 degree were selected and these positions, in principle, can give equal strength to the detected SP signal. The size of the confocal pinhole should be as small as possible while still retaining good signal-to-noise ratio of the detected signal. In general, a smaller pinhole size will give better confocality and it will give better linearity of the recovered phase.

4.3.3 Size of the Vortex Beam

In the next section, we will show that the power of the of vortex should be concentrated at the center for better signal to noise ratio. In this section, I will show how the size of the donut ring on image plane can be controlled by the size of the helical beam on BFP as shown on Figure 4-13 (c).

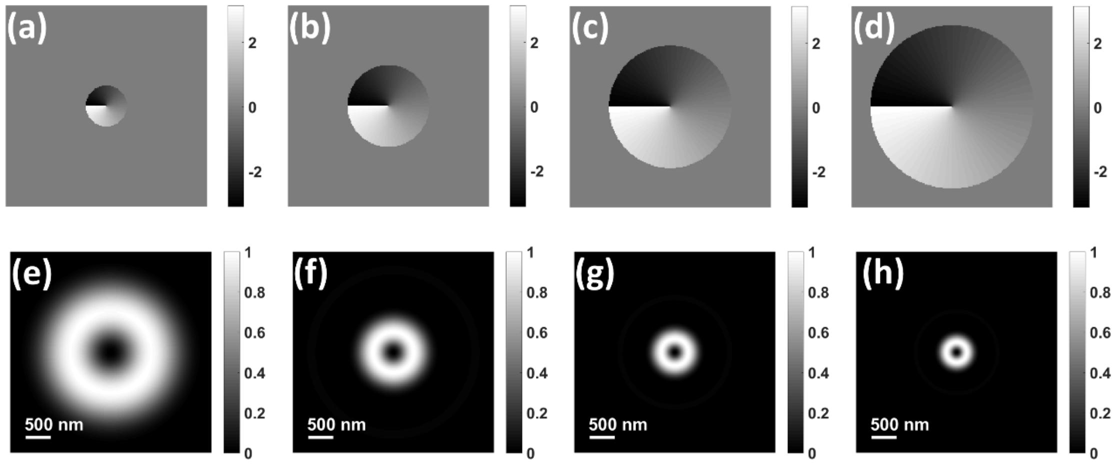

Figure 4-14 (a-d) show the size of helical beam of $k_x/nk_0 =$ 0.2, 0.4, 0.6 and 0.8 on the BFP respectively. (e-h) show the simulated intensity of the projection of the corresponding helical beam on the image plane.

As shown on Figure 4-14, the intensities on the vortex beam are more concentrated at the center when the size of the helical beam on the BFP increases. Therefore, the optimal choice is to choose the vortex beam as large as possible without unwanted interference on the image plane due to edge effect of pupil function.

4.3.4 SPR Projection on Image plane

In this study, instead of using radial polarized light, linear polarized light is adopted for the experiment as the optical configuration for linear polarized light is simpler. This is because radial polarized light normally is converted from linear polarized light by Radial-Polarization converter. The overall system will become much complicated and the alignment of radial-polarization converter is not a simple task. Therefore, linear polarized light is used for the demonstration of the idea of the vortex reference beam measurement.

However, it should be noted that SP can only be excited by p-polarization. With linear polarization illumination, the reflected light is the combination of the p-polarization and s-polarization resulting unsymmetrical distribution on azimuthal direction. Therefore, it is worth to investigate the complex field distribution on image plane.

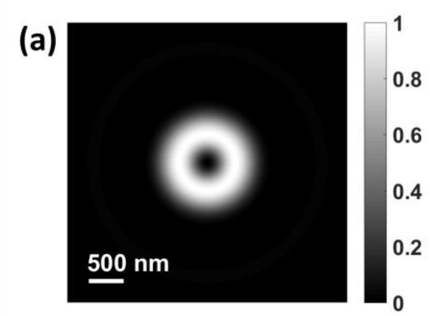

Figure 4-15 shows intensity of (a) Vortex Reference Signal and (b) SPR signal on image plane at defocus distance of -3 microns

Figure 4-15 shows the intensity of vortex reference beam and SPR beam on image plane at defocus distance of -3 microns. It can be seen that the intensity of the SPR signal near the central point is more uniform. Therefore, the reasonable choice of the 4-points measurements should be obtained near this region. On the other hand, to obtain proper interference signal of reference beam and SP beam, the amplitude between two signals should be comparable. Therefore, the choice of the confocal point should be chosen based on the strength and the smoothness of the signal.

In conclusion, we demonstrate that phase difference between SPR signal and Reference signal can be obtained in single shot. The experimental result will be analyzed in the next section.

4.3.5 Simulation Result on V(z) measurement

In the previous sections, I addressed the choice of values of the parameters such as the size of the helical beam on the BFP and the position of confocal pinhole on the image plane. In this simulation, the positions of the confocal pinhole are chosen at

50 nm from the central point at 4 different azimuthal angles of 45˚, 135˚, 225˚ and 315˚.

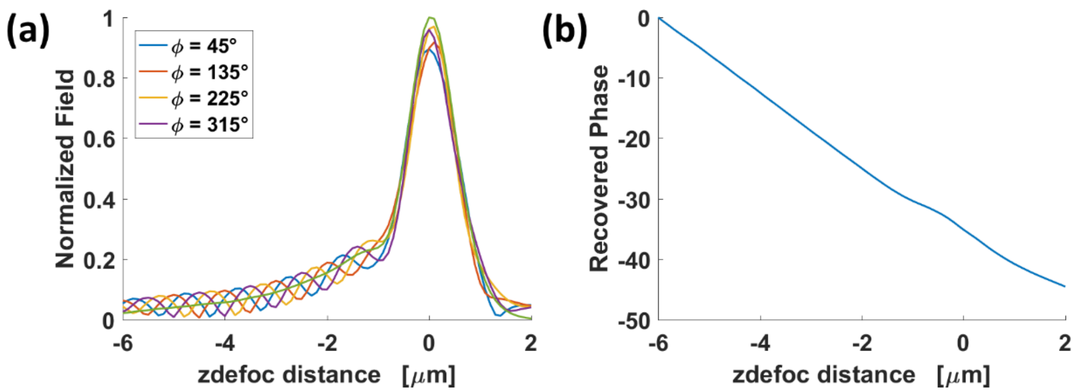

Figure 4-16 shows (a) the simulated V(z) from 4 points where each confocal point was on 50 nm from the central region at different azimuthal angles of 45˚, 135˚, 225˚ and 315˚ and (b) the recovered gradient based on 4 intensity measurements.

The simulated V(z) on Figure 4-16 shows that the relative phase against defocus distance can be recovered by the measurement in 4 different confocal positions in a single shot. Then, the excitation angle can be recovered by according to the equation (4-1).

4.4 Experiment and Results using Optical Vortex Modulation

In the previous section, we showed that vortex reference beam allows us to capture 4 different phase steps in one-shot. In this section, we are going to test the performance of this vortex technique in practical situation. The recovered result will compare with the result recovered by standard phase-stepping measurement. The practical consideration will also be discussed.

4.4.1 Experimental Setup

As mentioned a lot in this study, the integration of SLM in the embedded confocal SPRM enables us to control a variety of operations in the measurement. Without additional modification on the optical configuration described on Figure 3-7, the vortex beam can be generated with the SLM. The only difference is the modulated reference beam now a vortex beam instead of direct normal reflection.

4.4.2 Sample Preparation

Figure 4-17 shows schematic structure of test sample

In the experiment, a test sample with layers of different thicknesses of Indium Tin Oxide (ITO) is used for demonstration of measurement of the plasmonic dip movement (see Figure 4-17). A gold layer with thickness of 45 nm was first sputtered on a coverslip followed by multiple ITO layers onto the gold layer. Each ITO layer was roughly 5nm. Then, the ITO thickness is measured by using a surface profiler (model: P10 from KLA Tencor) to measure the ITO thickness and an ellipsometer (model: M-2000 from J.A. Woollam Co) to measure the refractive index of the ITO.

4.4.3 Result and Analysis

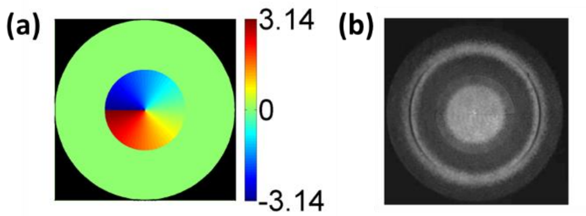

Figure 4-18 (a) show the vortex phase imposed on the pupil function and (b) experimental distribution on the BFP with SP excitation.

In this experiment, we impose the phase and the amplitude pupil function on the BFP as shown on Figure 4-18. By measuring the confocal signal from the center of 47 nm at different azimuthal angle of 45˚, 135˚, 225˚ and 315˚, we obtained the V(z) curves at shown on Figure 4-19.

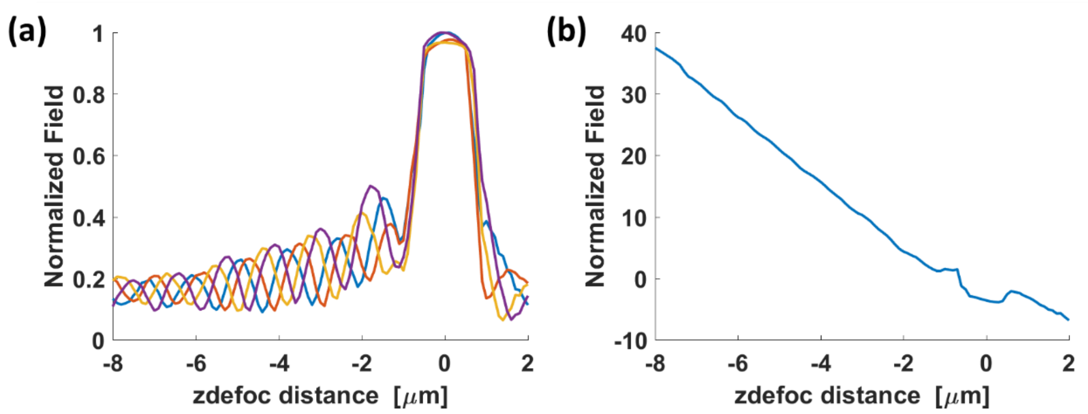

Figure 4-19 shows the experimental result on 4-point measurement on bare gold sample. (a) Vz curves and (b) the relative phase

It shows that the amplitude of the field on V(z) is slightly irregular resulting an unwanted ripple on the recovered gradient. This may arise from the non-uniform illumination on different positions on the xy plane. The reason why we cannot observe this effect on the standard phase stepping measurement is because the confocal signal collected at center is the contributions from all azimuthal angles. To suppress the ripple, least squares method is applied to estimate the gradient of vortex measurement which will be described in the latter context.

4.4.4 Algorithm for arbitrary Phase stepping

As the illumination on the BFP may not be perfect resulting in non-uniform illumination, the projected field on the image plane may not be perfect as well leading to a phase shift on the image plane. In order words, the effective reference phase γ is the function of azimuthal angle α such that $\gamma(\alpha)$.

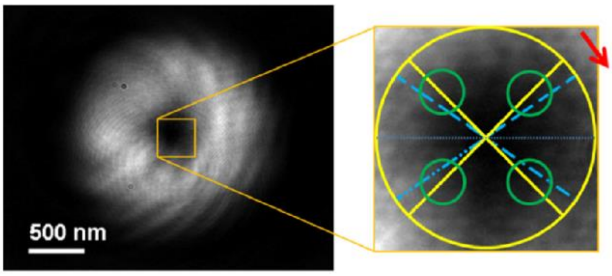

Figure 4-20 shows the position of the confocal pinholes

It should be noted that the effective reference phases are determined are not precisely separated by 90 degrees. A good estimate of the effective phases, however, can be made by examining the individual V(z) curves at each position and measuring the phase difference between the ripple patterns. In order to ensure the confocal pinholes are correctly placed, the effective phases should be exhibit proper symmetry. The effective phases should be δ_0, $\pi - \delta_0$, $\pi + \delta_0$ and $2\pi - \delta_0$ as shown on Figure 4-20. The phase value can then be inserted into a generalized phase reconstruction algorithm proposed by Lai and Yatagai (Lai & Yatagai, 1991). Then, the relative phase against defocus distance can be recovered. The output intensity can be expressed as

$$I(\alpha) = |A|^2 + |B|^2 + 2|A||B|\cos[\emptyset + \gamma(\alpha)] \tag{4-3}$$

which can be written in

$$I(\alpha) = I_0\{1 + \beta\cos[\emptyset + \gamma(\alpha)]\} \tag{4-4}$$

Where $I_0 = |A|^2 + |B|^2$, $\beta = 2|A||B|/I_0$, $\emptyset$ is the relative phase between the SP signal and reference signal, α is the azimuthal position, $\gamma(\alpha)$ is the effective phase of the reference beam. In this form, we can apply the generalized phase reconstruction algorithm to recover the corrected relative phase against defocus distance. By least squares fitting the gradient within the window of good linearity, the value of excitation angle is obtained.

Table 1 Comparison of ITO measurements by surface profiler, BFP, vortex and phase-stepping technique.

	Surface Profiler	BFP		Vortex		Phase Step	
	t [nm]	θ°	recovered t [nm]	θ°	recovered t [nm]	θ°	recovered t [nm]
Bare Au	0	44.06	-	44.06	-	44.06	-
Layer 1	5.7	45.86	7.42	45.38	5.72	45.31	5.46
Layer 2	9.6	46.95	10.70	46.62	9.77	46.59	9.67
Layer 3	14.3	48.94	15.37	48.62	14.70	48.37	14.16

t: thickness

Table 1 shows the recovered ITO thickness by the methods such as surface profiler, the dip on BFP, vortex measurement and phase-stepping measurement. It can be seen that the recovered thicknesses by vortex measurement has very good agreement with that by phase-stepping measurement. As expected, the dip position measurement on BFP is also reasonably close.

In short, we conclude that the idea of using vortex beam as a reference beam for interferometry was validated although we may need post-processing technique to determine the center of the vortex.

4.5 Hilbert-Transform based Surface plasmon microscopy

Recently, we investigated another approach called Hilbert-Transform Surface plasmon microscopy (Chow, Zhang, & Somekh, 2018) to speed up the data acquisition. As this thesis focuses on advanced phase techniques to improve the speed of the data acquisition, I will give a brief introduction of this technique of Hilbert Transform. (for the details, please refer to the recent published paper or (Bracewell, 1978)).

4.5.1 Hilbert Transform

Hilbert Transform of a signal $s(x)$ can be expressed as (Bracewell, 1978)

$$\mathcal{H}s(x) = \frac{1}{\pi}\int_{-\infty}^{\infty}\frac{s(x')}{x'-x}dx' \tag{4-5}$$

which can be regarded as the convolution of $s(x)$ and $1/\pi x$. For a real function $s(t)$, we can transform the function into analytic signal $s_a(t)$ which can be expressed as

$$s_a(t) = s(t) + i\mathcal{H}s(t) \tag{4-6}$$

When $s(t) = \cos(\omega t)$, $s_a(t) = \exp(i\omega t)$ as $\mathcal{H}s(t) = \sin(\omega t)$.

It is the property of the Hilbert Transform to convert the signal to the analytical signal that proves so used useful in our processing of the V(z) signal.

4.5.2 Experiments and Results

In this section, the detail of how the phase between two signals can be extracted from a V(z) curve by Hilbert Transform. Recall that the detected signal $|V(z)|^2$ can be expressed as

$$|V(z)|^2 = |R(z)|^2 + |S(z)|^2 + 2|R(z)||S(z)|\cos\left(\frac{4\pi n}{\lambda}\left[1-\cos\theta_p\right]z+\alpha\right)$$

Where $R(z)$ and $S(z)$ are the reference and SP signal. α is a constant offset related the pupil function of the microscope objective. By subtracting the background $|R(z)|^2 + |S(z)|^2$, we have

$$2|R(z)||S(z)|\cos\left(\frac{4\pi n}{\lambda}\left[1-\cos\theta_p\right]z+\alpha\right) \tag{4-7}$$

Then, we can apply the Hilbert transform to obtain the analytical expression ($s_a(z) = s(z) + i\mathcal{H}s(z)$). For single dominant frequency like equation (4-7), the analytical expression of equation (4-7) becomes

$$2|R(z)||S(z)|\exp i\left(\frac{4\pi n}{\lambda}\left[1-\cos\theta_p\right]z+\alpha\right) \tag{4-8}$$

As a result, the relative phase between reference and SP signal can be easily obtained. We believe that the Hilbert transform method is an effective method to process the interference signal. As no phase stepping is required, the complexity of the system will also be greatly simplified.

In the experiment, the optical system remains unchanged. Standard phase-stepping measurement on SPRM was conducted on 4 gold samples used in the previous section. Then, we have 4 V(z) curves with 4 phase steps for each sample which can be shown on Figure 4-21.

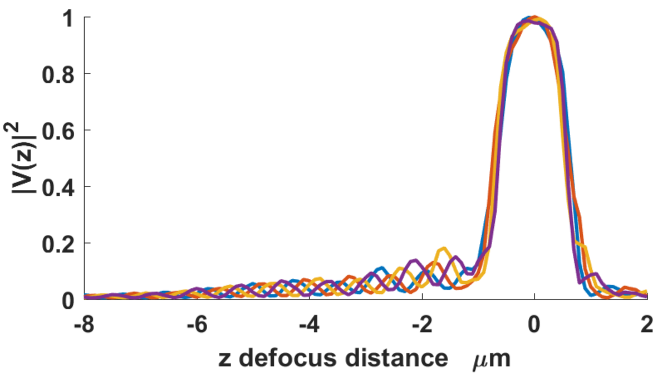

Figure 4-21 shows $|V(z)|^2$ with phase steps

For each sample, the relative phase Ø against defocus distance between two signals can be recovered according to the equation (2-14). Also, the relative phase Ø against defocus can be directly recovered by Hilbert Transform method as discussed above. Then, the excitation angle θ_p can be recovered by the equation (2-17). Finally, the values of the θ_p were converted to the thickness for comparison.

Table 2 Summary of the experimental results of the Phase Stepping and Hilbert Transform

Layer	Thickness t (nm)							
	SP	PS	HT				mean(t)	std(t)
0	-	-	-	-	-	-	-	-
1	5.7	5.98	6.94	6.10	5.12	6.06	6.05	0.74
2	9.6	10.73	10.88	11.46	10.78	10.72	10.96	0.34
3	14.3	14.05	14.26	15.32	13.87	13.16	14.15	0.90

SP: Surface Profiler, PS: Phase-Stepping, HT: Hilbert Transform

It can be seen on Table 2 that the recovered thickness by the Hilbert Transform is comparable with that of phase-stepping approach. They show good agreement with the result measured from the surface profiler.

It should be noted that phase stepping approach relies on the accurate and consistent phase steps. Therefore, the errors in the phase steps may introduce systematic errors to the curves of the relative phase against defocus distance for the choice of window. For Hilbert transform, the relative phases are recovered without the need of the accurate phase step. Also, the cost of the system can be greatly removed by not using SLM. Therefore, it is more flexible and reliable approach to recover the excitation angle in SPRM.

4.6 Summary

In this chapter, we demonstrated different advanced modulation techniques to improve the performance of the SLM-based SPRM. With the separated control of the reference beam, it allows us to enhance the reference beam by keeping the reference stationary at confocal pinhole. The experimental result showed that the interference signal can survive even in a low power environment. On the other hand, we demonstrated that the acquisition time can be improved by imposing optical vortex beam so that the relative phase between reference and SP signal can be extract in a single shot. Additionally, we showed that Hilbert can also be used to reduce the time of data acquisition. Therefore, the goals of improving the signal to noise ratio and the time for data acquisition were achieved by the advanced phase modulation technique by integrating the SLM into the SPRM.

It is, of course, possible to combine the vortex approach with the Hilbert transform method. In principle, we can obtain individual V(z) curve at different azimuthal positions from the vortex distribution. Therefore, by combining the technique of the Hilbert Transform, we could extract the phase against defocus distance for each individual V(z) curve. And therefore, the signal-to-noise ratio can be improved by averaging over the many positions. This would have the advantage over conventional phase stepping that it is not necessary to know the relative phase between signal and reference beam at each position. It remains a matter for further study to determine whether this would have benefits over the Hilbert transform as presented in this chapter.

Chapter 5 – Separation of Attenuation mechanisms by Goos–Hänchen Phase Engineering

In the previous chapter, we demonstrated that the excitation k-vector can be obtained by locating the dip position on the BFP or measuring the gradient of phase change against defocus distance from the V(z) curves.

Recently, researchers are interested in designing different optical devices such as SP sensors, waveguide sensors (Berini & De Leon, 2011) and so on. The attenuation coefficient is an important parameter to characterize those surface-wave sensors.

As the SP will propagate along the surface when it is excited, the lateral resolution can be improved by reducing the propagation length of the SP. One of the ways of reducing the propagation length of SP is to introduce more loss with different materials as discussed in Chapter 2. However, this is not the only way to introduce the loss term of the SP. Another approach to reduce the propagation length of SP is to design a coupling structure with high coupling loss. Therefore, the SP will attenuate quickly when it propagates along the interface. Therefore, insight into the loss mechanism can help to optimize the sensitivity and the resolution of the SPRM. In this chapter we consider two dominant loss mechanisms of SP, (i) the ohmic loss in the metal where the energy is converted to heat and (ii) the coupling loss where the decay of the SP arises from reradiation of energy back into the couplant. The key point in this chapter is developing an experimental method to separate the two loss mechanisms, which to our knowledge has not been done before.

On the other hand, the sensitivity is related to how light is coupled onto the interface. Sensitive SPRM is an attractive approach to measure weak solutions and partial binding over a surface. The attenuation of the SPR is to one of the key parameters in designing such sensors. However, measuring the attenuation of a surface wave is not a simple task. One of the methods of measuring attenuation coefficients is by near-field measurement such as scanning near-field optical microscope (SNOM). (Dawson, Puygranier, & Goudonnet, 2001) but, the operation of SNOM is challenging which involves a scanning tip which is very difficult to align in the optical setup and the scanning tip can easily damage the sample. In contrast to near-field methods, far-field measurement allows simpler preparation and direct measurement which can be used for characterizing and designing the sensors.

In this chapter we will discuss the model for the attenuation of SPs first. Then, we will discuss the limitation of the intensity-based measurement for separating the loss mechanism of SP. The dip in the reflection spectrum may look the similar for different values of coupling loss and absorption loss. It is relatively straightforward to measure the total attenuation but separating different loss mechanisms is more challenging. We will then discuss the experimental method to measure the attenuation of the SP in the SPRM. We will then discuss our novel phase modulation strategy on SPRM to separate the two loss mechanisms. The calculation to separate loss will be discussed later in this chapter. Finally, the experimental results will also be presented.

5.1 Background

When the SP is excited, the field at the interface will be enhanced resulting in a large energy absorption on the metallic layer. As mentioned before, a dip can be observed on the reflection spectrum by illuminating the sample with a range of angles. It is noted when the SP is excited, not only energy will be absorbed in a metallic layer to form a dip, it will undergo a phase shift resulting in GH lateral shift representing the movement of energy.

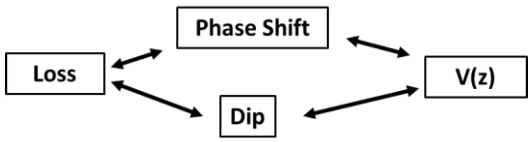

Figure 5-1 Conceptual Relationship between the loss and V(z)

In short, the relationship between these parameters are summarized as shown on Figure 5-1. The loss term on metal surface leads to a dip in the reflection coefficient close to the angle for excitation of SPs, the sharpness of the dip is related to the attenuation of the wave. The phase variation, however, gives more direct information of the attenuation as discussed below. This is the basis of the technique described below, where the SLM is used to produce a phase shift corresponding to a known 'virtual or artificial' surface wave which can be used to calibrate the microscope.

5.1.1 Simplified Green's function

A simplified Green's function is one of the models explaining the relationship between the amplitude and phase of SP. It can be used to explain why the loss mechanism cannot be measured from solely the intensity measurement and the plasmonic dip. Identical plasmonic dips may behave differently for different loss mechanism. With simplified Green's function, no complicated mathematics is involved. The field can be expressed as

$$R(k_x) = u_r + u_{sp} = -1 + 2k_c r(k_x, k_{sp}) \tag{5-1}$$

$$r(k_x, k_{sp}) = \frac{i}{k_{sp} - k_x} + \frac{i}{k_{sp} + k_x} \tag{5-2}$$

Where $k_{sp} = k'_{sp} + ik''_{sp}$, $R(k_x)$ is the reflection coefficient which the sum of two contributions, namely, direction reflection and the reflection due to the excitation of SP reflection on the metallic surface. The direct reflection u_r is assumed to be -1 for simplicity. From the equations, it shows that the resonance condition when $k_x = k'_{sp}$ which means that the phase velocity of SP is matched. Also, k''_{sp} is the total attenuation of SP which consists of two loss mechanism such that $k''_{sp} = k''_c + k''_{ohm}$ where k''_c is coupling loss and k''_{ohm} is ohmic loss.

Considering the case that $k'_{sp} = k_0 \sin\theta_p$ where θ_p is the excitation angle. With different ratios of coupling loss and ohmic loss, the reflection against input k-vector is plotted on Figure 5-2

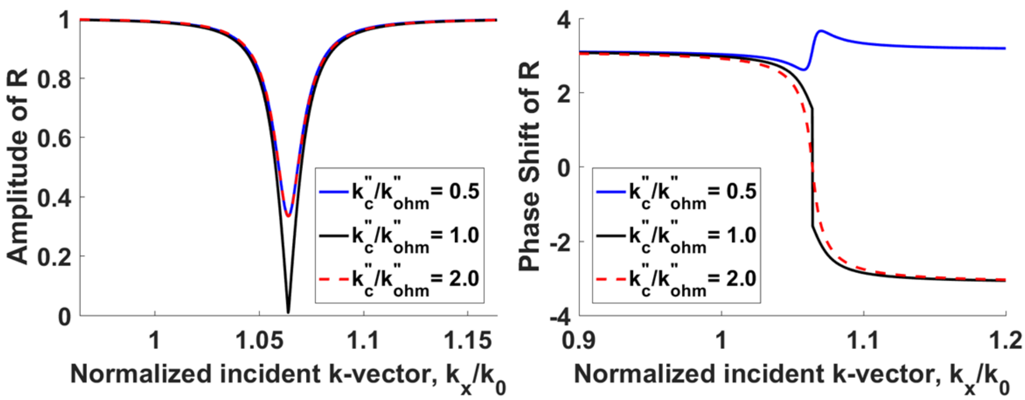

Figure 5-2 shows (a) amplitude of reflection and (b) Goos–Hänchen phase for the case of $k^{"}_c/k^{"}_{ohm} = 0.5$, $k^{"}_c/k^{"}_{ohm} = 1.0$ and $k^{"}_c/k^{"}_{ohm} = 2.0$

The simulated reflection shows that strongest dip occurs when $k^{"}_c = k^{"}_{ohm}$. But it is more worthy of note to see that for the case $k^{"}_c/k^{"}_{ohm} = 0.5$ and $k^{"}_c/k^{"}_{ohm} = 2.0$ where they exhibit a similar shape of the dip. Therefore, we cannot distinguish these two cases if only amplitude (or intensity) of the reflection spectrum is known.

However, the phase change on these two cases are different. Therefore, the difference of the phase shift allows us to separate the loss mechanism of the coupling loss and the ohmic loss. In the latter context, we will show the loss separation can be done by imposing artificial Goos–Hänchen phase engineering in our modified SPRM. But it should be noted that this technique can be applied on any other surface wave like measurement.

5.1.2 Surface wave measurement at defocus

In this section, we will discuss the principle of detecting surface wave in a confocal system and show how the wave propagation model leads to an expression similar to equation 5.3 provided the defocus values is sufficiently large. As discussed in the previous chapter, the SP will propagate along the surface when it is excited. However, we can make use of this property to separate the surface wave and non-surface wave in the confocal system.

Recently, our group demonstrated that the confocal SPRM can be used for the measurement of total attenuation of SP propagation. (B. Zhang, S. Pechprasarn, & M. G. Somekh, 2013) With the confocal pinhole, only one particular path of re-radiation of SP will be collected as described in the previous chapter 2. (or as shown on Figure 5-3) Therefore, the attenuation of the surface wave can be measured by measuring the confocal signal arising from the re-radiation of the SP.

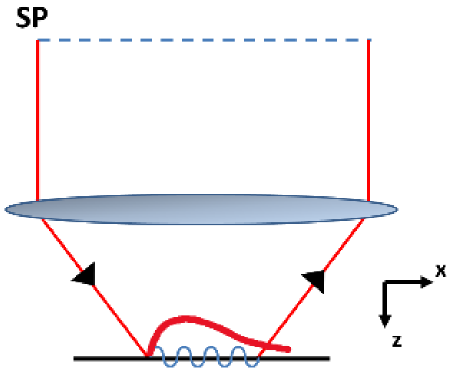

Figure 5-3 shows the measurement of V(x) by defocusing the sample

The collected confocal signal for sufficiently large defocus distance (e.g. beyond 3 microns) can be expressed as

$$|\mathrm{SP}(x)| = A\exp\left(-k_{sp}^{"}x\right) \tag{5-3}$$

where $k_{sp}^{"}$ and A are the total attenuation and modulus of SP respectively. This the validity of this assertion is discussed later in this chapter.

By taking natural log on Eq(5-3), we obtain

$$\ln[|\mathrm{SP}(x)|] = \ln[A] - k_{sp}^{"}x \tag{5-4}$$

By measuring the gradient of the decay, the total attenuation of SP can be recovered. On the other hand, the modulus of SP(x) can be further expressed in terms of coupling loss term k_c'' and ohmic loss term k_{ohm}'' such that

$$|\mathrm{SP}(x)| = 2k_c''\gamma\exp(-(k_c'' + k_{ohm}'')x) \tag{5-5}$$

where γ is an instrument dependent parameter depending on some parameters such as optical power, the pupil function and the size of the confocal pinhole. To separate two attenuation coefficients, we need to know γ. Our approach is to generate an artificial backward surface wave within the same system so that overall γ can be obtained by analyzing the attenuation of the artificial wave. (Appendix I derives the stationary phase approximation for the SPs generated at defocus, which validates equation 5.3.) The detailed discussion of the separation of the two loss mechanisms will be discussed in the latter section.

It is useful at this stage to explain the parameter γ in a little more detail. Essentially the magnitude of the SP signal generated is proportional to k_c'', however, the dimensionless scaling factor γ, is unknown and therefore requires calibration. For instance, there are several factors such as the optical power, the size of the pinhole and the pupil function that determine the precise value of this parameter. It is clear that any direct calibration of this parameter is not practical and would have very large errors. For this reason we devised a way to provide an internal calibration that absorbed all of these factors. This is discussed in detail later in this chapter, the only major assumption that is made is that the pupil function of the lens and optical system does not depend on the azimuthal angle, which is usually the case for a well-designed system.

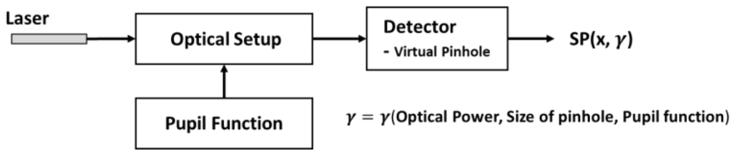

Figure 5-4 show the conceptual relationship between parameter γ and the applied parameters

In short, for a given setup, the instrumental parameter γ is varied by the factors of optical power, the size of the pinhole and the pupil function as shown on Figure 5-4. But the value of the γ will remain unchanged when these applied factors are fixed. Therefore, we can perform the internal calibration by our proposed method.

5.1.3 Relationship between $k_x^{''}$ and $k_z^{''}$

Recall that V(z) curve is obtained by measuring the confocal signal when the sample is defocused. For defocus distance Δz, the SP is propagated along the surface with a distance of $2\Delta x$ as shown on the Figure 5-5.

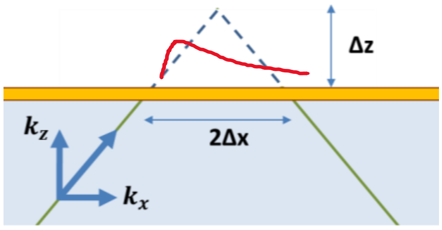

Figure 5-5 shows the propagation of surface plasmon

Therefore, conversion is needed to obtain the propagation distance from V(z) curve. As optical path length = $k_x^{''} 2\Delta x = k_z^{''}\Delta z$, hence, the propagation distance can be calculated by the expression below

$$k_x^{''} = k_z^{''}/(2\tan\theta_{sp}) \tag{5-6}$$

where θ_{sp} is the excitation angle. Once the attenuation of surface plasmon $k_z^{''}$ is calculated, the propagation distance can be computed by $1/k_x^{''}$ correspondingly.

5.2 Attenuation Measurement in Confocal Surface plasmon microscope

The further analysis on the confocal signal in SPRM will be analyzed in this section. As discussed in the previous chapter, the confocal signal is measured at negative defocus distance as shown on Figure 5-6 which is corresponding the case that the sample is moving towards to the objective lens.

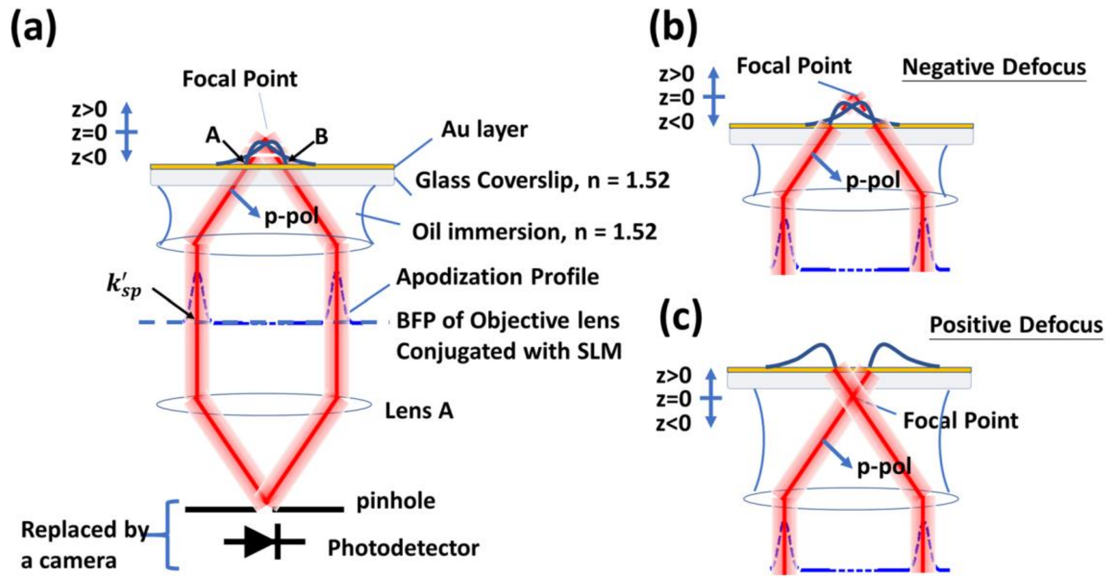

Figure 5-6 shows (a) the schematic diagram of confocal SP microscope, (b) negative defocus and (c) positive defocus (Pechprasarn, Chow, & Somekh, 2018)

The simulated V(z) response (confocal response) $u_r(k_x)$, surface wave $u_{sp}(k_x)$ and the total reflection $R_p(k_x)$ are plotted on Figure 5-7. These V(z) confocal response are simulated from the BFP calculated using Eq(5-1) where $k''_{sp} = 0.018\, k'_{sp}$ and k''_{c}/k''_{ohm} = 1.5, $n \sin\theta_p$ = 1.0570 where θ_p is the angle of SP. In order to measure the response of the SP, the modified amplitude pupil function as shown on Figure 5-7(b) is used to illuminate to the sample. With this amplitude pupil function, only the light around the resonance angle is allowed to illuminate the sample and no reference beam is involved.

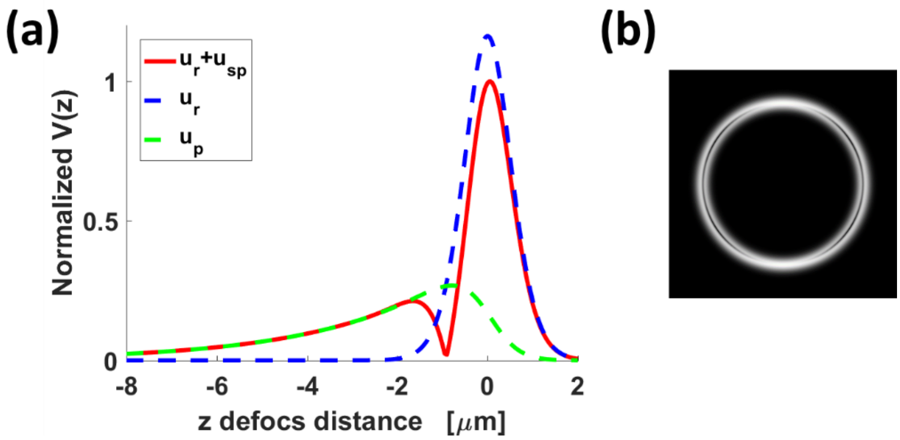

Figure 5-7 shows (a) simulated V(z) for the BFP calculated using Equation (5-1) with $k''_{sp} = 0.018\, k'_{sp}$, k''_c/k''_{ohm} = 1.5, $n \sin\theta_p$ = 1.057, where *n* is the refractive index of immersion oil of 1.52. The red curve is the V(z) curve calculated by for the simplified model BFP using Equation (5-1). The dashed blue curve is the V(z) calculated from the simplified model BFP with the $u_{sp}(k_x)$ = 0 and the dashed green curve is the V(z) curve calculated form the simplified model BFP with $u_r(k_x)$ = 0 and (b) the corresponding pupil function used in the BFP. The simulated V(z)s illustrate that the surface wave and non-surface wave contribution can be measured separately at large defocus distance since the main contribution of non-surface wave is confined close to the focus. For confocal measurement at sufficiently large defocus distance, e.g. -3 micron, the contribution of the direction reflection can be blocked by the confocal pinhole. Consequently, only surface wave signal will be collected. The expression of SP at defocus can be written into a simple form as described by Eq (5-3).

5.2.1 Validation of the simplified model

In order to illustrate the attenuation measurement in the SPRM, V(z) with different attenuation coefficients are simulated.

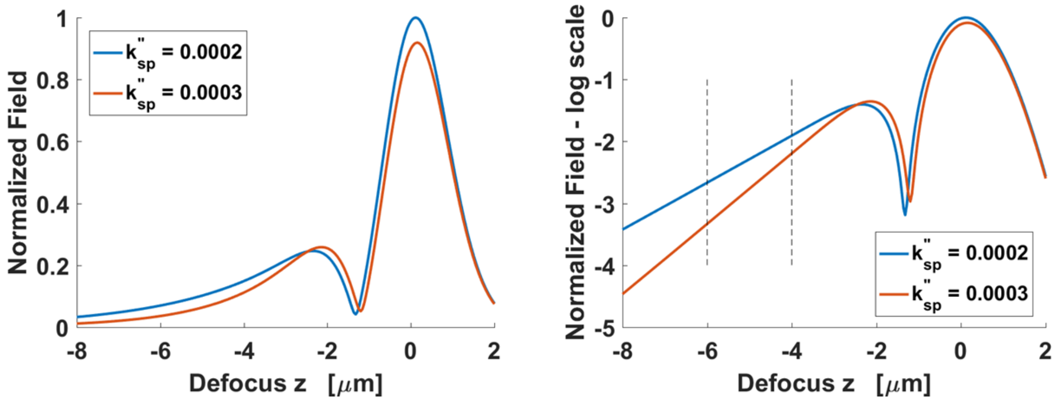

Figure 5-8 shows the (a) simulated V(z) calculated from the BFP with two different $k_{sp}^{"}$ such as 0.0002 and 0.0003, by simplified Green's function and (b) log scale of V(z)

In Figure 5-8, two V(z) are simulated with attenuation coefficient $k_{sp}^{"}$ of 0.0002 and 0.0003. It is clear that with SP will attenuate faster as the attenuation coefficient increase. By measuring the gradient of the decay within proper interval with good linearity, the attenuation coefficient can be recovered as discussed in the previous section. As the prior knowledge of the permittivity of gold layer is not required to work out the attenuation coefficient, the V(z) measurement can be regarded as a model-free method. For instance, previous work such as that of Kretschmann (Kretschmann & Raether, 1968) used an approximate model which were compared with the experimental results to recover the attenuation values, such an approach has intrinsic uncertainties.

Table 3 shows the comparison between input and recovered attenuation coefficients

	k_{sp} $[10^{-4}m^{-1}]$					
Input	2.000	2.200	2.400	2.600	2.800	3.000
Recovered	1.995	2.194	2.394	2.594	2.793	2.993
% error	0.27%	0.25%	0.25%	0.24%	0.24%	0.25%

The result shown on the previous work such as that of Kretschmann (Kretschmann & Raether, 1968) used an approximate model which were compared with the experimental results to recover the attenuation values, such an approach has intrinsic uncertainties.

Table 3 shows good agreement between the input attenuation coefficient and the recovered coefficient. The percentage error for all the cases are below 0.3%. Therefore, it shows that accurate measurement of attenuation coefficient can be obtained by the confocal SPRM.

5.2.2 Attenuation coefficient of a smooth gold sample

The attenuation coefficient of SP on different thickness of gold layer can be estimated from the V(z) measurement.

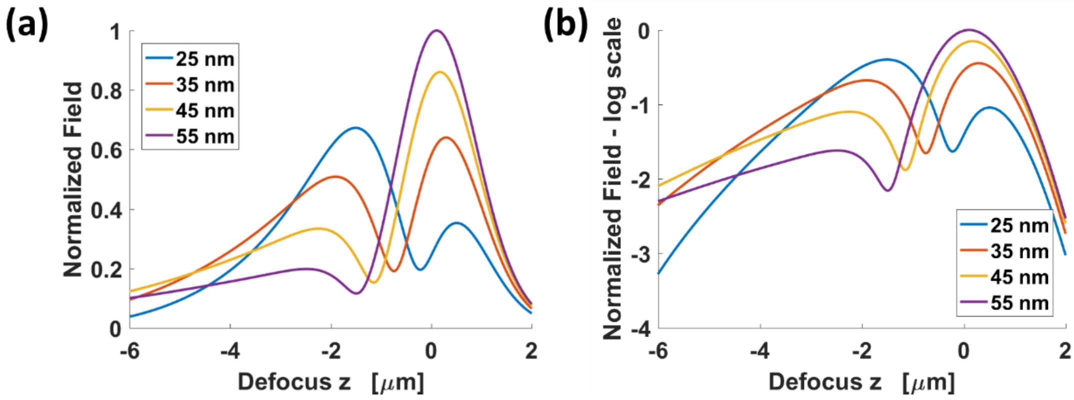

Figure 5-9 shows the (a) simulated V(z) calculated from the BFP of gold layer of different thicknesses and (b) log scale of V(z)

Figure 5-9 shows that the field of the SP of thin gold layer (e.g. 25 nm) is a strong surface wave at around -2 micron and it attenuates quickly compared with the SP on different thickness of gold. It is clear that the attenuation coefficients of SP become smaller as the thickness of gold layer become greater. However, we cannot separate the loss mechanism of ohmic loss and coupling loss. In the next section, a novel approach of separating the loss mechanism in SPRM will be discussed.

5.3 Separation of Loss mechanism

In this section, the novel approach of separating the loss mechanism of SP will be discussed.

5.3.1 Loss Model of Surface plasmon

Recall from the equation (5-5) that the modulus of SP(x) can be expressed in terms of coupling loss term k_c'' and ohmic loss term k_{ohm}'' such that

$$|\mathrm{SP}(x)| = 2k_c''\gamma\exp\left(-\left(k_c'' + k_{ohm}''\right)x\right)$$

where γ is an instrument dependent parameter. k_c'' and k_{ohm}'' are the attenuation coefficients of coupling loss and ohmic loss. By taking the natural log on the equation (5-5), it becomes

$$\ln(|\mathrm{SP}(x)|) = \ln\left(2k_c''\right) + \ln(\gamma) - \left(k_c'' + k_{ohm}''\right)x \tag{5-7}$$

The situation is now that the total attenuation can be easily measured from the gradient of the log of the V(z) response as discussed in the previous section, to separate the two loss mechanisms it is necessary to obtain the y-intercept of this line in Eq. 5.7. The value of this intercept, however, depends not only on the coupling loss but also on the instrumental parameter γ of the optical systems such as the pupil function and illumination power. As mentioned earlier direct calibration of this value is highly challenging for this reason we use the SLM to perform an internal calibration that allows the instrumental parameters to be easily removed.

5.3.2 Goos–Hänchen phase shift engineering

In order to recover the instrumental parameter γ as mentioned in the previous section, an artificial phase for the s-polarization will be imposed on the BFP by the phase-SLM to generate an artificial surface wave which is shown on Figure 5-10.

The phase profile imposed by SLM is expressed as

$$\emptyset_{artificial}(k_x) = 2\tan^{-1}\left(a\left(k_x + k_p\right)\right) + \pi \qquad (5\text{-}8)$$

where $\emptyset_{artificial}$ is artificial phase imposed by SLM, a and k_p are the variables used to determine the gradient of the phase shift and the mean position of the phase shift respectively. The parameter 'a' is used to control the propagation of the surface wave. It should be noted that the arctan phase function is not the only phase function to give the surface wave propagation on the sample. The reason for using the arctan phase function is simply that it can give good representation of a real phase variation with a very simple function. Near the wave vector k'_{sp} along the direction corresponding to s-polarization the phase almost constant so all the phase shift imposed by the SLM contributes to the phase profile of the artificial surface wave. Moreover, the amplitude is nearly constant so there is effectively no dip in the reflection coefficient, so the wave simulated by the SLM corresponds to a wave with no ohmic loss, with all the loss contributed by coupling loss.

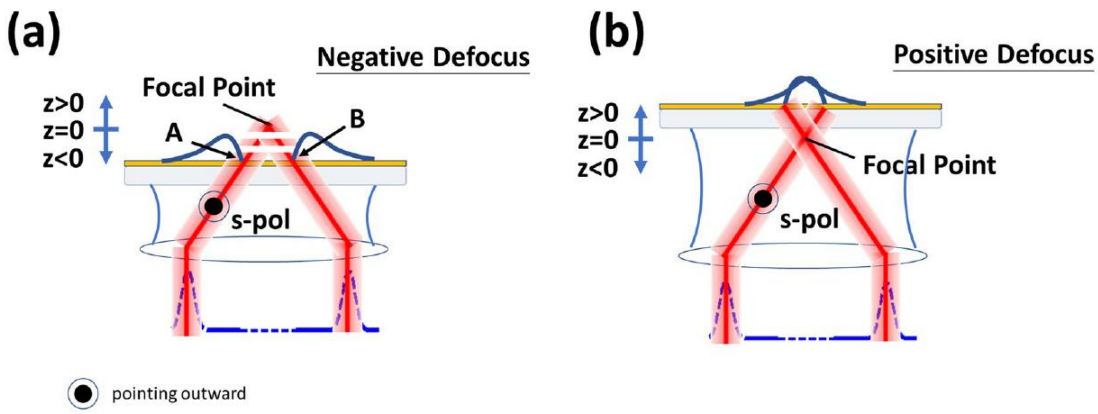

Figure 5-10 shows (a) negative defocus where the s-polarization artificial surface wave propagates away from the optical axis and (b) positive defocus where the s-polarization artificial surface wave propagates towards the optical axis

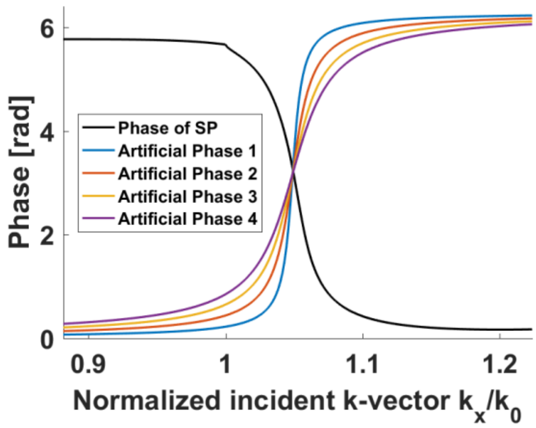

Figure 5-11 shows the phase of SP and the artificial phase calculated by Equation (5-8) where the parameters ((a, k_p) for the artificial phases 1 to 4 are (19e3,0.0104), (9.5e3,0.0104), (6.3e3,0.0104) and (4.7e3,0.0104) respectively

With artificial Goos–Hänchen phase shift $-d\emptyset/dk_y$, the artificial surface wave will propagate backwards as shown in Figure 5-10 and we see in Figure 5-11 that the phase variation with k-vector is opposite to the usual surface wave because of the negative sign of the group velocity. This accounts for the backwards propagating group velocity and the strong excitation at positive defocus. Since the phase distribution is imposed entirely by the SLM we can use the region close to s-polarization to excite the artificial wave. By imposing different phase gradients controlled by the parameter *a* in equation 5-11 we can control the attenuation in a known way, since there is no ohmic loss in this region all the loss can be attributed to coupling loss allowing us to see the effect of this known loss on the microscope output thus providing internal instrument calibration. In order to make the results more robust we take 4 different known attenuation (corresponding to different gradients of Eq. 5.8) to average the instrumental contribution. Summarizing we see therefore, in confocal system, the signal can only be collected by the objective lens in positive defocus distance. This backward artificial surface wave of s-polarized light can be expressed as

$$k_{ASP} = k'_{sp} - ik''_{ASP} \tag{5-9}$$

where k_{ASP} is the artificial surface wave k-vector and k''_{ASP} is the attenuation coefficient of the artificial surface wave. Therefore, the modulus of the artificial surface wave $ASP(y)$ can be expressed as

$$|ASP(y)| = 2k''_{c,artifical}\,\gamma \exp\left[\left(k''_{c,artifical}\right)y\right] \tag{5-10}$$

The expression is similar to the Eq.(5-5). The only difference is s-polarization cannot excite SP leading to no ohmic loss of the re-radiation. By measuring the gradient of the $\ln[|ASP(y)|]$, artificial attenuation $k''_{c,artifical}$ can be obtained. And the initial term $2k''_{c,artifical}\,\gamma$ can be obtained from the y-intercept. Now, the instrumental parameter γ can be calculated for self-calibration.

The advantage of imposing the gradient in the opposite direction to that of the normal surface wave is that we measure this wave at positive defocus ensuring that there are no interfering terms from real surface waves.

5.4 Experiment and Result

In this section, we will show the experimental results conducted by our proposed method. The experimental setup and the result of attenuation coefficient of coupling loss and ohmic loss will be discussed. As discussed in the previous section, two sets of data will be collected. One is the V(z) without artificial phase modulation. Another one is the V(z) with artificial phase modulation.

5.4.1 Experimental setup

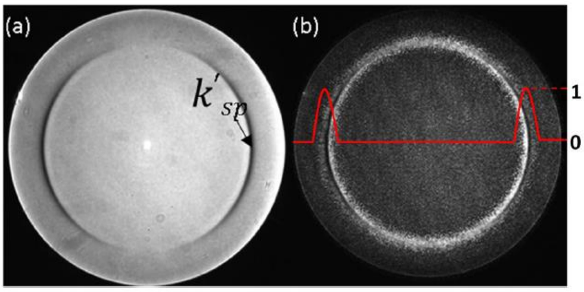

Figure 5-12 shows (a) experimental BFP image for Au sample with thickness of 46nm, (b) the experimental BFP image with amplitude pupil function modulation using phase-antiphase pairs pattern on the phase-SLM. The amplitude pupil function is shown in red (Pechprasarn et al., 2018)

Without additional modification on the optical configuration described on Figure 3-7, only phase modulation is applied. The BFP was modulated by the amplitude pupil function as shown on the Figure 5-12. As we are interested in the signal of SP, the reflection near normal direction is blocked.

5.4.2 V(z) Result

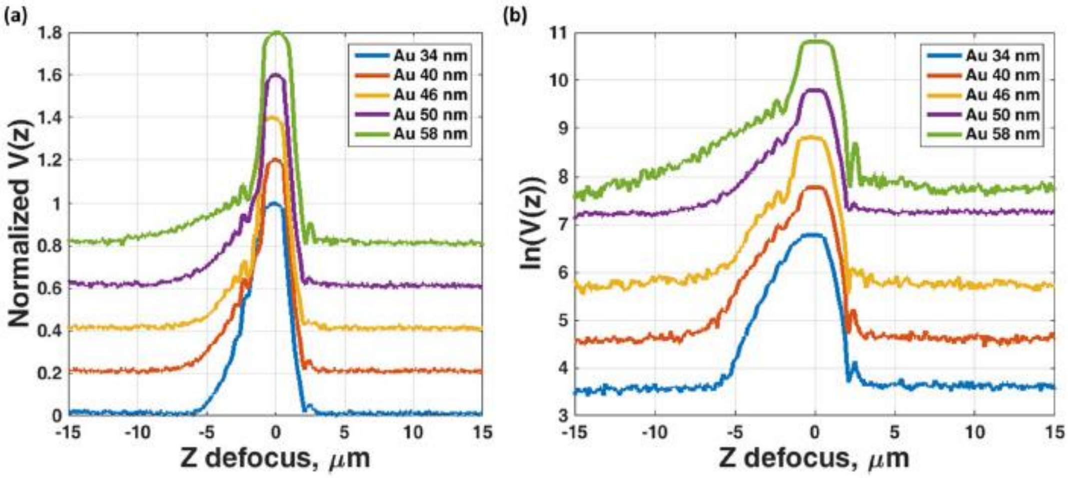

Figure 5-13 shows the normalized experimental V(z) attenuation measurement for 34nm, 40nm, 46nm, 50nm and 58nm thick of gold samples and (b) natural log scale of (a)

The total attenuation can be measured by V(z) measurement as shown on Figure 5-13. Then, the total attenuation can be calculated by measuring the gradient of the natural log of the modulus of the V(z) curve. The result is summarized in the Table 4.

Table 4 shows the attenuation coefficient k''_{sp} (in µm) for confocal V(z) measurement and values reported by Kolomenski et al.

Au thickness [nm]	k''_{sp} by V(z) measurement		k''_{sp} extracted from ref.
	Mean value	Variation coefficient	
34	0.3568	0.0029	0.2322
40	0.2391	0.0107	0.1600
46	0.1916	0.0067	0.1123
50	0.1534	0.0084	0.1039
58	0.0962	0.0111	0.0821

Each sample was measured 30 times to test the robustness and repeatability of the measurements. It is expected the $k^{"}_{sp}$ decreases as the thickness of gold increases. By modulating the BFP with the artificial phase, surface wave of s-polarization will be excited. The result is shown on Figure 5-14.

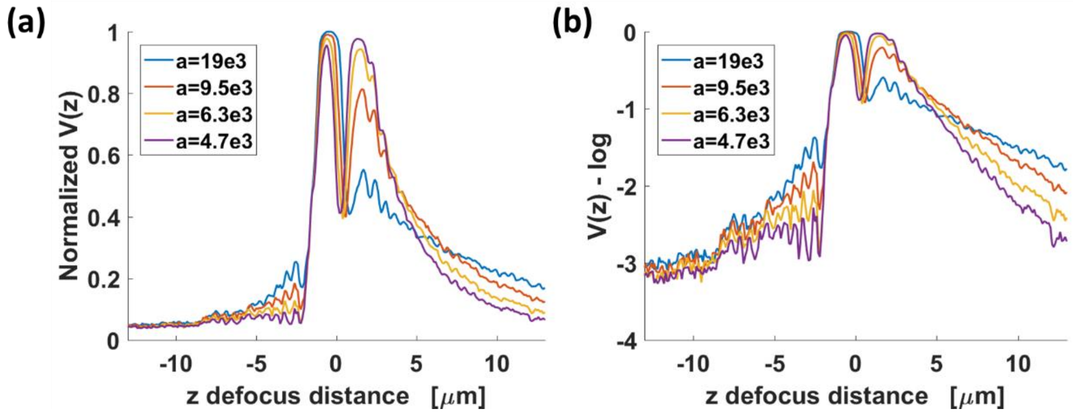

Figure 5-14 shows (a) normalized V(z) with artificial gradient on gold sample with thickness of 46nm at k_p = 0.0104 and (b) natural log scale in (a). The variable a is the gradient of the phase transition as described on Equation (5-8).

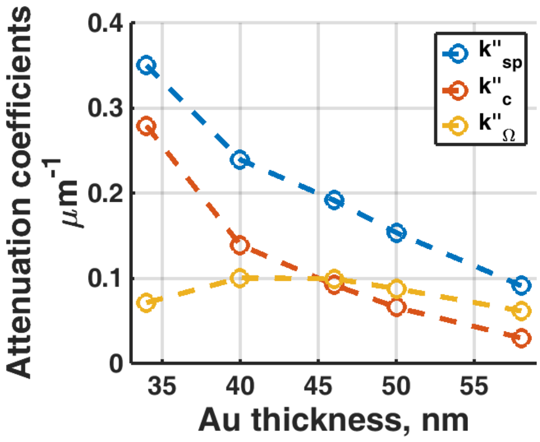

Figure 5-15 shows the attenuation coefficients

As discussed in the section of "Separation of Loss mechanism", instrumentation parameter γ can be obtained by the positive V(z) with artificial phase modulation on s-polarization to self-calibrate the system. For each sample, the recovered γ shows less than 5% deviation. Then, we use the mean value to separate the coupling and ohmic loss terms. The result on Figure 5-15 shows a very interesting intersection at around 46 nm thickness of gold, this is known to be very close to the thickness where the dip of the reflection coefficient reaches a minimum which is the position where the coupling and ohmic losses are equal.

5.4.3 Validation by simplified Green's function

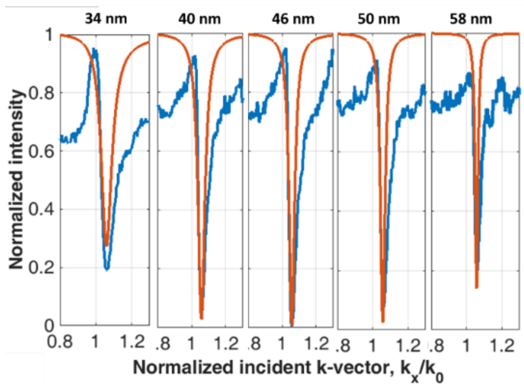

Figure 5-16 shows the matching of the green function (Pechprasarn et al., 2018)

In the previous section, the attenuation coefficients such as $k_{\mathrm{c}}^{"}$ and $k_{\mathrm{ohm}}^{"}$ on each sample are recovered. Up to this point, we can further validate the result by working out the reflection spectrum around excitation k-vector by simplified Green's function as shown in the Figure 5-16. Apart from the result in the case of thin gold (the case of 34 nm gold thickness), the agreement of the depth of dip in other cases are very good. On one hand, it indicates that it is reliable to recover the attenuation coefficients by the Goos–Hänchen phase engineering. On the other hand, it demonstrates the ability of simplified Green's function in relating the depth of the dip and the ratio of the coupling loss and ohmic loss.

5.5 Summary

In this chapter, we discussed the modelling of the V(z) of SP on our embedded confocal SPRM. We demonstrated that embedded confocal SPRM not only allows us to measure the total attenuation of SP, but also allows us to separate the loss between coupling loss and ohmic loss.

The measurement tells us that more information can be extracted from the reflection spectrum if the phase information of the reflection is also known. It leads us to think that the measurement of complete angular phase response will make it very attractive for understand the insight of the SP. Therefore, the goal of separating the loss mechanism of the coupling loss and ohmic loss on the SPRM was achieved by our novel idea of measuring the backward surface wave of s-polarization portion which is excited by imposing the artificial Goos–Hänchen phase on the SLM. In the next chapter, we apply a phase retrieval algorithm based on Ptychography to recover the complete angular phase information, this chapter will show that the alternative to controlling the phase distribution is measuring it.

Chapter 6 – Quantitative Phase Measurement by Back Focal Plane Ptychography

In the previous chapters we showed how a great deal of sample information may be extracted by manipulating the phase in the back focal plane with a spatial light modulator. In this section we discuss how to extract the phase information from the back focal plane using computational methods and we then use this to extract similar information to that obtained previously. We argue that this approach leads to considerable simplification of the hardware.

In this chapter, we proposed an innovative idea to directly capture the complex field on the BFP such that all information including amplitude and the relative phase of the re-radiated light emitted from the interface can be obtained, especially the SP signal. This technique not only allows us to extract more information from the sample but can be also implemented with a relatively simple and inexpensive system.

With the complete quantitative information of the BFP, it allows us to process the data in virtual (computational) way to obtain the results described in the previous chapter such as V(z), phase stepping, advanced beam profile modulation and attenuation of the SP signal; although the full knowledge of the phase profile in the BFP allows one to perform other more direct measurements that do not require the interferometric measurements discussed in the previous chapter. Indeed, with the complete information of the reflection, it also allows us to extract any available information with post processing, whereas when the phase of the back focal plane is manipulated in hardware it is normally necessary to perform a new experiment to obtain new information. This innovative measurement on BFP is not limited to plasmonic samples and can be applied to many other sample types such as metals, layered samples etc. For layered samples non-plasmonic surface waves are excited for which the back focal plane distribution gives a great deal of information for waves excited with both p- and s- polarization.

In practice, there are different advantages of intensity measurement and phase measurement of SP signal. In some cases, the intensity gives more easily accessible information, in others such as multilayer dielectric samples the intensity changes are not clear so that access to the phase information is very valuable. Also, it is also very difficult to extract information if there are multiple modes in the structure. A proper pupil function design with narrow bandwidth is challenging for standard V(z) measurement. This is because the narrow pupil function will dominate the ripple of the V(z) measurement. However, the problem of multiple modes can be solved by proper post-possessing when the complex field of the BFP is recovered.

BFP ptychography is also a useful tool to analyze angular response of a wide range of sensors. Not only can the excitation angle of the SP wave be measured, but also the quantitative phase information. By investigating the relative phase of the different incident angles light, insight of the sensor properties can be obtained, for example, the propagation length as discussed in the previous Chapter.

In this chapter, we will first discuss the details of the modified ptychographic iterative engine for our confocal SPRM. Then, we will discuss the experimental results on different samples such as gold samples with different thicknesses. Then, the results are validated by post processing techniques to extract additional information from the recovered complex field on the BFP. Finally, we will examine some interesting samples to illustrate the potential usage of this BFP ptychography technique.

6.1 System Design for confocal SPRM

In this study, we adapt the original ptychographical Iterative Engine (PIE) proposed by Faulkner and Rodenburg is described in the Chapter 2. A set of diffraction patterns for reconstruction will be captured from the sample with different illumination patterns in order to recover the phase of the object. However, some of the steps are modified for our embedded confocal SPRM. These will be discussed in later context.

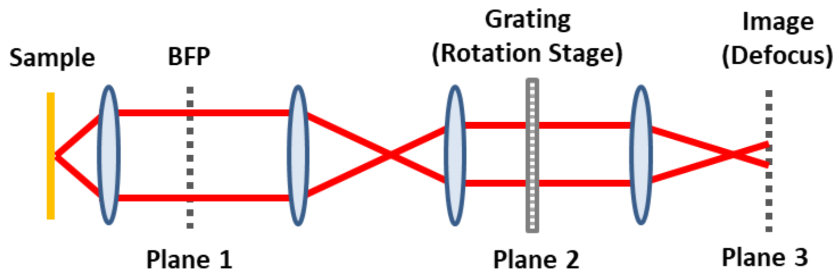

Figure 6-1 shows the optical arrangement among BFP, Ronchi grating and detector

In the design, the sample is illuminated by a focused beam. Then, the reflection from the sample is collected by the objective lens and formed on its BFP (Plane1) as shown on Figure 6-1. Then the wave function is projected on the conjugate Plane 2. By varying the patterns of aperture on Plane 2, a series of diffraction patterns will be formed Plane 3. Rather than recovering the phase of the object, in this experiment, the field on the BFP serves as our unknown guess function. The image plane on Plane 3 serves as the corresponding transform plane (or diffraction plane). In order words, we are going to recover the complex value of the BFP, so the image plane of the microscope serves as the diffraction plane. As a result, the complex field of the angular response of the focused beam will be recovered. Secondly, the measured diffraction plane is slightly defocused. This is because there is a strong intensity peak at the central focal which will saturate the camera and reduce the dynamic range of our measurement. By defocusing the energy spreads to a larger area and hence more detail of the signals can be captured.

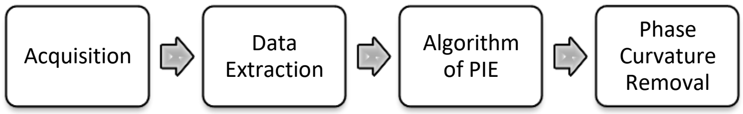

Figure 6-2 shows the flowchart of data handling

For the data handling in our system as depicted on Figure 6-2, we will capture two sets of data which are the images of Ronchi grating arrangement and the intensity images of the corresponding diffraction patterns. As the performance of the recovered result relies on the accurate knowledge of the probe position (Beckers et al., 2013; Shenfield & Rodenburg, 2011; Sun, Chen, Zhang, & Zuo, 2016; F. Zhang et al., 2013), the position of the probes should be measured accurately for the algorithm to give reliable results. We then extract the probe information by the BFP images followed by application of the conventional PIE algorithm. As the diffraction pattern is measured at defocus, we design a simple algorithm to remove the phase curvature of the recovered complex BFP. This step of phase curvature removal will be discussed in a later section in this chapter. In the later section, the design of the probes and the corresponding extraction method will also be discussed.

6.1.1 Probe Design for Ronchi Grating Ptychography

For a conventional ptychography implementation, the illumination probe is circular in shape. The algorithm requires several overlapping probes, so successive probes are shifted by a certain distance such that there is a sufficiently large overlapping region between the current probe and the next probe. However, in this study, we decided to use Ronchi grating with 50% duty cycle as the pattern of the probe. The new probe can be easily obtained by rotating the Ronchi grating. Therefore, it is not necessary to worry about the overlapping region as they will always overlap each other. One of the advantages of using Ronchi grating is that it can help us to accurately determine the scaling factor of the system. On the other hand, Ronchi grating can give better overlap uniformness for ptychography. With better overlap uniformity, recovered quality can be improved. (Huang et al., 2014) The discussion concerning the extraction of the scaling factor of the system will be discussed in a later section.

The largest period of the Ronchi grating on the commercial market is 5 line pairs/mm. As the size of the BPF of the objective is around 10mm, the estimated the number of periods within the BFP is around 50. If the number of periods with the BFP is too high, this reduces the tolerance to error in the lateral shift. Therefore, we de-magnified the size of BFP from Plane 1 to Plane 2 to reduce the ratio of number of periods of the grating within the BFP.

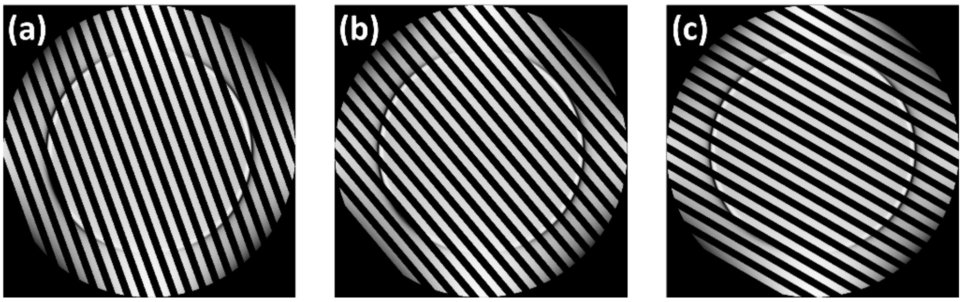

Figure 6-3 shows the simulated exit intensity of BFP covered by Ronchi grating in different orientations

In our design, the nominal number of periods per BFP is around 20. By rotating the Ronchi grating attached to a rotation stage (see Figure 6-3), a series of diffraction patterns on the Plane 3 are recorded which is the Fourier projection of the exit wavefunction on Plane 2. It is important to note that the rotation center is arranged outside the BFP. There is a simple practical reason for having the rotation center outside the BFP because if it is inside there will no change in the center so this region not see a change in illumination preventing its proper recovery.

Principle of Probe Extraction

As mentioned above, the probe in this study is not circular shape, our probe is a Ronchi grating. Therefore, it may be useful to define the probes in term of grating period P and the orientation angle θ rather than position vector. For convenience in the latter context, we describe each probe in term of state $S(P, \theta_n)$.

We developed a simple, robust algorithm to extract the state of the Probe by recording the images on the plane of the Ronchi grating.

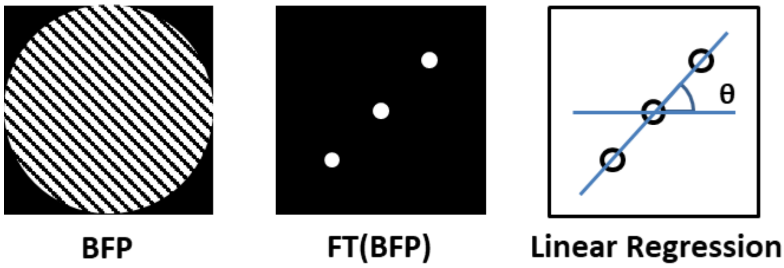

Figure 6-4 shows workflow of measuring the state of the probe

As the main feature of the exit wavefunction is a 2D square wave, it will form a series of peaks the plane 3 of Figure 6-1 according to the period of the object plane. Therefore, the state of the probe can be easily extracted from the recorded BFP image from these peaks. First, the period of the square wave can be extracted by locating the relative peak position. Second, the orientation angle can also be computed by those peaks on Fourier domain as shown on Figure 6-4. The locations of the peaks can be expressed slope-intercept form, $\mathrm{y} = \mathrm{mx} + \mathrm{c}$. The orientation angle θ can be easily computed by arctan of the slope such that $\theta = \tan^{-1} m$. Lastly, an additional phase shift is needed to shift the probe to the correct probe position, this may be performed by comparing the phase difference between the actual grating pattern and a synthetic pattern with the known period and orientation. This allows one to obtain very accurate measures of the probe thus allowing the corresponding fields on the BFP to be re-created with the ptychography algorithm.

6.1.2 Removal of the additional phase

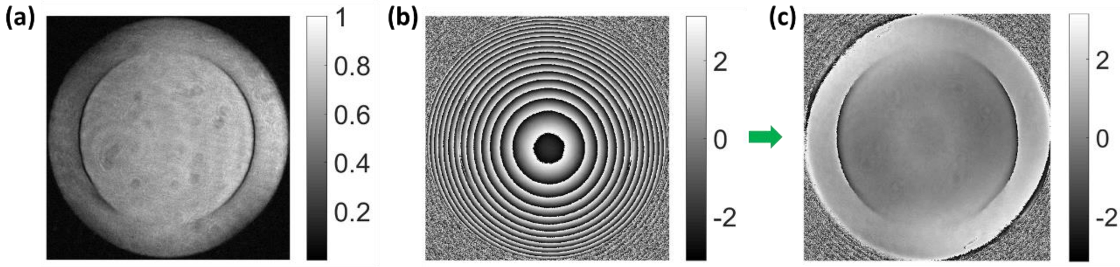

Figure 6-5 shows the recovered BFP - (a) amplitude, (b) phase and (c) phase after pupil correction

As the intensity images are measured on defocus plane, a phase curvature will be integrated on the recovered object wavefunction. This curvature can be expressed as $\exp(ik(1-\cos\theta)z)$ where k is the k-vector in free space, θ is the incident angle of the plane wave to the detector, z is the defocus distance of the detector. To remove the phase curvature, an automatic algorithm is developed to determine the curvature according to the strength to DC signal. Essentially, the principle of the algorithm is to transform the recovered BFP to the image plane with the reverse curvature phase pupil function. Then, we can record and compare the peak intensity value on each image. It is expected that recovered BFP with correct defocus pupil function will give maximum peak value on image plane in our case as there is no significant phase variation in the center part of the BFP. By fitting the peak value against defocus curvature, the corrected BFP can be obtained by removing defocus curvature as shown on Figure 6-5.

6.2 Performance Analysis

Accurate translation position determination is the key in ptychographic iterative engine algorithm. (Hurst et al., 2010; Thibault, Dierolf, Bunk, Menzel, & Pfeiffer, 2009; F. Zhang et al., 2013) Before processing the data, it is worth analyzing the potential source of errors and the corresponding effects in order to understand the influence of the parameters. In this section, the intensity offset, spatial scaling matching, dynamic range error and defocus distance will be discussed.

6.2.1 Dynamic Range and Defocus

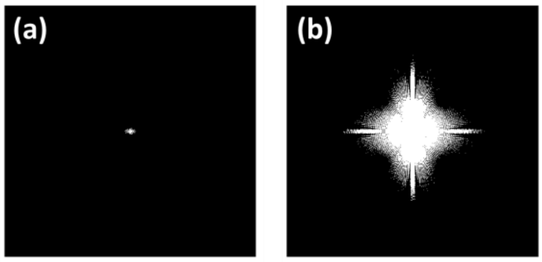

Figure 6-6 shows the simulated image quantized with the detector (dynamic range = 30000:1) on the image plane with effective numerical aperture NA of 0.02 - (a) at focus and (b) at defocus of 20 mm. The white region on the image represents that intensity levels with values corresponding to at least one intensity level.

The effect of dynamic range of a detector will be discussed in this section. Considering a focused beam on a detector, the light is confined at the center. As the dynamic range of a standard camera is limited, without saturating the camera, information on the high frequency region is lost as shown on Figure 6-6(a). When the detector is placed at the defocus plane, the focused beam is now spreading in a larger region. More information can be recorded as shown on Figure 6-6(b). It is of course very important to recover information over an extended range as this defines the resolution of the recovered field. The simulation demonstrates that more photons can be measured by the camera at defocus distance with fixed dynamic range. In order words, the required dynamic range of the detector is huge when it is in focus whereas the required dynamic range of the signal is greatly reduced when the image is measured on the defocus plane. Therefore, information in the high frequency bands on the image plane can be captured allowing us to have better reconstruction. It is the frequency range in the image plane that determines the angular resolution in the back focal plane. Now, let us investigate the effect of the defocus distance.

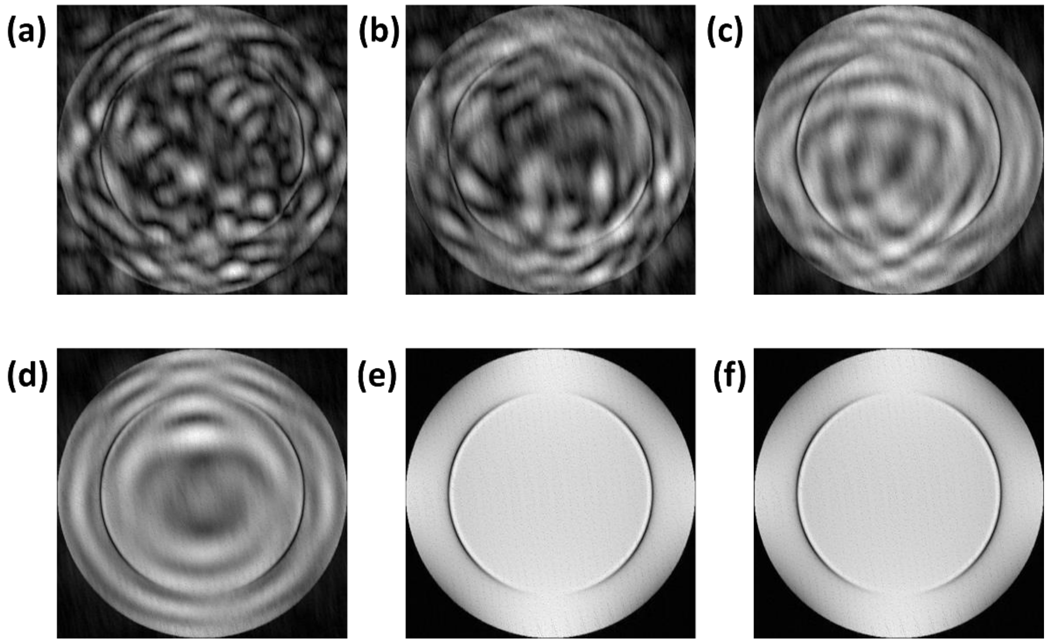

Figure 6-7 (a-f) show simulation of recovered modulus of BFP at defocus distance of 6 mm, 6.5 mm, 7 mm, 7.5 mm, 8 mm and 8.5 mm by the detector (dynamic range = 30000:1) respectively

Assuming detector dynamic range of the detector is 30000:1 which is used in this simulation (the quote value of dynamic range for the Andor Zyla camera is 33000:1), it represents some deviation form idea behaviour and not fully saturating the camera. Using these assumptions, the intensity images are recorded at different defocus distances. After ptychography algorithm, the field on the BFP are recovered. The modulus of the fields on the BFP recovered by the corresponding diffraction images are shown on Figure 6-7. For the recovered field on Figure 6-7 (a-d), the recovered results are very poor. Due to the highly concentrated intensity, only few pixels can survive (Intensity level > 0) to give the information. The recovered BFPs of (a-d) can be regarded as a low-pass filtered BFP. However, the recovered BFP on Figure 6-7 (e-f) are much better when the defocus distance is sufficiently large. Therefore, there are sufficient frequency components on the diffraction plane to reconstruct the BFP.

6.2.2 Error Analysis of Dynamic Range of Images

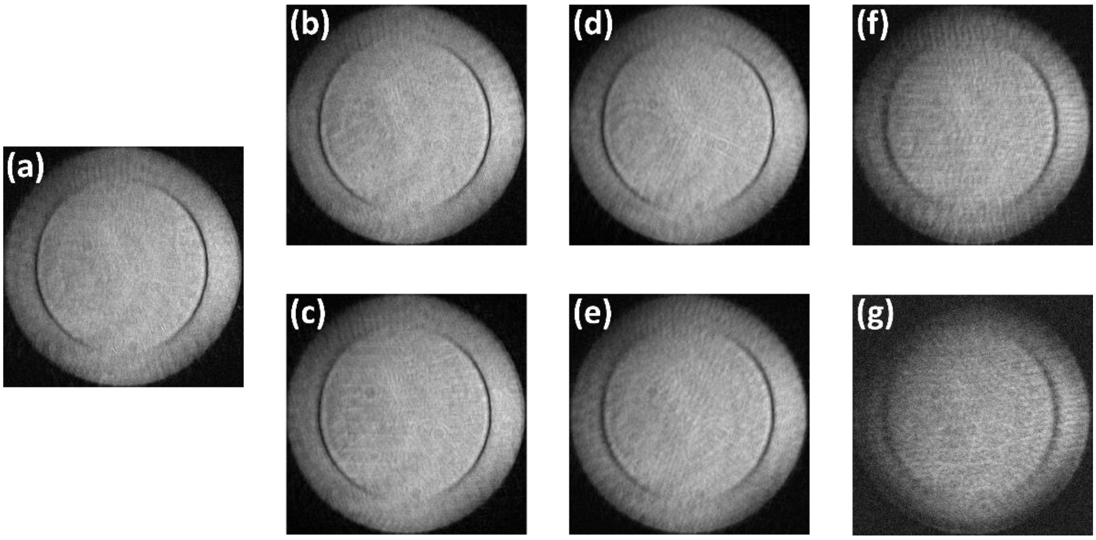

Figure 6-8 shows the modulus of the recovered field on BFP with respect to the dynamic range of the detector– (a) 33000:1, (b) 16000:1, (c) 4096:1, (d) 1024:1, (e) 256:1, (f) 64:1 and (g) 16:1. The diffraction images are measured on the plane of the defocus distance of 25mm.

For this analysis, the experimental diffraction patterns on image plane with the dynamic range of 33000:1 were recorded. In order to analyze the effect of the dynamic range of a detector, the recorded diffraction patterns are re-quantized in lower dynamic range format. Then, the re-quantized data will be used to recover the field on the BFP in the same condition. The modulus of recovered BFP can be seen on Figure 6-8. Although the dip position can be correctly recovered, the quality of the recovered field patterns on the BFP with low dynamic range are not very good (see

Figure 6-8 f and g). This can be explained by the similar reason such that the loss of the high frequency components (as the intensity of high frequency components is very low as shown on Figure 6-6) so that the recovered BFP cannot form a sharp edge. For further analysis, the line traces of the recovered BFP are plotted on Figure 6-9.

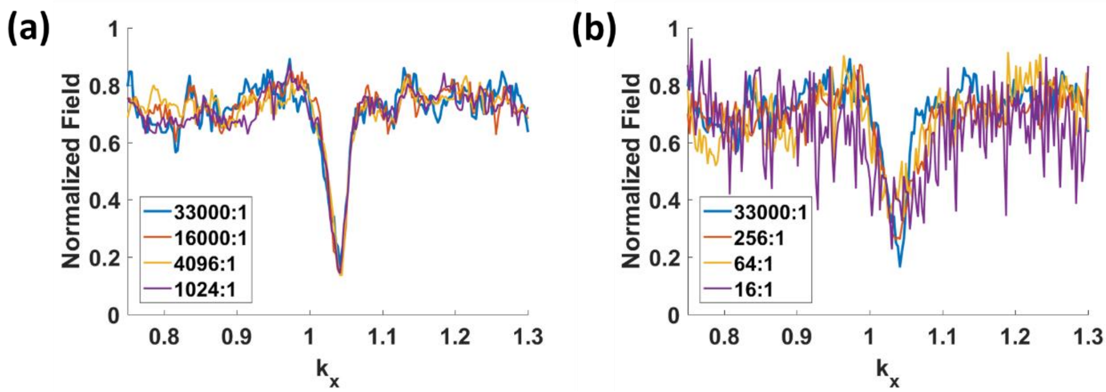

Figure 6-9 shows the cross section of the modulus of the BFP of Figure 6-8

It can be seen on all of the recovered BFP can give the correct position of the dip although the quality of the dips with low dynamic range are rather poor. It shows the recovered dip position is independent of the number bits of the recorded intensity on the image plane. Also, it is clearly on the Figure 6-9a that the width of the dips agrees very well. We can conclude that provided we can recover by the recorded image with dynamic range of at least 1024:1 at the chosen defocus.

6.2.3 Error Analysis of Scaling factor

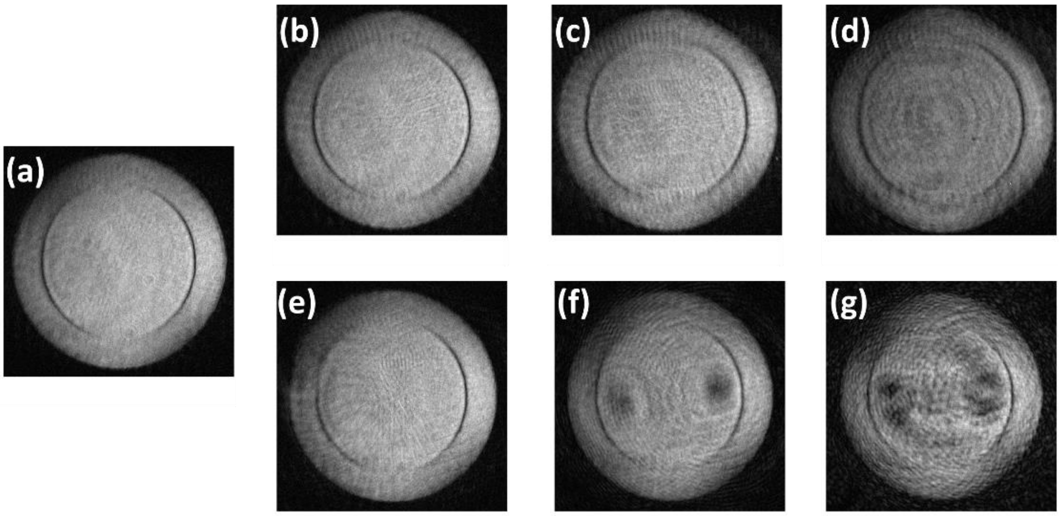

Figure 6-10 shows the modulus of the recovered wavefunction on BFP with respect to scaling error using experimentally measured images in plane 3– (a) 0%, correct magnification, (b) -2%, (c) -4%, (d) -6%, (e) 2%, (f) 4% and (g) 6%.

The scaling factor is defined as the ratio between the numerical aperture of the detector NA_{image} and the numerical aperture of BFP NA_{BFP}. The scaling factor between the plane 1 and plane 3 has to be accurately determined (see Figure 6-1). The quality of the recovered BFP will be degraded if the scaling factor is not correctly determined. In this section, the effect of scaling factor error ranging from -6% to 6% is simulated from the experimentally determined recorded patterns. It can be seen on Figure 6-10 that the irregular patterns are observed on the recovered BFP distributions when the scaling error increases. When the error of the scaling factor is greater than 1, the performance of the recovering become even worse than the case for values less than 1. The poor recovery due to the error of the scaling factor because the fact that PIE relies on the accurate model between object plane and Fourier plane. Therefore, it shows the importance of accurate measure of the scaling factor between two planes. This is one of the advantages of using Ronchi grating instead of circular probe because scaling factor of the system can be accurately determined from the projection of Ronchi grating.

6.2.4 Learning Rate

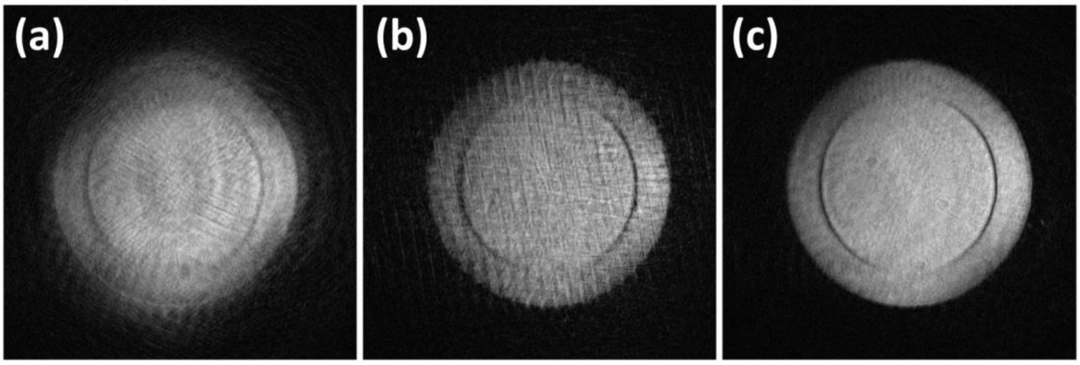

Figure 6-11 recovered result with the learning rate β of (a) 0.2 for each iteration, (b) 0.8 for each iteration and (c) 0.8 to 0.2 as the iteration process proceeds

Figure 6-11 shows that recovered BFP with the different settings of the learning rate. In order to obtain global solution, the learning rate is properly selected during the iterations. If the learning rate is too small (for example β = 0.2), the recovered BFP will be trapped in the local minimum resulting relatively poor solution. For large learning rate, the solution appears to oscillate between solutions missing the optimal position of the global minimum. For this reason, we gradually reduce the β as the iteration process proceeded. Figure 6-11 shows that the BFP can be recovered with very good quality. In the later section, we will examine the quality of the recovered result.

6.3 Experiment and Results

In this section, we move on to the experimental section. I will show the optical configuration followed by the standard raw images captured by the cameras for reconstruction. Then, a series of experiment is conducted to show the great performance of this technique.

6.3.1 Optical Configuration

In this experiment, the optical configuration is modified compared to the previous optical configuration, the system remains simple or even simplified as shown in Figure 6-1 (The detailed configuration as shown in Figure 6-12). The beam from HeNe laser (632.8 nm, 10mW) is magnified to the 1.49 NA objective lens (Nikon, CFI Apochromat TIRF, oil immersion, 60x). The beam is then focused on the sample and reflected. The reflected light is then passed to the pellicle beamsplitter. The conjugated plane of the BFP, formed by a lens with focal length of 75 mm, represent the angular response of the incident light is presented on the back focal plane.

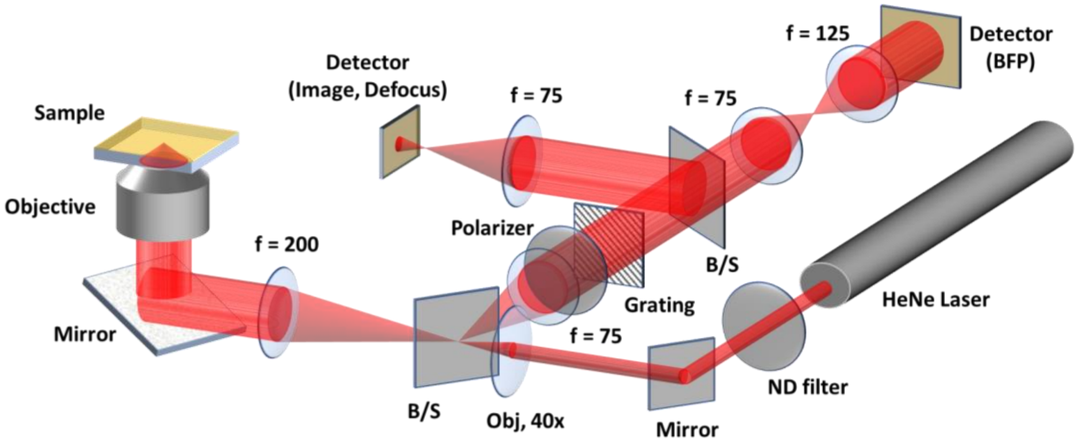

Figure 6-12 Detailed Optical configuration

The Ronchi grating (Edmund Optics, 5 line pairs/mm) is aligned on the conjugate plane of the BFP of the objective lens. The measured plane is on the image plane with slight defocus. It should be noted that polarizer is inserted between the Plane 1 and Plane 2 as shown on the simplified configuration on Figure 6-1. It is used to simplify the system such that only the field along x-direction will propagate to the Plane 2.

The camera (Thorlabs, DCC3240M, 1280 x 1024) on conjugate BFP is used to measure the probe information for the PIE algorithm. The camera of image plane is an Andor CMOS Camera (Zyla 5.5, 2560 x 2160). The rotation of the Ronchi grating is controlled by customized rotation stage. The detailed configuration of the rotation stage is described on the section “Design of Rotation stage” in Chapter 3.

6.3.2 Images obtained by the detectors

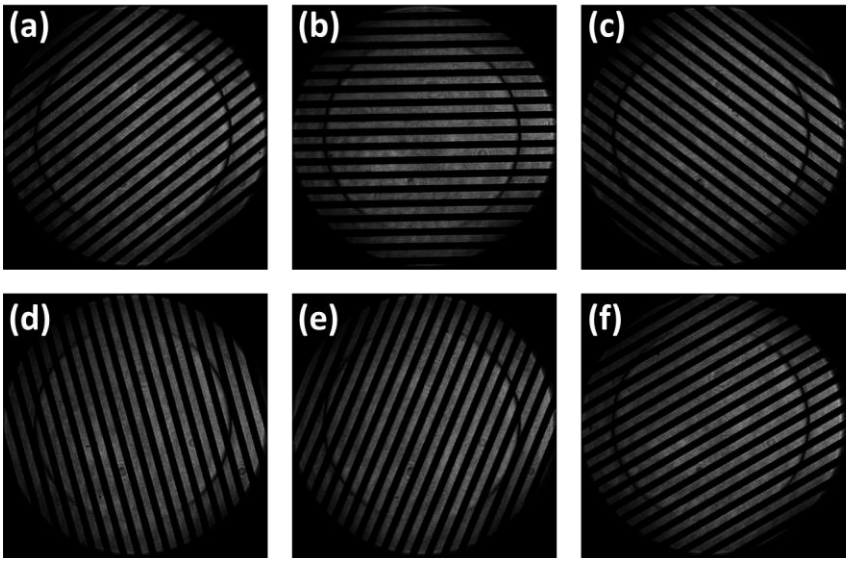

Figure 6-13 shows experimental images on the BFP in different orientation of the Ronchi grating

The experimental images captured on BFP are shown on Figure 6-13. The quality of the Ronchi grating is such that the beam is blocked completely. By transforming the BFP image as described above, the calculated period of the grating in the BFP is around 19.5.

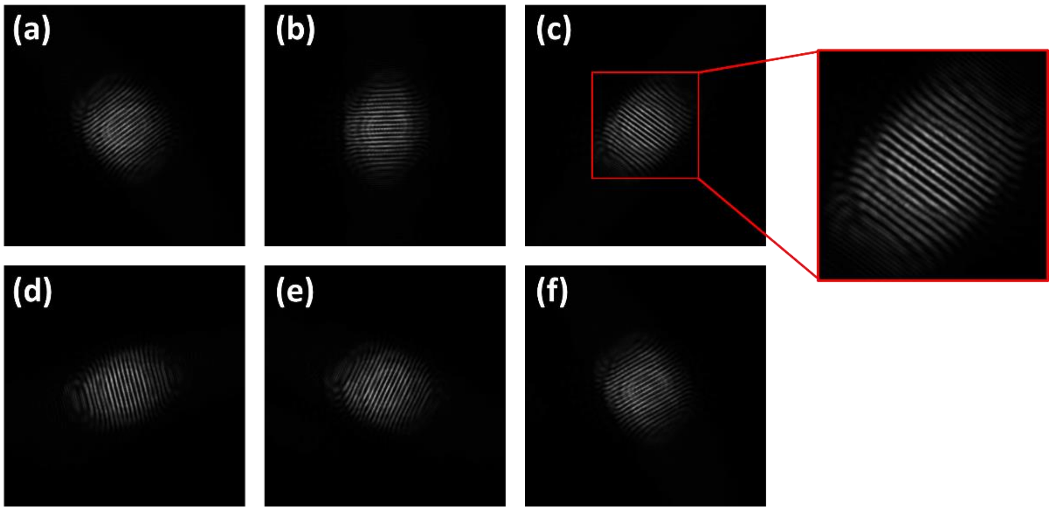

Figure 6-14 shows the zoomed images captured on image plane at defocus distance of 25 mm

The experimental images captured on BFP are shown on Figure 6-14. It is interesting that there are some fringes on the images because of the overlapping of the diffraction orders. We believe that this overlapping provides extra constraints to the estimated guess to ensure better uniqueness.

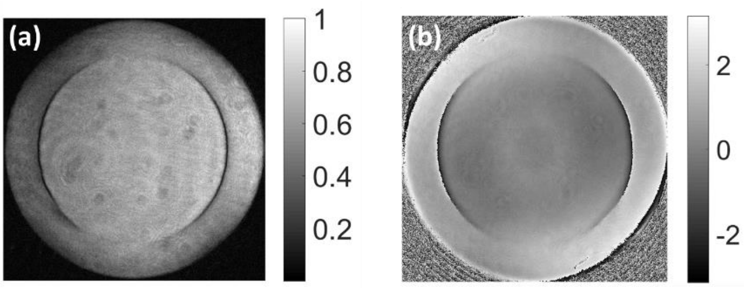

Figure 6-15 (a) and (b) shows the recovered modulus and phase of the wavefunction on BFP respectively

By following the processing procedure as described in the Figure 6-2, the reconstructed complex wavefunction on BFP is obtained which is shown on Figure 6-15.

6.3.3 Advanced Processing Strategy

Somekh proposed an algorithm to estimate the original modulus of the reflectance coefficients by least square estimation on the recorded intensity of BFP. In the algorithm, it makes use of the intensity at different azimuthal angles. Because of the cross term of the p-polarization and s-polarization, the algorithm involves 3x3 matrix. However, in our case, the matrix can be reduced to 2x2 matrix as we know the complex information of the BFP, which means there is no need to consider cross terms as in the case of intensity only information Now, considering the field of the BFP along x-direction which is

$$E_x = r_{p\alpha} \cos^2 \phi + r_{s\alpha} \sin^2 \phi \tag{6-1}$$

where the reflection coefficients $r_{p\alpha}$ and $r_{s\alpha}$ are the reflection coefficients for p-polarization and s-polarization respectively. By separating E_x in term of real and imaginary parts, we have

$$\mathrm{Re}(E_x) = r'_{p\alpha} \cos^2 \phi + r'_{s\alpha} \sin^2 \phi \tag{6-2}$$

$$\mathrm{Im}(E_x) = r''_{p\alpha} \cos^2 \phi + r''_{s\alpha} \sin^2 \phi \tag{6-3}$$

Where $r_{p\alpha} = r'_{p\alpha} + ir''_{p\alpha}$ and $r_{s\alpha} = r'_{s\alpha} + ir''_{s\alpha}$.

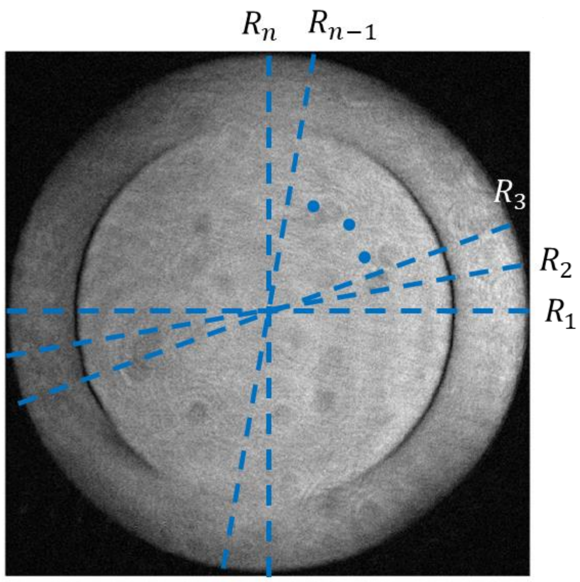

Figure 6-16 shows the line-trace measurement on BFP

Taking the real part ($\mathrm{Re}(E_x)$) as an example, we can take n line-trace measurements with different azimuthal angles ∅ on the BFP and denote the line trace as R_n as shown on Figure 6-16. As all the measurement are a the linear combination of $r'_{p\alpha}$ and $r'_{s\alpha}$, we can find the best fit to all the measurements by least square method on $\sum_n \left(R_n - r'_{p\alpha}\cos^2\phi_n - r'_{s\alpha}\sin^2\phi_n\right)^2$. Then, $r'_{p\alpha}$ and $r'_{s\alpha}$ can be computed by the matrix as follow:

$$\frac{1}{2}\begin{bmatrix} \sum_n \cos^4\phi_n & \sum_n \cos^2\phi_n \sin^2\phi_n \\ \sum_n \cos^2\phi_n \sin^2\phi_n & \sum_n \sin^4\phi_n \end{bmatrix}\begin{bmatrix} r'_{p\alpha} \\ r'_{s\alpha} \end{bmatrix} = \begin{bmatrix} \sum_n R_n \cos^2\phi_n \\ \sum_n R_n \sin^2\phi_n \end{bmatrix}$$

Similarly, $r''_{p\alpha}$ and $r''_{s\alpha}$ can be recovered from the imaginary part of E_x. By combining the recovered result, the complex reflection coefficients $r_{p\alpha}$ and $r_{s\alpha}$ are reproduced.

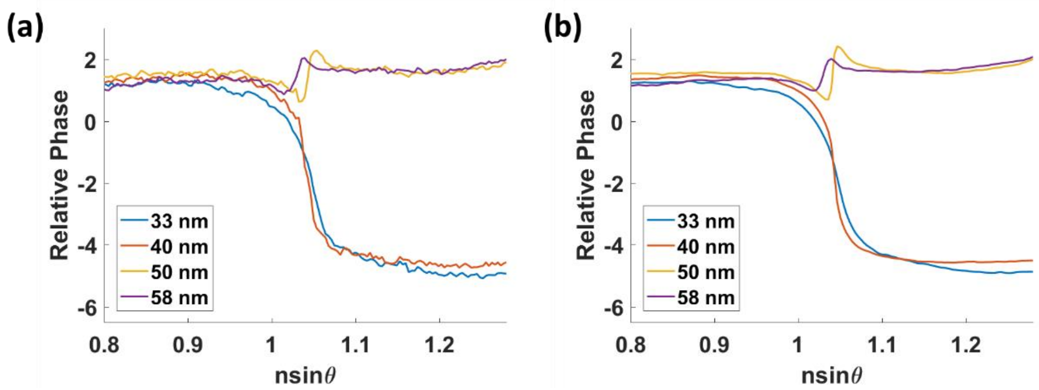

Figure 6-17 shows the line trace of the phase of p-polarization on gold samples of different thicknesses. (a) the original recovered phase (by PIE algorithm) and (b) the phase further estimated by least squared method

We examine the algorithm to recover the reflection coefficient of r_p by the sample of different thicknesses. Figure 6-17 clearly shows that the single line trace of the phase of r_p contain noticeable phase noise. However, by the least squares method, the phase noise is substantially removed and the best fit of the r_p shows very good agreement of the phase change with respect to k-vector. In the latter section, we will examine the phase change and further recover the attenuation of the SP.

6.4 Validation of Recovered Result

6.4.1 Comparison of Direct Measurement

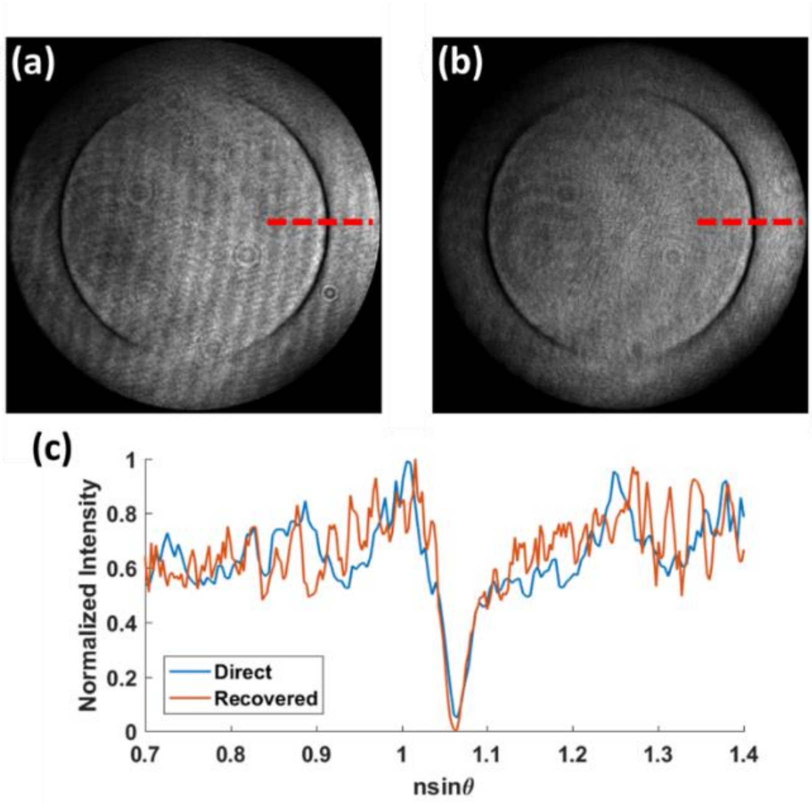

Figure 6-18 shows the intensity on BFP - (a) direct measurement by detector, (b) recovered intensity and (c) the cross section

In order to check performance of the recovered result, we first compare the intensity of the recovered result and the intensity image directly captured from the camera. The results are shown on Figure 6-18. It can be seen that lots of details including the defects on can be recovered BFP. A major difference is that there are the weak fringes on the direct measurement. We believe that it is probably due to multiple reflection on the protective glass on the detector used on the BFP. It also shows that the recovered result can avoid this situation as any fringes would appear on an image plane which when processed would be dispersed in the recovered image. In the Figure 6-18(c), it shows the trend of the line traces along x-direction is consistent.

Indeed, a simple and robust way to retrieve the phase information is our goal of this thesis. As the complex field of the BFP is recovered, we can extract more information for a wide range of analysis. For example, the properties of the sensor such as propagation length of the SP can be computed by the standard confocal V(z) measurement as discussed in the Chapter 5. In the virtual confocal measurement, the size of the confocal pinhole can be infinitely small rather than finite size so that the confinement can be much better. In the next section, we will perform a series of virtual optics computations to show the consistency of the phase result on recovered result and measured result.

6.4.2 Dip Recovering on ITO sample

In this experiment, we are going to demonstrate the performance of BFP Ptychography on detection of dip movement.

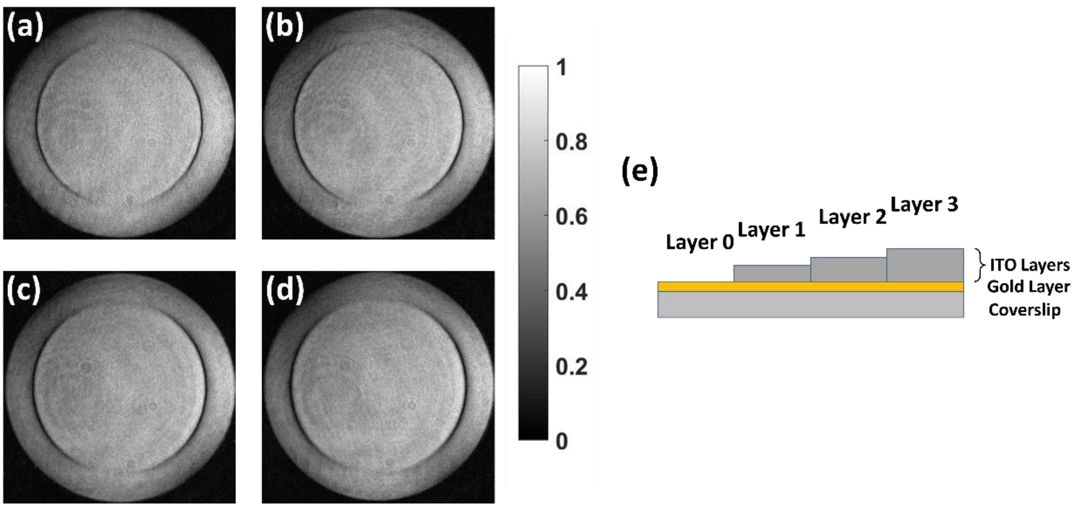

Figure 6-19 the recovered amplitude of BFP on (a) Layer 0, Bare Gold, (b) Layer 1, (c) Layer 2, (d) Layer 3 and e) the schematic diagram of the structure of the samples

In this experiment, the complex fields of different ITO layers (the structure is shown on Figure 6-19 (e)) on BFP are recovered by ptychography algorithm. It shows that the dip on the BFP is moving outward to the edge as the thickness of the ITO layers increases. This indicated that the SP in higher effective medium requires higher k-vector to excite.

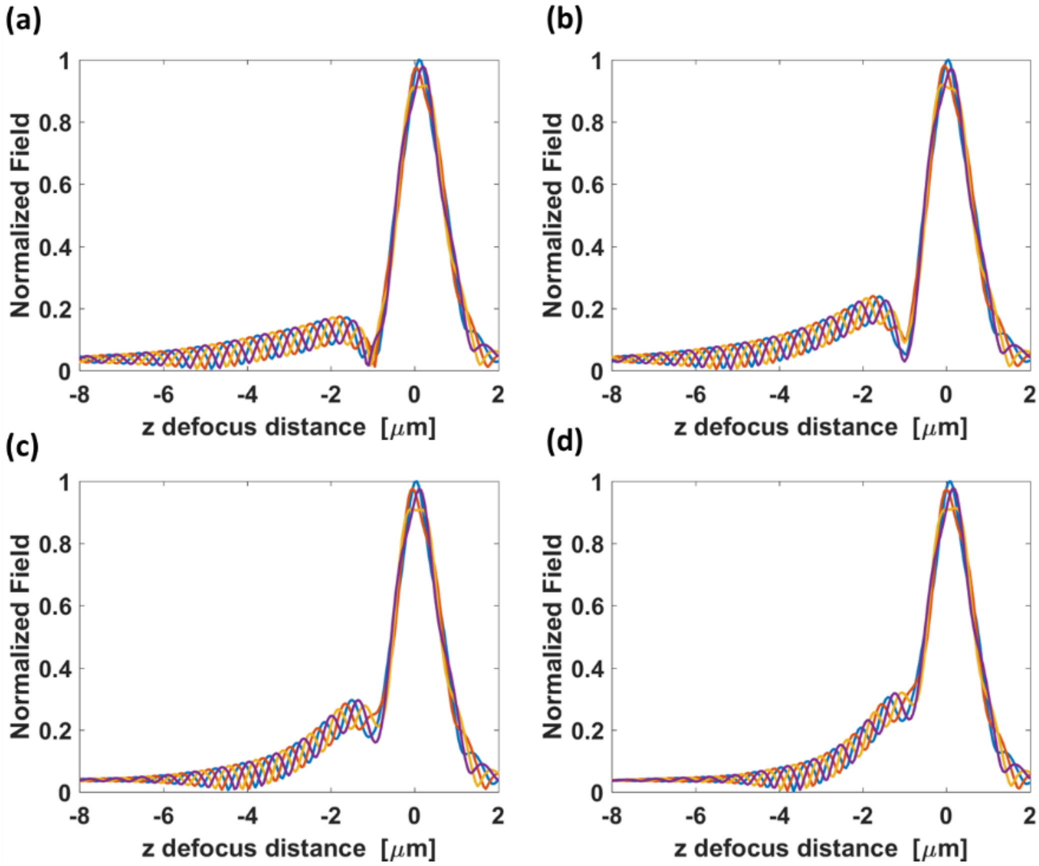

Figure 6-20 shows phase-stepping of the V(z) based on recovered BFP ITO layers. (a) Layer 0, (b) Layer 1, (c) Layer 2 and (d) Layer 3

Now, we are going to examine the agreement of the recovered thickness of the ITO layers between the dip position of BFP and the phase-stepping approach (see Figure 6-20). With this examination, it can show whether the phase is recovered correctly as the dip position on the BFP should be the same position where the phase transition is.

Table 5 shows the recovered thickness by the method of (i) PIE and (ii) measuring the dip position of the image on BFP

Method	Recovered Thickness [nm]			
	Layer 0	Layer 1	Layer 2	Layer 3
BFP	-	5.31	9.84	11.87
Phase Stepping	-	5.63	9.83	11.52

The recovered result is shown on Table 5. Layer 0 is bare gold layer which serves as reference layer so that the thickness of ITO is zero. The result shows that the agreement between dip position measurement and phase-stepping measurement is very good where the difference of the recovered thickness for all samples are less than 0.5 nm.

6.4.3 Quantitative measurement of angular phase response

Apart from the performance of monitoring the position of the dip, we would like to examine the phase quantitatively of the recovered BFP by the gold samples with different thicknesses. The nominal thicknesses of the gold layers were 33nm, 40nm, 50nm and 58nm.

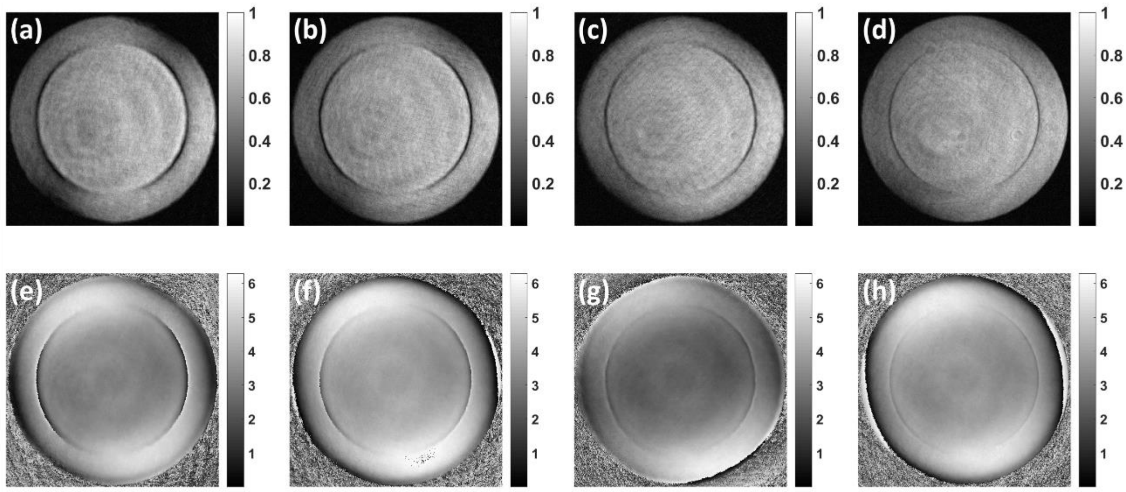

Figure 6-21 (a-d) and (e-f) show the recovered amplitude and phase of the BFP of different thickness of gold respectively. The thicknesses of gold sample are 33 nm (a, e), 40nm (b, f), 50nm (c, g) and 58 nm (d, h)

Figure 6-21 shows the recovered result of the samples of different thickness of gold layer. As the dielectric layer on the surface of the gold sample is air, the dip positions are almost the same for all cases. The difference is only the ratio of the coupling loss and ohmic loss as discussed in Chapter 5. This ratio difference will control the minimum intensity of the dip at resonance angle.

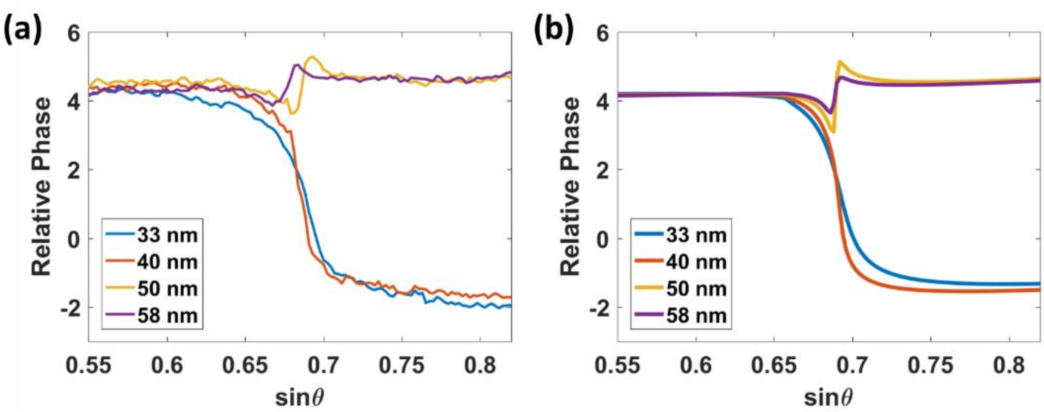

Figure 6-22 (a) and (b) show experimental and simulated the cross section of the phase on gold sample with thickness of 33 nm, 40 nm, 50 nm and 58 nm respectively

Before we perform virtual imaging by the recovered BFP, we can check whether the recovered BFP is consistent with the theoretical prediction. Figure 6-22 shows the line trace of the phase of the BFP. For thin gold sample with thickness of 33 nm and 40nm, there is a 2π phase transition because of the coupling loss is greater than ohmic loss which can be explained by the simplified Green's function as discussed on Chapter 5. For thick gold sample with thickness of 50 nm and 58 nm, it will not undergo 2π phase change as the ohmic loss is greater than coupling loss. It clearly shows that the recovered phase of the BFP is consistent with the predicted phase very well.

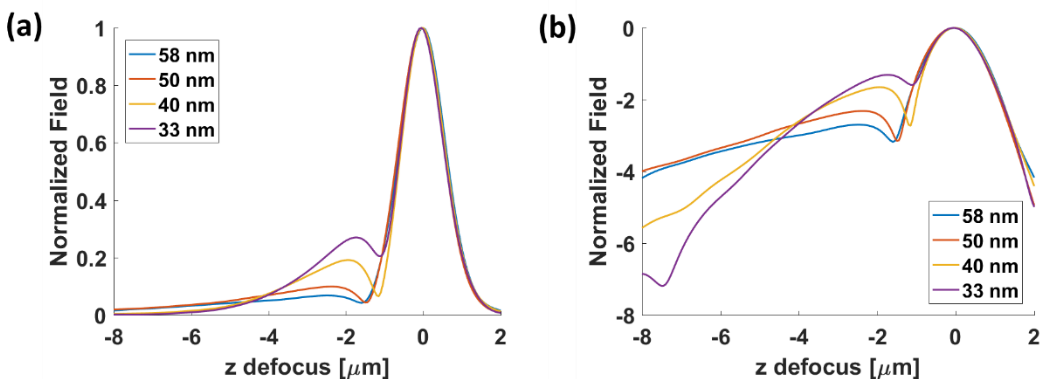

Figure 6-23 shows the V(z) curves by virtual optics. (a) Normalized V(z) and (b) the log scale of V(z) showing the linearity of the decay of SP as defocusing

Now, the recovered BFP is used to compute the V(z) curve. It can be seen that the V(z) curves shown on Figure 6-23 are smooth implying the confocal signal is averaged over different azimuthal angles. This is because there is no additional noise source arising from the optical path and the detector. On the other hand, it can be seen that the attenuation is much greater as the thickness of the gold decreases. The recovered attenuation coefficients of the samples with different thicknesses are summarized below.

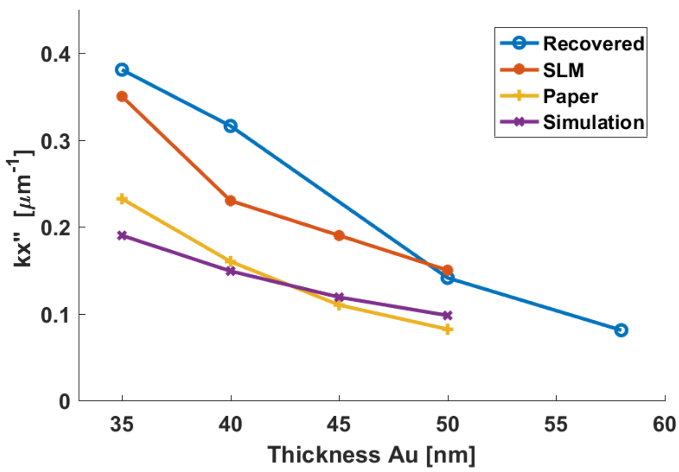

Figure 6-24 show the recovered attenuations on gold sample with different thicknesses

The result shown on Figure 6-24 are the recovered attenuations from the gold samples with different thicknesses. The blue curve is recovered attenuation based on the recovered complex BFP by Ptychography algorithm. The attenuation values were recovered by applying exactly the same processing as discussed in Chapter 5. The crucial difference, of course, is the recovered data in chapter 5 was obtained by hardware manipulation of the field with the SLM, in the present case once the back focal plane was recovered all the phase processing was performed in the computer. The red curve is the experimental measurement based on SLM based SPRM as described on Chapter 5. The yellow curve is the experimental result measured by Kolomenski et al. (Kolomenski, Kolomenskii, Noel, Peng, & Schuessler, 2009) The purple curve is the simulated result by Fresnel's Equation. The trend of the recovered attenuation is consistent with the reported values. We believe the gap between the curves is because of the surface roughness of the sample as described in the previous paper (Pechprasarn et al., 2018). However, in the same batch of the sample (the attenuations obtained by SLM-based SPRM and the ptychography measurement) are well-matched. Therefore, the performance of the ptychography in our experiment seems consistent with the SLM based measurements reported earlier.

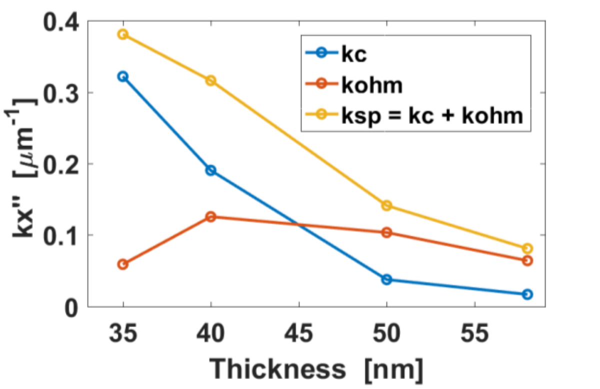

Figure 6-25 shows the recovered attenuation coefficients of coupling loss k_c and ohmic loss k_{ohm}

As discussed in Chapter 5, the coupling loss and ohmic loss can be recovered by imposing the Goos–Hänchen phase on the recovered BFP. Figure 6-25 shows that the attenuation coefficient of coupling loss and ohmic loss are consistent with the predicted trend. For example, the coupling loss decreases as the thickness of the gold sample increases and the ohmic loss is roughly constant. And it should be also noted that they meet approximately at 45 nm thickness.

6.5 Interesting Results from Other Samples

6.5.1 Transparent sample

As mentioned in the previous section, one of the issues on the transparent sample that there is no dip or a very weak dip on the reflection spectrum of the transparent sample. In this case, we are not able to monitor the dip movement by tracking the dip position. Therefore, measuring the position of the phase change becomes the possible solution to this kind of problems. You may think that V(z) can help to solve the problem as well by measuring the gradient. However, V(z) is obtained by relative phase between SP and Ref signal along defocus z direction. Therefore, it may not be suitable for the sample where there are multiple modes available. Another issue with V(z) measurements with transparent samples is that the reflected beam at normal incidence which forms the reference of the interferometer is very weak, so the signal to noise ratio of the V(z) curves extracted is rather poor. This is not a problem with the ptychoghraphic measurements.

The setup in this experiment is the same system as described before. Only the gold sample is replaced by the transparent sample which structure can be seen on Figure 6-26 (b). The sample is prepared by fabricating LiF (Lithium Fluoride) and PMMA (poly(methyl methacrylate)) layer on the cover glass with refractive index of 1.52. The refractive index of LiF and PMMA are 1.39 and 1.49 respectively and the thicknesses of the LiF and PMMA layer are 600 nm and 450 nm respectively.

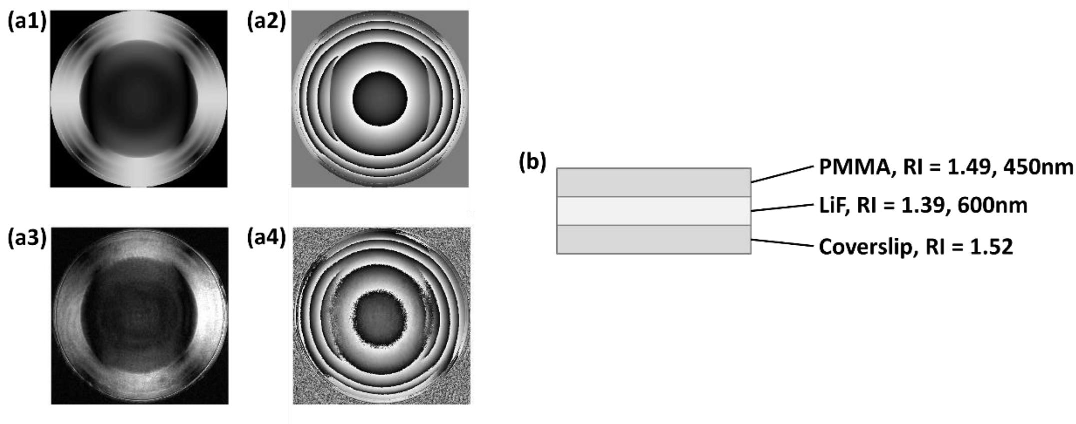

Figure 6-26 (a1) and (a2) show the amplitude of experimental and simulated BFP respectively; (a3) and (a4) shows the phase of the experimental and simulated BFP respectively. (b) shows the structure of the transparent sample

In general, the recovered BFP of transparent sample is consistent with the simulated BFP. Particularly, the features at the Brewster angle on p-polarization can be easily be identified which have a very similar shape to those of simulated result. On the other hand, it is interesting that the mode of p-polarization and s-polarization are slightly different. It can be easily seen by observing the phase change of BFP. Therefore, it is expected that BFP Ptychography can be a useful tool to investigate these types of samples.

6.5.2 Complex BFP of Au sample along y-direction

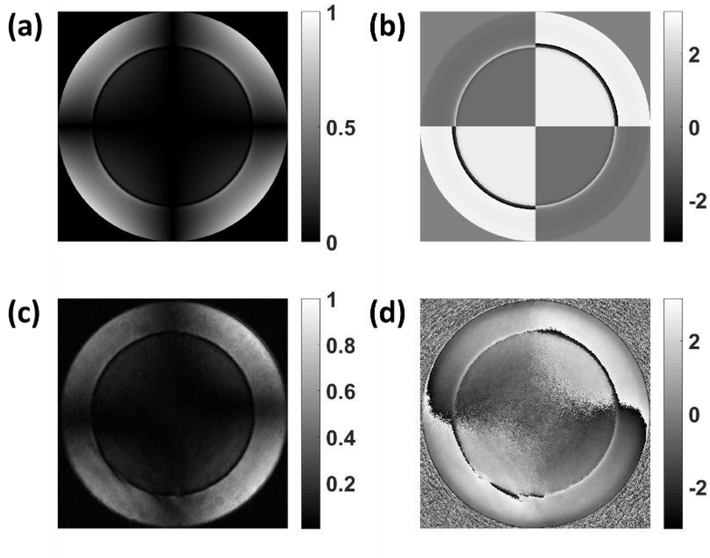

Figure 6-27 (a) and (b) shows the modulus and phase of the simulated BFP of Au sample along y direction respectively. (c) and (d) shows the modulus and phase of the recovered BFP of Au sample along y direction respectively. It is assumed that the input polarization of the light is along x direction (horizontal direction).

This recovered BFP of gold sample is obtained by selecting the electric field along y-direction instead of x-direction. It can be achieved by rotating the polarizer in front of the Ronchi grating by 90 degrees. As the exit field after reflection is the combination of p-polarization and s-polarization (as discussed in the Chapter2), there is no decomposed field along direction of pure p-polarization and pure s-polarization of light resulting no reflected on along y-direction as shown on the Figure 6-27(a). But it is more interesting that the phase is separated into four quadrants with each quadrant approximately shifted in phase by 180 degrees to the adjacent quadrant. It is clear that the recovered BFP is consistent with the simulated result. The center part of the recovered BFP is not very clear because of the low reflection. To investigate the center part of the BFP, we may block the light above critical angle to enhance the signal to the detector. In short, BFP Ptychograhy will be a simple and excellent tool to investigate the angular response of tested sample.

6.6 Discussion and Summary

In this chapter, we demonstrated that BFP Ptychography essentially recover the complex field of the BFP. With this technique, a variety samples were examined on the SPRM such as different gold samples, different ITO samples and LiF sample and a wide range of information can be extracted when the phase information of the BFP presents. The recovered phase information on BFP can be used to compute the field on the image plane virtually. Also, with the complex information, we can perform advanced post-processing technique to improve the signal to noise as well as the aberration by our algorithm based on least square estimation on different azimuthal angle of the BFP. On the other hand, the overall system is much more compact and direct although the system involves the rotating stage imposing different probe to the system. No additional SLM is required to be inserted before the objective lens. Therefore, it is convenient to be integrated into standard microscope by simply modifying the detection arm. Therefore, BFP Ptychography provides great potential for many other applications. Indeed, BFP recorded the angular information on the sample. Therefore, once we have the phase information, we have better insight of the interaction within the structure. For instance, intensity information in the back focal plane does not give spatial position on the sample, giving information of the spatial frequencies present over the whole field of view. With the phase information, however, we may also extract the spatial information by numerically propagating the fields through the optical system from the back focal plane to the sample plane. The phase information is thus a crucial first stage in developing techniques that allow measurement of many points simultaneously, this issue is discussed briefly in the suggestions for further work.

Hence, the goal of retrieving the quantitative phase information of the angular response (the field of the BFP) was achieved by applying our modified ptychography algorithm. The recovered result showed a good agreement with the result measured from the SLM-based SPRM.

Chapter 7 – Conclusion and Future Work

In thesis, we have developed different advanced strategies to extract the phase information for the confocal embedded SPRM in order to measure the k-vector of the SP so that we can monitor binding events on gold samples.

In Chapter 4, we developed several advanced modulation techniques to improve the performance of SPRM by SLM. It showed that SLM give a wide range of possibilities to modulate the wavefront of the illumination beam. It allows us to separate control of the reference beam and SP beam with relatively simple hardware. Also, we showed the acquisition time can be reduced by the technique of optical vortex modulation and Hilbert Transform.

In Chapter 5, we discussed the loss mechanism of the SP. We showed that the attenuation and the loss mechanism can be measured on the SPRM. To the best of our knowledge, the is no direct measurement to separate two loss mechanisms of SP.

In Chapter 6, we successfully applied the ptychographic iterative engine to recover the complex field on the BFP. It allows us to extract more information for further use. With our modified algorithm, the scaling factor of the system is accurately determined. Also, we also showed that the dynamic range of the detected can be solved by measuring the field on the defocused plane. By examining different samples, we showed the BFP Ptychography is a powerful tool to examine the angular response of a sample.

In this chapter, we will discuss some possible improvement can be conducted in the future.

7.1 Optimization on BFP Ptychography

In this thesis, we use the modified ptychographic iterative engine to recover the complex field on the BFP. The modified probe, Ronchi grating, can be used as a calibration tool of the scaling factor between object plane and its diffraction plane. However, there are still lots of room to improve the overall performance such the duty cycle of the Ronchi grating, multiple levels probe. With optimal parameters, the convergence rate and time of data acquisition can be improved.

7.1.1 Grating with different duty cycle

In this study, 50% duty cycle Ronchi grating serves as the probe and the calibration tool for the algorithm. By rotating the Ronchi gating, we can control different regions of the exit field. The duty cycle will control the overlap region on each iteration region. Therefore, it can help to optimize the convergence. As the customized binary grating is expensive, we can first analyze the effect on simulation. Once the parameters are obtained, we can fabricate it to validate the estimation

7.1.2 Phase Grating by phase SLM

Compared to the conventional ptychography, it uses amplitude constraint to retrieve the phase distribution on the recovered object field. Integrated SLM into BFP ptychography may be a good idea, no moving part is involved. In the future, we would like to apply phase constraints. With phase grating, we can design more advanced pattern to improve the performance. Even further, multiple-level phase can be implemented. However, the problem of using phase SLM are (i) the stability of the phase modulation imposed by SLM and (ii) the fill gap between the pixel of phase-SLM. If these two problems can be solved, the hardware can be greatly simplified, and more advanced pattern can be introduced to improve the performance

7.2 Phase retrieval on thin Au Sample

The typical choice of the thickness of the Au layer is around 50 nm which is the optimum thickness for intensity-based measurement. However, this thickness may not be optimum thickness for the phase measurement of the SP signal.

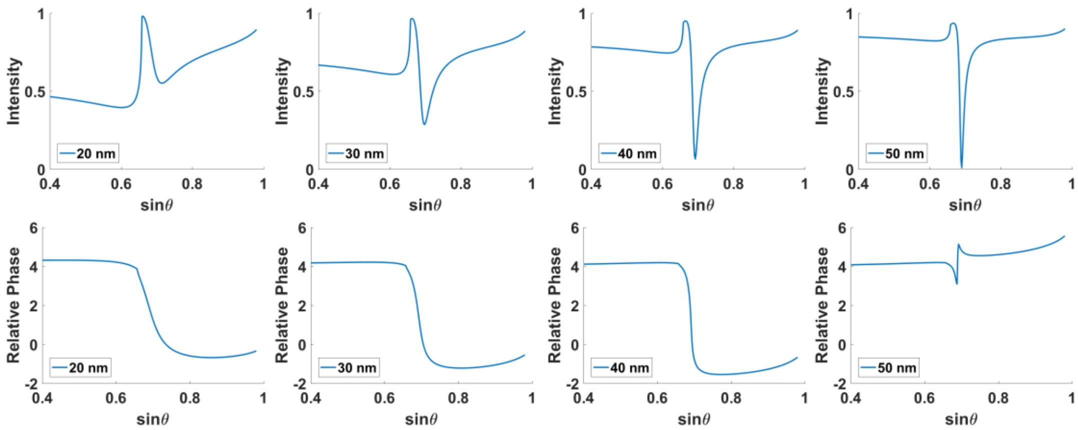

Figure 7-1 shows the phase and intensity of reflection on gold sample with the thickness of 20 nm, 30 nm, 40 nm and 50 nm respectively

It can be seen on the simulated response of p-polarization light as shown on Figure 7-1. It is expected the dip is sharp when thick gold is used. However, less information can be returned at resonance angle. Although, the dip of thin gold is less sharp. However, it may be a good choice for retrieval of the phase information. In the future, we would like to the gold sample with 30 nm thickness as our sensor to check the robustness of this method. For thin gold, on one hand, due to the high coupling coefficient, more light is coupled in the sensing layer resulting in better sensitivity. On the other hand, the total attenuation coefficient of thin gold is higher than that of thick layer. Therefore, the SP will attenuate more quickly to give better lateral resolution.

7.3 Multi-point BFP Ptychography

In Chapter 6, the recovery of the angular response (BFP) is only a single point on the image plane. It will make it even more attractive if we can extract the BFP from more than two illumination points.

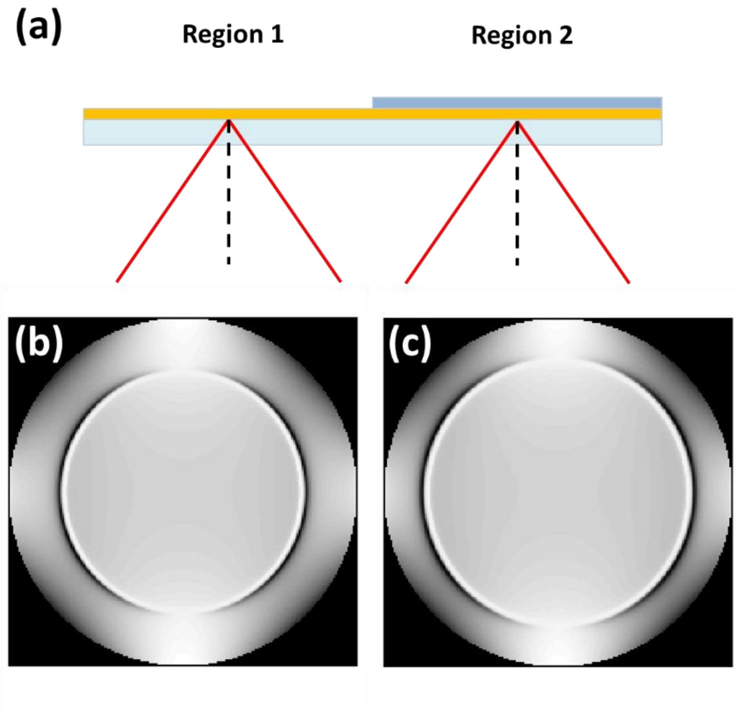

Figure 7-2 (a) shows the schematic diagram of two points illumination on region1 and region2. (b) and (c) are the BFPs in region 1 and 2 respectively

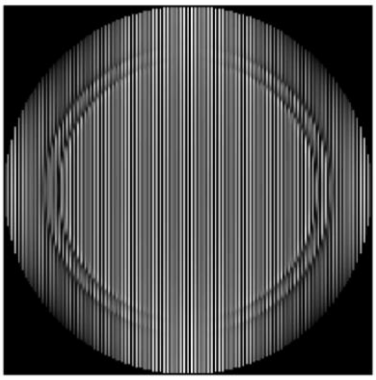

Figure 7-3 shows the intensity on the BFP for two-points illumination

Now, considering two points are illuminated in different region as shown on Figure 7-2, not surprisingly, the resultant field on the BFP shown on Figure 7-3 is the interference signal contributed from the fields on the BFP of these two illumination points. If the resultant complex field are recovered, we are able to perform many processing techniques to extract target information. For example, supposing we would like to calculate the k-vector or attenuation of the SP in region 1, it can be seen that it is quite challenging to measure the dip position from the BFP. However, by projecting the complex BFP onto the image plane, two points (see Figure 7-4) can be selected individually by self-defined filter.

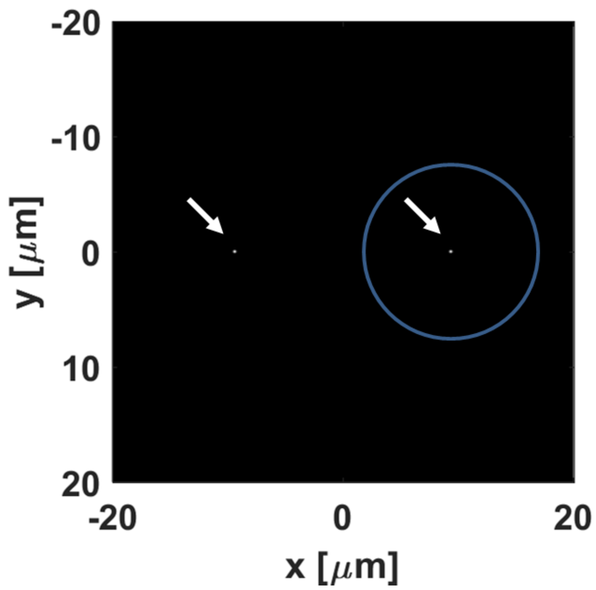

Figure 7-4 shows the projected points by recovered complex BFP. The white arrows indicate the illumination points

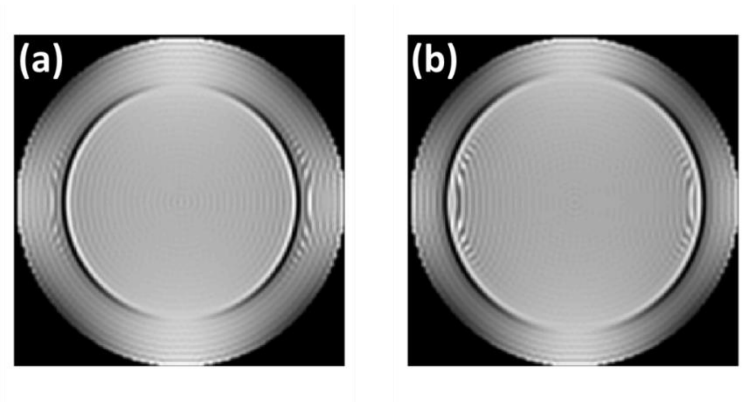

Figure 7-5 shows the modulus of the recovered BFP

As shown on Figure 7-4, by blocking the contribution outside the blue circles, we can select individual points to inverse Fourier transform to obtain the corresponding angular distribution (BFP) as shown on Figure 7-5. Indeed, the quality of the recovered BFP is not perfect due to the simple band-pass filter. However, it demonstrates the possibility of dealing with multi-point signal on image plane. When this technique is well developed, it is expected to extend to the case with multi-point illumination.

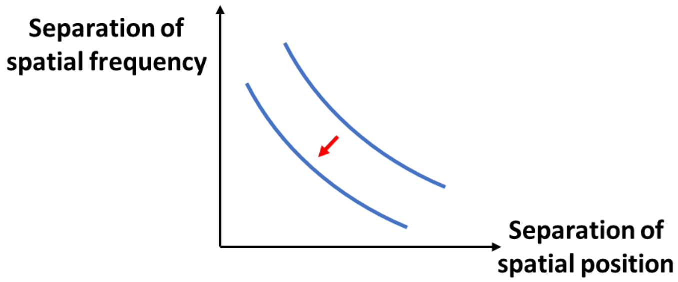

Figure 7-6 the conceptual diagram of the trade-off between separation of the spatial frequency and the separation of the spatial position.

In general, when the distance of the illuminated points becomes shorter, it is more difficult to recover good quality BFP result. In order words, there is a trade-off between the spatial frequency and the spatial position as shown on Figure 7-6. In the future, we would like to measure the trade-off between the separation of the spatial frequency and the separation of the spatial position quantitatively with the proposed method. Then, with the advanced processing method such as deep learning method, we would like to obtain better recovered BFP separately. The ultimate goal is to push the resolution boundary between the spatial frequency and the spatial position.

7.4 Phase Retrieval by Transport of Intensity Equation

One issue with ptychographic reconstruction is that in the image acquisition stage it is necessary to acquire a relatively large number of images in order to effect the reconstruction. This is clearly a disadvantage if we need to obtain information rapidly. We will suggest that it is worth investigating other phase retrieval methods such as transport of intensity equation (TIE) where it is necessary to acquire only, typically, three images.

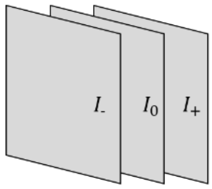

Figure 7-7 shows positions of three planes

In the TIE algorithm, the typical form can be expressed as

$$\frac{\partial I}{\partial z} = -\frac{\lambda}{2\pi} \nabla_\perp \cdot (I \nabla_\perp \phi) \tag{7-1}$$

where $I = I(x, y)$ and $\phi = \phi(x, y)$ are the intensity and the phase on the xy-plane respectively.

According to the equation (7-1), once we have the intensity of the three planes as shown on Figure 7-7, we can work out the $\frac{\partial I}{\partial z}$. By solving the equation, the phase ϕ can be calculated.

In our implementation, these could be obtained in parallel by projecting the image to three different planes. There would be experimental challenges with image registration but provided these issues are successfully overcome this approach would pave the way for extremely fast phase retrieval algorithms.

7.5 Conclusion

In this study, I applied a wide range of computational methods to achieve recover the phase information of the SP such as Hilbert transform and phase retrieval algorithm (Ptychographic iterative engine). With these computation methods, they can help to reduce the complexity of the system by reducing some of the components. With a compact form of the system, it is expected that the system can be more convenient, flexible, robust and easier to integrate with other systems. In the future, many computational methods can be applied on the SPRM to further improve the functionality of the instrument. On the other hand, the present thesis has examined a range of different techniques with standard samples which act as a proxy for the true biological materials. The advantage of using these samples is that they provide direct repeatable measurements to allow the different methods to be compared. In the future, we will examine real biological samples.

References

Argoul, F., Berguiga, L., & Fahys, A. (2010). W. I. P. Organization.

Beckers, M., Senkbeil, T., Gorniak, T., Giewekemeyer, K., Salditt, T., & Rosenhahn, A. (2013). Drift correction in ptychographic diffractive imaging. *Ultramicroscopy, 126*, 44-47. doi:https://doi.org/10.1016/j.ultramic.2012.11.006

Berini, P., & De Leon, I. (2011). Surface plasmon–polariton amplifiers and lasers. *Nature Photonics, 6*, 16. doi:10.1038/nphoton.2011.285

Bohm, D., & Pines, D. (1951). A Collective Description of Electron Interactions. I. Magnetic Interactions. *Physical Review, 82*(5), 625-634.

Bohm, D., & Pines, D. (1953). A Collective Description of Electron Interactions: III. Coulomb Interactions in a Degenerate Electron Gas. *Physical Review, 92*(3), 609-625.

Boltovets, P. M., Snopok, B. A., Boyko, V. R., Shevchenko, T. P., Dyachenko, N. S., & Shirshov, Y. M. (2004). Detection of plant viruses using a surface plasmon resonance via complexing with specific antibodies. *Journal of Virological Methods, 121*(1), 101-106. doi:https://doi.org/10.1016/j.jviromet.2004.06.019

Borch, J., & Roepstorff, P. (2004). Screening for Enzyme Inhibitors by Surface Plasmon Resonance Combined with Mass Spectrometry. *Analytical Chemistry, 76*(18), 5243-5248. doi:10.1021/ac049335f

Bracewell, R. N. (1978). *The Fourier transform and its applications*: Second edition. New York : McGraw-Hill, [1978] ©1978.

Cardona, M. (1971). Fresnel Reflection and Surface Plasmons. *American Journal of Physics, 39*(10), 1277-1277. doi:10.1119/1.1976627

Chow, T. W. K., Zhang, B., & Somekh, M. G. (2018). Hilbert transform-based single-shot plasmon microscopy. *Optics Letters, 43*(18), 4453-4456. doi:10.1364/OL.43.004453

Curtis, J. E., & Grier, D. G. (2003). Structure of Optical Vortices. *Physical Review Letters, 90*(13), 133901. doi:10.1103/PhysRevLett.90.133901

Dawson, P., Puygranier, B. A. F., & Goudonnet, J. P. (2001). Surface plasmon polariton propagation length: A direct comparison using photon scanning tunneling microscopy and attenuated total reflection. *Physical Review B, 63*(20), 205410. doi:10.1103/PhysRevB.63.205410

Dillon, P. P., Daly, S. J., Killard, A. J., & O'Kennedy, R. (2003). Development and Use of Antibodies in Surface Plasmon Resonance-Based Immunosensors for Environmental Monitoring. *International Journal of Environmental Analytical Chemistry, 83*(7-8), 525-543. doi:10.1080/0306731031000114929

EdmundOptics (Producer). (2018). Pellicle Beamsplitters. Retrieved from https://www.edmundoptics.com/f/Pellicle-Beamsplitters/12443/

Fano, U. (1941). The Theory of Anomalous Diffraction Gratings and of Quasi-Stationary Waves on Metallic Surfaces (Sommerfeld's Waves). *Journal of the Optical Society of America, 31*(3), 213-222. doi:10.1364/JOSA.31.000213

Faulkner, H. M. L., & Rodenburg, J. M. (2004). Movable Aperture Lensless Transmission Microscopy: A Novel Phase Retrieval Algorithm. *Physical Review Letters, 93*(2), 023903.

Faulkner, H. M. L., & Rodenburg, J. M. (2005). Error tolerance of an iterative phase retrieval algorithm for moveable illumination microscopy. *Ultramicroscopy, 103*(2), 153-164. doi:https://doi.org/10.1016/j.ultramic.2004.11.006

Fienup, J. R. (1982). Phase retrieval algorithms: a comparison. *Applied Optics, 21*(15), 2758-2769. doi:10.1364/AO.21.002758

Flynn, R. A., Bussmann, K., Simpkins, B. S., Vurgaftman, I., Kim, C. S., & Long, J. P. (2010). Propagation length of surface plasmon polaritons determined by emission from introduced surface discontinuities. *Journal of Applied Physics, 107*(1), 013109. doi:10.1063/1.3273480

Gerchberg, R. W., & Saxton, W. O. (1972). A practical algorithm for the determination of phase from image and diffraction plane pictures. *Optik, 35*, 237-250.

Giebel, K. F., Bechinger, C., Herminghaus, S., Riedel, M., Leiderer, P., Weiland, U., & Bastmeyer, M. (1999). Imaging of Cell/Substrate Contacts of Living Cells with Surface Plasmon Resonance Microscopy. *Biophysical Journal, 76*(1), 509-516. doi:https://doi.org/10.1016/S0006-3495(99)77219-X

Hamamatsu. (2015). How does the Hamamatsu LCOS-SLM operate? *Hamamatsu*. Retrieved from http://www.hamamatsu.com/jp/en/community/lcos/technology/index.html

Hessel, A., & Oliner, A. A. (1965). A New Theory of Wood's Anomalies on Optical Gratings. *Applied Optics, 4*(10), 1275-1297. doi:10.1364/AO.4.001275

Homola, J. (2006). Surface plasmon resonance based sensors. doi:https://doi.org/10.1007/b100321

Hoppe, W. (1969). Beugung im inhomogenen Primarstrahlwellenfeld. I. Prinzip einer Phasenmessung von Elektronenbeungungsinterferenzen. *Acta Crystallographica Section A, 25*(4), 495-501. doi:doi:10.1107/S0567739469001045

Huang, X., Yan, H., Harder, R., Hwu, Y., Robinson, I. K., & Chu, Y. S. (2014). Optimization of overlap uniformness for ptychography. *Optics Express, 22*(10), 12634-12644. doi:10.1364/OE.22.012634

Hurst, A. C., Edo, T. B., Walther, T., Sweeney, F., & Rodenburg, J. M. (2010). Probe position recovery for ptychographical imaging. *Journal of Physics: Conference Series, 241*(1), 012004.

Jordan, C. E., Frutos, A. G., Thiel, A. J., & Corn, R. M. (1997). Surface Plasmon Resonance Imaging Measurements of DNA Hybridization Adsorption and Streptavidin/DNA Multilayer Formation at Chemically Modified Gold Surfaces. *Analytical Chemistry, 69*(24), 4939-4947. doi:10.1021/ac9709763

Kabashin, A. V., Patskovsky, S., & Grigorenko, A. N. (2009). Phase and amplitude sensitivities in surface plasmon resonance bio and chemical sensing. *Optics Express, 17*(23), 21191-21204. doi:10.1364/OE.17.021191

Kabashin, A. V., Patskovsky, S., & Grigorenko, A. N. (2009). Phase and amplitude sensitivities in surface plasmon resonance bio and chemical sensing. *OPTICS EXPRESS*, 21191-21204.

Kano, H., & Knoll, W. (2000). A scanning microscope employing localized surface-plasmon-polaritons as a sensing probe. *Amsterdam*, 11-15.

Kano, H., Mizuguchi, S., & Kawata, S. (1998). Excitation of surface-plasmon polaritons by a focused laser beam. *Journal of the Optical Society of America B, 15*(4), 1381-1386. doi:10.1364/JOSAB.15.001381

Kolomenski, A., Kolomenskii, A., Noel, J., Peng, S., & Schuessler, H. (2009). Propagation length of surface plasmons in a metal film with roughness. *Applied Optics, 48*(30), 5683-5691. doi:10.1364/AO.48.005683

Kretschmann, E., & Raether, H. (1968). Radiative decay of nonradiative surface plasmons excited by light. *Z. Naturforsch. A, 23*, 2135. doi:citeulike-article-id:3901347

Löfås, S., Malmqvist, M., Rönnberg, I., Stenberg, E., Liedberg, B., & Lundström, I. (1991). Bioanalysis with surface plasmon resonance. *Sensors and Actuators B: Chemical, 5*(1), 79-84. doi:http://dx.doi.org/10.1016/0925-4005(91)80224-8

Lai, G., & Yatagai, T. (1991). Generalized phase-shifting interferometry. *Journal of the Optical Society of America A, 8*(5), 822-827. doi:10.1364/JOSAA.8.000822

Liedberg, B., Lundström, I., & Stenberg, E. (1993). Principles of biosensing with an extended coupling matrix and surface plasmon resonance. *Sensors and Actuators B: Chemical, 11*(1), 63-72. doi:https://doi.org/10.1016/0925-4005(93)85239-7

Liedberg, B., Nylander, C., & Lunström, I. (1983). Surface plasmon resonance for gas detection and biosensing. *Sensors and Actuators, 4*, 299-304. doi:https://doi.org/10.1016/0250-6874(83)85036-7

Limaj, O., Etezadi, D., Wittenberg, N. J., Rodrigo, D., Yoo, D., Oh, S.-H., & Altug, H. (2016). Infrared Plasmonic Biosensor for Real-Time and Label-Free Monitoring of Lipid Membranes. *Nano Letters, 16*(2), 1502-1508. doi:10.1021/acs.nanolett.5b05316

Love, G. D. (1997). Wave-front correction and production of Zernike modes with a liquid-crystal spatial light modulator. *Applied Optics, 36*(7), 1517-1524. doi:10.1364/AO.36.001517

Maiden, A. M., Humphry, M. J., Sarahan, M. C., Kraus, B., & Rodenburg, J. M. (2012). An annealing algorithm to correct positioning errors in ptychography. *Ultramicroscopy, 120*, 64-72. doi:https://doi.org/10.1016/j.ultramic.2012.06.001

Maiden, A. M., & Rodenburg, J. M. (2009). An improved ptychographical phase retrieval algorithm for diffractive imaging. *Ultramicroscopy, 109*(10), 1256-1262. doi:http://dx.doi.org/10.1016/j.ultramic.2009.05.012

Maiden, A. M., Rodenburg, J. M., & Humphry, M. J. (2010). Optical ptychography: a practical implementation with useful resolution. *Optics Letters, 35*(15), 2585-2587. doi:10.1364/OL.35.002585

Nguyen, H., Park, J., Kang, S., & Kim, M. (2015). Surface Plasmon Resonance: A Versatile Technique for Biosensor Applications. *Sensors, 15*(5), 10481.

Otto, A. (1968). Excitation of nonradiative surface plasma waves in silver by the method of frustrated total reflection. *Zeitschrift für Physik A Hadrons and nuclei, 216*(4), 398-410. doi:10.1007/BF01391532

Patching, S. G. (2014). Surface plasmon resonance spectroscopy for characterisation of membrane protein–ligand interactions and its potential for drug discovery. *Biochimica et Biophysica Acta (BBA) - Biomembranes, 1838*(1, Part A), 43-55. doi:https://doi.org/10.1016/j.bbamem.2013.04.028

Pechprasarn, S., Chow, T. W. K., & Somekh, M. G. (2018). Application of confocal surface wave microscope to self-calibrated attenuation coefficient measurement by Goos-Hänchen phase shift modulation. *Scientific Reports, 8*, 8547. doi:10.1038/s41598-018-26424-2

Pechprasarn, S., & Somekh, M. G. (2012). Surface plasmon microscopy: resolution, sensitivity and crosstalk. *Journal of Microscopy*, 287-297.

Römer, H. (2005). *Theoretical Optics: An Introduction*: John Wiley & Sons,Inc. NY.

Raether, H. (1986). *Surface Plasmons on Smooth and Rough Surfaces and on Gratings* (Vol. 111): Springer Tracts in Modern Physics.

Rayleigh. (1907). On the dynamical theory of gratings. *Proceedings of the Royal Society of London. Series A, 79*(532), 399-416. doi:10.1098/rspa.1907.0051

Ritchie, R. H. (1957). Plasma Losses by Fast Electrons in Thin Films. *Physical Review, 106*(5), 874-881.

Rothenhausler, B., & Knoll, W. (1988). Surface plasmon microscopy. *Nature, 332*(6165), 615-617.

Schasfoort, R. B. M., & Tudos, A. J. (2008). *Handbook of Surface Plasmon Resonance*: The Royal Society of Chemistry.

Shenfield, A., & Rodenburg, J. M. (2011). Evolutionary determination of experimental parameters for ptychographical imaging. *Journal of Applied Physics, 109*(12), 124510. doi:10.1063/1.3600235

Singhal, A., Haynes, C. A., & Hansen, C. L. (2010). Microfluidic Measurement of Antibody−Antigen Binding Kinetics from Low-Abundance Samples and Single Cells. *Analytical Chemistry, 82*(20), 8671-8679. doi:10.1021/ac101956e

Situ, C., Mooney, M. H., Elliott, C. T., & Buijs, J. (2010). Advances in surface plasmon resonance biosensor technology towards high-throughput, food-safety analysis.

TrAC Trends in Analytical Chemistry, 29(11), 1305-1315. doi:https://doi.org/10.1016/j.trac.2010.09.003

Somekh, M. G., Liu, S., Velinov, T. S., & See, C. W. (2000). High-resolution scanning surface-plasmon microscopy. *Applied Optics, 39*(34), 6279-6287. doi:10.1364/AO.39.006279

Somekh, M. G., Liu, S. G., Velinov, T. S., & See, C. W. (2000). Optical V(z) for high-resolution 2π surface plasmon microscopy. *Optics Letters, 25*(11), 823-825. doi:10.1364/OL.25.000823

Stabler, G., Somekh, M. G., & See, C. W. (2004). High-resolution wide-field surface plasmon microscopy. *Journal of Microscopy, 214*(3), 328-333. doi:doi:10.1111/j.0022-2720.2004.01309.x

Sui, G., Cheng, L., & Chen, L. (2011). Large positive and negative lateral optical beam shift due to long-range surface plasmon resonance. *Optics Communications, 284*(6), 1553-1556. doi:https://doi.org/10.1016/j.optcom.2010.10.091

Sun, J., Chen, Q., Zhang, Y., & Zuo, C. (2016). Efficient positional misalignment correction method for Fourier ptychographic microscopy. *Biomedical Optics Express, 7*(4), 1336-1350. doi:10.1364/BOE.7.001336

Suárez, I., Ferrando, A., Marques-Hueso, J., Díez, A., Abargues, R., Rodríguez-Cantó Pedro, J., & Martínez-Pastor Juan, P. (2017). Propagation length enhancement of surface plasmon polaritons in gold nano-/micro-waveguides by the interference with photonic modes in the surrounding active dielectrics. In *Nanophotonics* (Vol. 6, pp. 1109).

Thibault, P., Dierolf, M., Bunk, O., Menzel, A., & Pfeiffer, F. (2009). Probe retrieval in ptychographic coherent diffractive imaging. *Ultramicroscopy, 109*(4), 338-343. doi:https://doi.org/10.1016/j.ultramic.2008.12.011

Wood, R. W. (1902). On a Remarkable Case of Uneven Distribution of Light in a Diffraction Grating Spectrum. *Proceedings of the Physical Society of London, 18*(1), 269.

Yeatman, E., & Ash, E. A. (1987). Surface plasmon microscopy. *Electronics Letters, 23*(20), 1091-1092. doi:10.1049/el:19870762

Yeatman, E. M. (1996). Resolution and sensitivity in surface plasmon microscopy and sensing. *Biosensors and Bioelectronics, 11*(6–7), 635-649. doi:http://dx.doi.org/10.1016/0956-5663(96)83298-2

Zhang, B., Pechprasarn, S., & Somekh, M. G. (2012). Surface plasmon microscopic sensing with beam profile modulation. *Optics Express, 20*(27), 28039-28048. doi:10.1364/OE.20.028039

Zhang, B., Pechprasarn, S., & Somekh, M. G. (2013). Quantitative plasmonic measurements using embedded phase stepping confocal interferometry. *Optic Express*, 11523-11535.

Zhang, B., Pechprasarn, S., & Somekh, M. G. (2013). Quantitative plasmonic measurements using embedded phase stepping confocal interferometry. *Optics Express, 21*(9), 11523-11535. doi:10.1364/OE.21.011523

Zhang, B., Pechprasarn, S., Somekh, M. G., & Zhang, J. (2012). Confocal surface plasmon microscopy with pupil function engineering. *OPTICS EXPRESS*, 7388-7397.

Zhang, B., Pechprasarn, S., Zhang, J., & Somekh, M. G. (2012). Confocal surface plasmon microscopy with pupil function engineering. *Optics Express, 20*(7), 7388-7397. doi:10.1364/OE.20.007388

Zhang, F., Peterson, I., Vila-Comamala, J., Diaz, A., Berenguer, F., Bean, R., . . . Rodenburg, J. M. (2013). Translation position determination in ptychographic coherent diffraction imaging. *Optics Express, 21*(11), 13592-13606. doi:10.1364/OE.21.013592

Appendix

I. Model of SP Propagation length and Attenuation

In this section, I will briefly describe the relationship between Goos–Hänchen phase shift and the V(z) curve measurement. It requires the knowledge of stationary phase to understand the confocal measurement of V(z).

Stationary Phase

The decaying field on the sample surface will be formed when it is illuminated by a large angular range. In this thesis, the analysis uses the reflection coefficient from the Fresnel equations and a pupil function corresponding to spherical lens with input linear polarization.

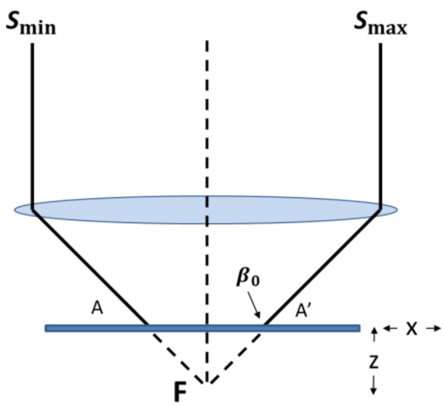

Figure A 1 shows the path length between the focus and the point of intersection with the sample

By considering the analytical expression in 1D case, the principle of stationary phase is applied. (Sui, Cheng, & Chen, 2011) The asymptotic representation of the field on the sample surface and the field distribution due to the SP on the surface will be calculated.

The field on the sample surface can be expressed in a weighted sum of all the plane wave components as function of defocus which is

$$E(x,z) = \int_{s_{min}}^{s_{max}} P(s) \exp[ik(z\cos\theta + xs)]\, ds$$

$$= \int_{s_{min}}^{s_{max}} P(s) \exp\left[ikz\left(\sqrt{1-s^2} + \beta s\right)\right] ds$$

Where s is the sine of the incident angle θ of plane wave, P is the pupil function, k is wavenumber and $\beta = x/z$.

The phase term, $\emptyset(\beta,z) = kz\left(\sqrt{1-s^2} + \beta s\right)$, in the derivative is zero when $\beta = \frac{s}{\sqrt{1-s^2}}$. At this point, the second derivative is given by

$$\emptyset''(\beta,z) = \frac{d^2\emptyset(\beta,z)}{ds^2} = -\frac{kz}{(1-s^2)^{\frac{3}{2}}} = -\,kz(1+\beta^2)^{3/2} \quad \text{(A-1)}$$

The asymptotic stationary phase solution is this given by

$$E(\beta,z) \approx P(\beta,z)\sqrt{\frac{2\pi}{kz}}(1+\beta^2)^{\frac{3}{4}} \exp\left[i\frac{\pi}{4}\mathrm{sgn}(\emptyset'')\right] \exp[i\emptyset(\beta,z)]$$

$$= A(\beta,z)\exp[i\emptyset(\beta,z)]$$

Where $\emptyset(\beta,z) = kz\left(\sqrt{1-s^2} + \beta s\right) = kz(1-s^2)^{-\frac{1}{2}} = \frac{kz}{\cos\theta} = kz\left(\sqrt{1+\beta^2}\right)$.

In the above expression, it states that the relative optical path difference on the sample surface is a function of the incident angle of plane wave as shown on Figure A 1.

The next step is to estimate the field distribution arising from the surface wave excitation. Each point on the surface will generate a surface wave. The resultant field distribution is determined by the weighted sum of these surface wave contributions.

As $\frac{d\beta}{dx} = \frac{1}{z}$, the field due to the SPs travelling from left to right is given by

$$2k_c'' \int_{-\infty}^{x_0} E(x,z) \exp ik_p(x_0 - x)dx = 2k_c'' \int_{-\infty}^{\beta_0} \frac{1}{z} E(\beta,z) \exp ik_p z(\beta_0 - \beta)\,(zd\beta)$$

By using the stationary solution derived above, the excited field can be written as

$2k_c'' \int_{-\infty}^{\beta_0} A(\beta,z) \exp[i\emptyset(\beta)] \exp ik_p z(\beta_0 - \beta)\, d\beta$

= $2k_c'' \exp(ik_p'\beta_0 z) \int_{-\infty}^{\beta_0} A(\beta,z) \exp[-k_p'' z(\beta_0 - \beta)] \exp[ikz(\sqrt{1+\beta^2} -$

$\beta \sin\theta_p)]d\beta$

provided that $k_p = k_p' + ik_p''$ and $k_p' = k \sin\theta_p$.

Similarly, the stationary phase point for this integral is when $\frac{\beta}{\sqrt{1+\beta^2}} = \sin\theta_p$ and therefore $\beta = \tan\theta_p$. The second differential of the phase variation at the stationary phase point is $\frac{kz}{(1+\beta^2)^{3/2}}$

The field due to the SP travelling from left to right at negative defocus z can be expressed in term of 3 components which is

$$A1 \text{ Exp1 Exp2} \qquad \text{(A-2)}$$

Where

$$A1 = 2k_c'' \sqrt{\frac{2\pi z}{k}} A(-\tan\theta_p\,, z)\left(1 + \tan^2\theta_p\right)^{\frac{3}{4}}$$

$$\text{Exp1} = \exp\left(ik_p \sin\theta_p\, x_0 + \frac{\pi}{4}\right) \exp(-ikz\cos\theta_p)$$

$\text{Exp2} = \exp[-k_p''(x_0 + z\tan\theta_p)]$

From the expression above, A1 is the predicted amplitude, Exp1 is the propagation exponential and Exp2 is the decaying exponential. It should be noted that the attenuation constant is the imaginary part of the SP. (Flynn et al., 2010; Kolomenski et al., 2009; Suárez et al., 2017). Therefore, by measuring the imaginary part of the SP, the total attenuation of the SP can be obtained.

II. Specifications

<table>
<tr><th>Key Components</th><th>Specifications</th></tr>
<tr><td>Spatial Light Modulator</td><td>Holoeye, LETO
<table>
<tr><td>Display Type:</td><td>Reflective LCOS (Phase Only)</td></tr>
<tr><td>Resolution:</td><td>1920 x 1080</td></tr>
<tr><td>Pixel Pitch:</td><td>6.4 µm</td></tr>
<tr><td>Fill Factor:</td><td>93 %</td></tr>
<tr><td>Addressing</td><td>8 Bit (256 Grey Levels)</td></tr>
<tr><td>Signal Formats</td><td>HDMI – HDTV Resolution</td></tr>
<tr><td>Input Frame Rate</td><td>60 Hz / 180 Hz</td></tr>
</table></td></tr>
<tr><td>Camera
(used for BFP in confocal detection in SLM-based SPM and BFP in ptychography)</td><td>Thorlabs, DCC3240M
<table>
<tr><td>Sensor Type:</td><td>Monochrome</td></tr>
<tr><td>Resolution:</td><td>1280 x 1024</td></tr>
<tr><td>Pixel Pitch:</td><td>5.3 µm</td></tr>
<tr><td>Addressing</td><td>8 Bit (256 Grey Levels)</td></tr>
<tr><td>Interface</td><td>USB 3.0</td></tr>
</table></td></tr>
</table>

<table>
<tr><td>High NA objective</td><td>Nikon, CFI Apo TIRF 60x H
<table><tr><td>Numerical Aperture:</td><td>1.49</td></tr><tr><td>Magnification:</td><td>60x</td></tr></table>
Tube length</td></tr>
</table>

<table>
<tr><td>Key Components</td><td>Specifications</td></tr>
<tr><td>Ronchi Ruling</td><td>Edmund Optics
<table><tr><td>Coating:</td><td>Vacuum Deposited Chrome</td></tr><tr><td>Frequency (lp/mm):</td><td>5</td></tr><tr><td>Optical Density OD:</td><td>3.00</td></tr><tr><td>Substrate:</td><td>Float Glass</td></tr><tr><td>Dimensions (inches)</td><td>1 x 1</td></tr><tr><td>Thickness (mm)</td><td>1.50</td></tr><tr><td>Line to Line Parallelism (arcsec)</td><td>≤2</td></tr></table></td></tr>
</table>

	Surface Flatness: 1λ
Camera (used for image plane in ptychography)	Andor, Zyla 5.5 Sensor Type: CMOS Resolution: 2560 x 2160 Pixel Pitch: 6.5 µm Data Range: 12-bit and 16-bit Maximum Dynamic Range: 33,000:1 Interface: USB 3.0